MACROSCOPIC QUANTUM TUNNELING AND QUANTUM MANY-BODY DYNAMICS IN BOSE-EINSTEIN CONDENSATES

by

Diego A. Alcala

A thesis submitted to the Faculty and the Board of Trustees of the Colorado School of Mines in partial fulfillment of the requirements for the degree of Doctor of Philosophy (Physics).

Golden, Colorado

Date _____

Signed: _____
Diego A. Alcala

Signed: _____
Dr. Lincoln D. Carr
Thesis Advisor

Signed: _____
Dr. Mingzhong Wu
Thesis Advisor

Golden, Colorado

Date _____

Signed: _____
Dr. Uwe Greife
Professor and Head
Department of Physics

ABSTRACT

Quantum mechanics revolutionized the previous century, not only in technology with lasers and semiconductors but also our fundamental view of the world with Bell's inequality and entanglement. Quantum tunneling was the first experimental verification of quantum mechanics, by solving the mystery of radioactive decay, that a particle can escape the nucleus without sufficient energy to overcome the classical energy barrier. In this century, many-body quantum mechanics is bringing about a second revolution, with the possibility of quantum simulators, quantum computers, and a deeper understanding the nature. However, in order to fully harness the power of these systems, a detailed understanding of many-body effects is required, such as fluctuations, correlations, and entanglement. In this thesis, we seek to understand these observables in the context of macroscopic quantum tunneling. We quantify the macroscopic quantum tunneling dynamics, showing how interactions alter tunneling and quantum phase transitions modify non-equilibrium dynamics, providing a road maps of future experiments.

The first experimental realization of mean-field interactions producing non-exponential decay of a tunneling Bose-Einstein condensate has been achieved. We develop an effective semi-classical model which accounts for the repulsive atom-atom interactions via an additional mean-field potential. This captures the 3D quantum tunneling via classical oscillations in an effective 1D trap and tunneling through a barrier with time-dependent height due to mean-field interactions. Mean-field treatments work well for Bose-Einstein condensates with negligible many-body effects, such as fragmentation, depletion, and fluctuations away from the mean. We show how a Bose-Einstein condensate with non-negligible fragmentation and depletion can be described with a renormalized mean-field. This suggest mean-field models are more widely applicable than previously thought, and that many-body physics may be hiding in such experiments and systems.

Next, we explicitly look at the dynamics of many-body tunneling from a meta-stable trap, described by the Bose-Hubbard Hamiltonian in the superfluid quantum phase. The many-body physics are simulated using matrix product state methods, which allow exploration of lowly-entangled dynamics via data compression methods, and can calculate a wide range of quantum observables, like number fluctuations, correlations, and entanglement entropy. We compare many-body and mean-field dynamics, explicitly showing many-body tunneling times converge to mean-field tunneling times with increasing number of atoms in the system. We find rich dynamics with different time scales for the escape time, fluctuations, and quantum entropy in the system.

With a firm grasp on the superfluid dynamics in the Bose-Hubbard Hamiltonian, we turn our attention to the superfluid to Mott insulating quantum phase transition, and understanding how the initial quantum phase alters macroscopic quantum tunneling. We examine this for both the double-well and quantum escape systems. We find that the dynamics of tunneling are strongly dependent on the quantum phase of the ground state. Qualitatively, the superfluid regime has wave-like dynamics, while the Mott regime has particle-like dynamics, and near the critical point there is a mixture of the two. The dynamics of many-body observables, fluctuations and correlations, have distinct signatures of their quantum phases, fingerprints pointing to the quantum phase transition.

Finally, we provide a road map for future macroscopic quantum tunneling experiments, in particular for two accessible trap configurations in both semi-classical and strongly interacting regimes. Using a semi-classical method, we study the gross features of macroscopic quantum tunneling in symmetric offset Gaussian barriers, and a linearly ramped Gaussian barrier. Because the tunneling probability depends exponentially on the barrier area, large, heavy, or many interacting atoms can have tunneling rates too slow to be experimentally viable. We show how to overcome this time-scale issue, quantifying the time and length scales regarding macroscopic quantum tunneling of Bose-Einstein condensates of rubidium, lithium, and sodium, deriving scaling laws for the various trap parameters; the experimental

"knobs". Scaling laws clearly demonstrate when oscillations in the well or tunneling probabilities dominate. We find the emergence of mean-field islands inside the traps, resulting in multiple oscillations.

In the strongly interacting regime, preliminary evidence is provided for pulsed and continuous-wave regimes of a correlation-based atom laser utilizing macroscopic quantum tunneling in both barrier and interaction control.

TABLE OF CONTENTS

LIST OF FIGURES

LIST OF ABBREVIATIONS

Atomic, Molecular, and Optical . . . . . AMO

Berzinskii-Kosterlitz-Thouless . . . . . BKT

Bose-Einstein Condensate . . . . . BEC

Bose-Hubbard Hamiltonian . . . . . BHH

Discrete Nonlinear Schrodinger Equation . . . . . DNLSE

Gross-Pitaevskii Equation . . . . . GPE

Jeffreys-Wentzel-Kramers-Brillouin . . . . . JWKB

Macroscopic Quantum Tunneling . . . . . MQT

Matrix Prodcut State . . . . . MPS

Nonlinear Schrodinger Equation . . . . . NLSE

Quantum Phase Transition . . . . . QPT

Time-Evolving Block Decimation . . . . . TEBD

ACKNOWLEDGMENTS

Thank you to my adviser Lincoln, for making this possible. For your constant and unwavering encouragement and support, enthusiasm for science, helping me reach limits I didn't know I could achieve, and for believing in me. My co-adviser Mingzhong for his patience and support and giving me the opportunity to work with the amazing members of his research lab. Thank you to my committee, Luis Tenorio, David Flammer, and Stephen Pankavich for encouraging, challenging, and supporting me and, for their flexibility and patience throughout the whole process.

Thank you to all my collaborators outside the School of Mines that made this work possible. Joseph Glick for getting me started on many-body quantum tunneling. Gregor Urban and Matthias Weidemüller from Heidelberg University for their support in finishing our joint work. Shreyas Potnis, Ramon Ramos, and Aephraim M. Steinberg, at the University of Toronto, for their great efforts in carrying out the experimental work and asking deep and probing questions on the manuscript.

To my parents for believing in me, sharing in the joy of success, and helping and supporting me through the pain of failure. Words cannot convey how incredibly blessed I am to have you in my life. With eternal gratitude and love, thank you.

Thank you to my family, for showing me what it's like to perceiver and prosper through difficult situations. In the most difficult times, when I couldn't push forward by my own strength, I was able to perceiver because of my family. For letting me indulge in physics talk, and being receptive and curious about the whole process, reminding me why I got into science.

Thank you to my lab mates, to everyone that I got to meet and interact with in the Carr research group at Mines and Mingzhong's research group at CSU. Now that it's passed, those few long years feel like the blink of an eye. A special thank you to Xinxin Zhao and

Marie McLain for supporting me and helping me through some of the most difficult times. I would not have made it through without you two, from the bottom of my heart thank you. Daniel Jaschke, for being someone I could look up to and learn from, learn how to work hard but still find humor in everything and laugh. Gavriil Shchedrin from Texas, for being a constant source of light heartedness, laughter, and inspiration. For watching over all the students, guiding them and giving them words of wisdom to have a meaningful and balanced life. Anastasia Gladkina, for our enjoyable conversations about life and the world and everything in-between. For reminding me of the joy, curiosity, and enjoyment of science that I forgot part way through grad school. To Majed Alotaibi, for the conversations we'd have about family and life and physics, where I came to realize how similar we all are, with similar struggles and similar faults, and for constantly being so energetic and always smiling and laughing. Justin Anderson, for being so down to earth and being an example of pushing through struggles and difficult times. Scott Strong, for very enjoyable conversations, which were simultaneously random and insightful. Nathanael Smith, for your words of support and encouragement. Even if they were just off hand comments, they helped a lot more than you know. Marc Valdez for being so levelheaded and chill and being an amazing person I could look up to. David Vargas for the fun times making up random nonsense in the physics lab and being the only one in the lab to get my nerdy references.

Thank you to all my friends at Mines. A special thank you to Andrew Proudian for being an inspiration, someone I look up to, and the fun times we shared talking and nerdying out. Shane Mahaffey and Matthew Marino for showing me what it means to work hard and play hard, and the many good side-splitting laughs we had together.

Thank you to all the staff and support at the Colorado School of Mines. A special thank you to Barbara and LeeAnn, for making the physics department feel like a home away from home, for always being there to take care of the students.

CHAPTER 1

FUNDAMENTAL CONCEPTS: A GENTLE INTRODUCTION

This chapter introduces the main topics of this thesis: macroscopic quantum tunneling, many-body quantum mechanics, Bose-Einstein condensates, and the methods that are incorporated to tackle these systems.

1.1 Many-body Quantum Tunneling

In our modern and often romanticized retelling of the invention of quantum mechanics, or any great leap in scientific knowledge, we are tempted to envision the great scientists of the day wrestling with the forces of nature or attempting to peer into the very mind of God. Quantum mechanics, with all of its philosophical intrigue and predictive power, was pioneered by physicists of the early 20th century for, arguably, the same reason that all great scientific understanding is manifest, *curiosity*, or to put more simply, to answer some seemingly innocuous questions: why is light emitted with specific colors or line widths, how can alpha particles escape from a nucleus with less energy than should be possible, could it be possible for a molecule to switch between left and right handedness, etc. These questions, and others, interesting in their own right, lead to the discovery of quantum mechanics and quantum tunneling. We will focus on the *tunnel effect* arising from *wave mechanics*, or now commonly known as quantum tunneling, one of the greatest triumphs of early quantum mechanics, and the first of many times that quantum mechanics would solidify itself as *the* theory of atomic phenomenon.

So, what is quantum tunneling? In the simplest sense, quantum tunneling is the ability of atomic objects (electrons, protons, atoms, etc.) to "pass through" a "solid" barrier. Allow me to give a crude and oversimplified analogy. Instead of a material "going through" a barrier, it's conceptionally easier to think about energetically going over a barrier. Imagine a kid riding a bicycle approaching a small hill. The kid pedals right to the bottom of the

hill, and then tries to ride up and over, using only that initial speed, with no additional pedaling. Without enough energy, the kid will get part way up, then roll back down. In classical mechanics, we say that the kid+bicycle did not have enough energy to overcome the barrier that was the hill. Now, try to imagine a quantum mechanical kid on a bicycle. What would that look like? Well, that's an interesting philosophical question, but for our purposes just imagine that as the kid goes faster and faster, a large and thick cloud start to surround the kid+bicycle, with a radius of a few meters. The "quantum mechanical" kid+bicycle cloud system approaches the hill at the same speed, at least the cloud seems to be moving with about the same energy, but you can't really see the kid or the bicycle, just the cloud. And, to your amazement, the cloud makes it past the hill. You run up to the kid, who stops moving, and the cloud disappears, and you're both left scratching your heads.

In the lab, this cloud+kid system is said to be the wave function of a system. Instead of knowing the position and momentum of a particle, like classical mechanics, in quantum mechanics we have a particle's statistical distribution, the "cloud". Why does this happen at the quantum level, but not for large "classical" objects? When examining objects at small enough length scales, atomic or lower, they stop behaving like classical particles, such as base balls. Instead, the objects start to exhibit both particle and wave-like properties; they can either be like a wiggling jump rope or a baseball depending on how you interact with them. Things that are sufficiently small, or large things that are sufficiently cold will behave quantum mechanically when their de Broglie wavelength is larger than their spatial extent.

Now a quick introduction to macroscopic quantum tunneling. Despite the conceptual difficulty, the physics of single atomic particles is very well understood with the Schrodinger equation, which is computationally accessible to physics students at the undergraduate level. However, when a large collection of atomic objects interacts, they open up amazing opportunities. One example is entangled between quantum objects. Two atoms are entangled when some measurable between them is perfectly correlated, even if they are separated by large distances. This property brings up many still-unanswered philosophical questions. It

allows for research on science fiction sounding phenomena like "quantum teleportation", and many believe entanglement is a key to quantum computers. Beyond the lab, nature has already tapped into this phenomenon, with strong evidence that entanglement is involved in photosynthesis. Many-body systems also start to '"push into" the classical world, forcing scientists to think about the boundary or limit between the intuitive world of classical mechanics and the unintuitive quantum world. A particularly powerful tool to explore this boundary is Bose-Einstein Condensates, a macroscopic object that behaves quantum mechanically, further discussed in Section 1.3.

1.2 Single to Many-body Quantum Mechanics: The necessity of simplifications

We've touched on "what" quantum tunneling is. Here we discuss how quantum problems are solved. Single-body non-relativistic quantum mechanics are well understood with the Schrodinger equation, a wave equation where the solution, the wave function, is a probability amplitude; in other words, the solution is a statistical distribution. There are a handful of textbook problems that are analytically solvable systems for the Schrodinger equation: infinite and finite square wells, harmonic potentials, and Dirac delta potentials. These all help build intuition of quantum mechanics: square wells give quantized energy levels, harmonic wells are good approximations to real-world potentials, Dirac delta potentials approximate scattering barriers. Beyond just textbook problems, single electron models with periodic potentials are used to describe solid state devices, and the hydrogen atom is also analytically solvable. Beyond the handful of textbook problems, analytics becomes intractable and approximations become necessary, Section 1.5. However, even approximations quickly become too difficult, requiring numerical solutions: such as complicated potentials, 3D, time-dependent potentials, etc.

Many-body systems provide even more difficulty to the intrepid researcher. The inherent difficulty in solving many-body quantum systems comes from having to deal with interactions between atoms. Classically, one solves for the position and momentum of each particle in a system, the dimension of the problem can be said to grow linearly with each additional

particle; each additional particle introduces two more variables that must be solved. In quantum mechanics, each additional atom multiplies the dimension of the system, rather than simply adding an additional position and momentum to solve for, and thus grows exponentially. Consider that, even classical many-body systems are not fully understood, which have been actively studied since the late 18th century, are an active area of research with many unanswered questions in nonlinearity, solitons, and chaotic systems.

1.3 Bose-Einstein Condensates

A Bose-Einstein condensate is an object made up of atoms which are all in the same quantum mechanical state. In other words, it can be considered as a single quantum object, despite being composed of tens, if not, thousands of atoms; a truly macroscopic quantum object. In the lab, they are created by cooling a gas of alkali atoms to Kelvin temperatures below 10^{-5}. This feat is accomplished with a collection of magnetic traps and lasers. The combination of lasers and magnetic traps are highly controllable and customizable: from pseudo 1D traps to full 3D traps. This high level of control allows single-site resolution, and tunable interatomic interactions, via Feshbach resonances, over 7 orders of magnitude. They allow for the exploration of mean-field dominated physics, all the way to many-body physics.

1.4 Quantum Phase Transitions

Ultracold atomic systems allow for the study of quantum phase transitions. Classical phase transitions occur when some thermal observable, temperature, pressure, etc., are modified through a critical value and result in a different state of matter. A simple example is the discontinuity in the first derivative of free energy when going from a liquid to a gas. Discontinuity in the second derivative occurs for ferromagnetic-antiferromagnetic and superfluid transitions, which lead to the study of universal critical scaling. A key idea in phase transitions is that different states of matter have different symmetries, and thus the critical point is moving between different symmetries. Quantum phase transitions also describe

these abrupt changes between phases, between different symmetries, but occur at zero temperature, when thermal fluctuations are zero, and thus are driven by quantum fluctuations. Despite being defined at zero temperature, when the energy of thermal fluctuations is sufficiently low, quantum phase transitions are observable. Finite systems at finite temperature can, for all practical purposes, still produce QPTs [1, 2].

This thesis focuses on the Bose-Hubbard Hamiltonian and its quantum phase transition from a superfluid to a Mott insulator. The superfluid state is a gapless state with global phase coherence. In other words, the phase uncertainty is minimal, and the many-body wavefunction describing the atomic cloud is described by a global phase breaking $U(1)$ symmetry. The Mott insulator is gapped, and in a commensurate filled lattice, the number uncertainty is minimal, while phase uncertainty is maximal. In other words, the system moves between a quantum phase with global phase coherence, and a quantum phase that breaks this symmetry. The Mott insulator gap, the required energy to the next excited state which would have two atoms on a given lattice site, is present regardless of the size of the system.

1.5 Analytic and numerical methods

Here, we briefly cover the analytical approximations and numerical schemes useful in our research. Sometimes, a many-body quantum system can be simplified by mean-field or semi-classical approximations. In a mean-field approximation, instead of examining all the individual atoms, the system is treated as a single field with the average of the system. In statistical physics, a thermometer measures the average kinetic energy of a system, and if fluctuations around this mean are small, then we don't need to know the position and momentum of every particle in the system but can just deal with the average. For a quantum example, this can also occur for superfluids, where each atom in a system is maximally delocalized with a global phase, and thus a mean-field gives a good approximation when there are enough atoms in the system, see Chapter 4. For a semi-classical approximation, some part of a quantum problem is treated as behaving approximately like a classical object.

In the JWKB approximation, Section 2.3.2, the momentum of the particles are approximated to be moving with a semi-classical momentum, this turns out to be a good approximation in a many situations, drastically simplifying calculations; this occurs in parts of a system where the de Broglie wavelength is not changing too rapidly. With any approximation scheme, we are necessarily losing some information. Sometimes all we want is order-of-magnitude estimates, or to understand gross or macroscopic properties of a system.

Even with appropriate approximations and simplifications, many problems require numerical solutions. Mean-field and semi-classical approximations can be readily solved with well-known numerical differential equation packages. Many-body problems, where approximations and simplifications are not suitable, also have numerical tools. When a many-body system is small enough, the Hilbert space is sufficiently small, and the system can be exactly diagonalized. In pseudo-1D systems, even when for many interacting atoms, area laws of entanglement allow for the efficient simulation with numerical compression algorithms, known as matrix product state methods, Section 2.4

1.6 Thesis organization

Chapter 1 attempts to present a non-technical introduction to the topics covered in this thesis, as a primer for anyone unfamiliar. These topics are expanded upon in technical detail in chapter 2, including literature reviews and derivations of all pertinent equations and methods. In chapter 3, we analyze the first experimental realization of quantum tunneling of a mean-field interacting Bose-Einstein condensate, using a modified JWKB model to include mean-field effects and reproduce the experimental non-exponential escape. We also examine how even successful mean-field treatments can have hidden many-body physics. The following three chapters explicitly look at many-body dynamics. In Chapter 4, we simulate superfluid dominated dynamics in the Bose-Hubbard Hamiltonian, tuning interactions from maximally possible attractive interactions, near self-trapping, to maximally possible repulsive interactions. Following that, in chapter 5 we allow interactions to go from the superfluid to Mott insulating quantum phases and study the influence of the phase transition on tunneling

dynamics. Chapter 6 includes additional unpublished results on the superfluid-Mott escape system, and also contributions to the analysis of the superfluid-Mott phase transition in a double-well, which includes the additional Josephson-Fock phase transitions. And finally, as a guide to future MQT experiments, in chapter 7 we use JWKB to quantify the MQT parameter space of two experimental potentials, clearly identifying where MQT could be realized, with conclusions and discussion in chapter 8.

CHAPTER 2

MANY-BODY QUANTUM MECHANICS: MATHEMATICAL MODELS AND COMPUTATIONAL TOOLS

In this chapter we will expand upon chapter 1, giving the necessary technical knowledge, background literature, and derivations of all models relevant to macroscopic quantum tunneling of Bose-Einstein condensates, with semi-classical, mean-field, and many-body treatments.

2.1 Many-Body Quantum Tunneling

In the simplest sense, quantum tunneling occurs when an object lacking enough energy to overcome an energy barrier can "tunnel", or pass through with some small but non-zero probability. This explanation was used by George Gamow and independently by Ronal Gurney and Edward Condon in 1928 to explain a surprising discovery by Ernest Rutherford: alpha particles seemingly escaped from uranium-238 with less than half of the required energy to escape of approximately 8.57 MeV. The solution, arising from the Schrodinger equation, naturally explained the probabilistic nature of alpha decay and reproduced the empirical findings by Geiger-Nuttall, exponential dependence of tunneling probability on energy. Specifically, Gamow derived an analytical approximation to the transmission rate given by e^{-2G}, with the Gamow factor, G, proportional to the nucleus and emitted particle nuclear charges and inversely proportional to the escape velocity [3]. While the Gamow factor is specific for alpha decay, we will show that this exponential form is very general to the JWKB approximation in Section 2.3.2.

While the excellent theoretical description of alpha decay provided by quantum tunneling is rightfully celebrated today, it propelled quantum mechanics into the forefront of theories for nuclear phenomena at the time, this was not actually the first use of the *tunnel effect*, but

provided the first agreement with experiment. Between 1926 and 1927, Friedrich Hund published three papers on the theory of molecular spectra, where, using a double-well system, he showed that the probability to tunnel through an energy barrier is exponentially dependent on the barrier area [4–6]. For tunneling between left and right-handed isomers, which Hund represented as a double-well problem, he showed that increasing the barrier area by a factor of 7 increased the frequency of tunneling from nanoseconds to a billion years [3].

Because of this exponential dependence, low-mass objects or smaller barriers produce much faster tunneling rates. Thus, tunneling is most frequently observed in electrons, light atoms, short distances (small barriers), and cold atoms; larger and more massive objects must be cold enough for their de Broglie wavelengths to exceed their physical size in order to behave quantum mechanically. In many semi-conductors electron screening allows for a single-particle electron treatment. This has allowed tunneling of electrons to be used in many devices like Zener diodes, flash memory, and tunneling microscopes. Quantum tunneling is also present in chemical and biological systems. Polycrystalline and amorphous ice at kelvin temperatures experience enhanced diffusion from quantum tunneling of atoms from hydrogen to oxygen [7, 8]. Complex molecules at kelvin temperatures have carbon atoms tunneling over sub-angstrom distances [9]. Tunneling also affects organic systems through the kinetic isotope effect and enzyme catalysis [10–12].

If the exponential dependence in tunneling is so extreme, are we limited to just the previous examples of single electronic and light-atomic systems? Is the concept of macroscopic quantum tunneling a moot point? Although one might suspect the issues with time-scales and exponential dependence to effectively kill MQT, in actuality, the landscape of MQT is more vast than one could imagine. Following is a brief discussion to the varied landscape of MQT, a more complete, but still non-exhaustive discussion can be found in [13]. The factors of MQT we cover are: macroscopicity, statistical properties, the different physics that result from interactions, the influence of the trapping potential, and the dimensionality of the system.

There is no universally accepted definition and characterization of "macroscopic", as it's an active are of research [14, 15]. For the purposes in this work, we will focus on macroscopic as it refers to either a large number of atoms or to large and heavy objects. Many atoms in a system results can result in fermionic or bosonic statistics [16, 17]. Additionally, many atoms can produce quasi-particles like anyons, vortices, solitons, skyrmions, excitons, or polaritons [18–20]. Bosons can create BEC's, a macroscopic object obeying quantum mechanics, see Section 2.2. BECs can also be comprised of different atomic species or be a mixture of different hyperfine states. Larger and heavier objects can still exhibit quantum properties at lower temperatures. The first realization of BECs was with Rubidium BEC atoms, and buckyballs, 60 carbon atoms in a soccer ball configuration, have been used in double-slit interference [21].

Macroscopic systems allow interactions to alter and produce new physics. Weakly coupled macroscopic quantum states produce the well-known Josephson dynamics [20, 22–24]. These can dynamically tunnel in AC or DC Josephson effects [25, 26] or be trapped for a critical tuning parameter [24]; we examine this for a double-well many-body system in Section 6.1. The interactions can be repulsive and attractive between atoms. This can result in atoms tunneling sequentially, one at a time, [27], and pairing phenomena [16, 27, 28] such as fermionization [28–30] can occur. The strength of interactions can be weak; weakly interacting bosons can often be accurately described via a mean-field [31–33]. Stronger interactions cause non-negligible fluctuations away from the mean with fragmentation, occupation of several macroscopic modes, and depletion, occupation of multiple non-macroscopic modes [34–36]. In 1D, bosons with sufficiently strong interactions can create a Tonks-Girardeau gas, which can exhibit both bosonic and fermionic properties [17, 37]

The geometry and flexibility in traps are a primary driver of the physics. The type of trap determines the kind of tunneling: quantum escape, double well, multiple well, periodic lattices, and dynamic "periodically shaken" lattices. In double wells, the states tunnel between discrete states in each well. In Josephson dynamics, weakly coupled macroscopic states

undergo quantum tunneling [20, 22–25, 25, 26, 26]. Beyond quantum escape and double wells, which are the central systems in this work, there are periodic potentials which modify transport [38, 39] and dressed potentials which enhance interactions between neutral atoms [40, 41]. Dynamic potentials, such as time-driven symmetry broken ring potentials create chaotic current reversal [42, 43], and shaken lattices can be used to modify the effective tunneling rates between sites [38, 44–46] Even a single boson atom can produce non-exponential decay on certain time scales because of the trap shape [47].

All chapters, expect for Chapter 3, exclusively use pseudo-1D potentials. This is because higher order tunneling can often be reduced to a quasi-1D system, where trajectories inside the well are averaged and tunneling is dominated by penetration through the energetically weakest points in a barrier [48]. This effective/averaged method does lose some information from the higher dimensional traps. For example, chaotic dynamics [49], which create oscillations and fluctuations [50–52].

2.2 Experimental Considerations: Ultracold Atoms, Bose-Einstein Condensates, and Quantum Phase Transitions

Advances in atomic, molecular, and optical physics have given scientists unprecedented access and control of quantum physics; control at the level of a single atom to hundreds of thousands of atoms in BECs. Single atoms, with their internal and external degrees of freedom, can be exploited in optical tweezers [53]. Many atoms can be trapped and controlled with a combination of optical and magnetic traps, allowing for simple and complex trap geometries. Such control has brought ultracold atomic systems as quantum simulators into the conversation of quantum computing [54]. These advances have allowed experimentalists to probe quantum phase transitions, with the realization of the Superfluid-Mott quantum phase transition [55].

The advances in AMO physics make it possible to create BECs. In a BEC there is the macroscopic occupation of a single quantum mechanical state. They were first realized in dilute gas clouds of rubidium [56], sodium [57], and lithium [58]. It was the combination of

laser cooling to trap alkali atoms and evaporative cooling which allowed scientist to reach sufficiently low temperatures, $O(10^{-}5)[K]$. BECs allow access to most of the MQT landscape described in Section 2.1. Beyond the study of quantum tunneling, condensation into a single quantum state gives access to quantum effects on a macroscopic scale. Experimentally, microscopy and optical lattices allow for single-site resolution, allowing up to 10th order correlations measurements via atomic interferometry [59]. BECs are highly condensed with low fragmentation and depletion, which grants analysis via the GPE in Section 2.3.3. But they are not limited the mean-field dominated interactions, also being able to access to many-body states [60]. Highly tunable interactions, via Feshbach resonances, can tune interactions over seven orders of magnitude [61]. The Flexible geometries required for MQT study are accessible via lasers traps and radio-frequency magnetic traps, which can also control the statistics and dimensionality of the system [62, 63].

A quantum phase transition (QPT) occurs when a small change in some parameter of a quantum system produces an abrupt change in the ground state properties. This abrupt change is often quantified by some non-analyticity in a correlator, or discontinuities in energy. In this thesis we focus on the BHH, full derivation in Section 2.3.4. The BHH demonstrates the Superfluid-Mott insulator QPT. The Superfluid is a gapless phase, in the infinite size limit, with global phase coherence. The Mott insulator has an energy gap $\Delta \sim U$, known as the Mott gap, where U is the on-site energy. This gap occurs because it takes a finite amount of energy to remove an atom from a site, leaving behind a hole, and place that atom into an already occupied site. The Superfluid-Mott QPT can occur in a second order $U(1)$ quantum phase transition and a continuous or Berzinskii-Kosterlitz-Thouless (BKT) quantum phase transition.

In the infinite limit, the critical point in the BHH occurs at $(U/J)_c \approx 3.28$ [64]. Although QPTs are usually taught in the infinite size limit and defined at zero temperature, they are observable in finite, or mesoscopic, systems and at finite temperatures, where thermal fluctuations are sufficiently small [2, 65]. In other words, the sharp behavior of QPTs is

observable in finite systems, with as few as 5 to 10 atoms [66]. These mesoscopic sizes also introduce the single-particle excitation gap, which scales like $1/L^2$, where L describes the system length. For an explicit and analytical example, the well-known infinite square well has energy states $E_n = n^2\pi^2\hbar^2/2mL^2$, with $n \in \mathbb{Z}$.

Beyond a description of ground state properties, QPTs can be studied and observed via the Kibble-Zurek mechanism [67]. To date, the principle example of a connection between quantum phases and dynamics is the Kibble-Zurek mechanism, which describes how the density of defects grow in a system as a function of how it is dynamically ramped through a critical point, giving information about the critical exponents of the critical point. This thesis presents a second example in Chapter 5, that non-equilibrium dynamics are determined primarily by the characteristics of quantum phases.

2.3 Models and Methods

This section derives the important models and methods used to study MQT throughout in the following chapters. We derive the Gross-Pitaevskii equation, discrete nonlinear Schrodinger equation, and the Bose-Hubbard Hamiltonian, explicitly stating how these equations relate. The semi-classical method in the Jeffreys-Wentzel-Kramers-Brillouin is presented in detail, being central to Chapters 3 and 7. We show how the various equations can be reduced from 3D to pseudo-1D systems. Together, these allow us to explore MQT from a single-particle to many-body and mean-field dominated physics.

2.3.1 Semi-Classical Physics

The semiclassical method, in the simplest sense, is a method which allows us to treat some aspect(s) of a quantum mechanical system as behaving classically. Intuitively, we can say that an object can be treated classically if the de Broglie wavelength of a system is smaller than some characteristic extent of the object under investigation; we will see this statement naturally occurs in mathematical form in the JWKB derivation, analogous to the Wave-to-Geometric optics transition.

The semiclassical method can be stated mathematically in two equivalent ways. First, when the de Broglie wavelength is much smaller than the object in question. That is to say, that the "wave nature" of an object becomes insignificant for a specific configuration of a system. Second, take the limit $\hbar \to 0$. This is directly analogous with the limit from wave to geometric optics and the Eikonal approximation. However, one might object that while $\hbar \to 0$ is mathematically convenient, isn't $\hbar$ a universal constant? The reader might find it useful to think about this as saying that everything in the system or equation is much larger than $\hbar$. In the following section, we demonstrate how the semi-classical approximation can be used for quantum tunneling, the well-known JWKB method.

2.3.2 The Jeffreys-Wentzel-Kramers-Brillouin (JWKB) approximation

The Hamiltonian for a single particle moving in a 1D potential is given by,

$$\hat{H} = \frac{\hat{p}^2}{2m} + V(x), \tag{2.1}$$

with mass m, a time independent potential $V(x)$, and the momentum operator $\hat{p}$. For a particle with wave function, $\psi(x)$, and using the canonical momentum operator, $\hat{p} = -i\hbar\frac{d}{dx}$,

$$\frac{d^2\psi(x)}{dx^2} + \frac{2m}{\hbar^2}[E - V(x)]\psi(x) = 0, \tag{2.2}$$

we get the well-known Schrodinger equation.

Take an ansatz of the form,

$$\psi(x) = \exp\left(\frac{i}{\hbar}S(x)\right). \tag{2.3}$$

Substituting in the ansatz into (2.2), along with substituting in the classical momentum,

$$p(x) = \sqrt{2m[E - V(x)]}, \tag{2.4}$$

gives

$$\frac{1}{\hbar^2}e^{iS(x)/\hbar}\left[(S'(x))^2 - i\hbar S''(x) - (p(x))^2\right] = 0. \tag{2.5}$$

We expand $S(x)$ in powers of $\hbar$; recall, if variables with units of action are small in comparison to $\hbar$, then we recover classical dynamics,

$$S(x) = \sum_j (-i\hbar)^j S_j(x) \tag{2.6}$$

with the first few terms written out

$$S(x) = S_0(x) + (\hbar/i)S_1(x) + (\hbar/i)^2 S_2(x) + \cdots . \tag{2.7}$$

We can now solve perturbatively. Starting with the 0th order approximation, we plug S_0 into (2.5), resulting in

$$p(x)^2 - S_0'(x)^2 + i\hbar S_0''(x) = 0. \tag{2.8}$$

If the terms satisfy the inequality,

$$\hbar|S_0''(x)| \ll |S_0'(x)^2| \tag{2.9}$$

in other words take all values of order $\hbar^0$, then

$$S_0(x) = \pm \int_{x_0}^{x} dq|p(q)|, \tag{2.10}$$

where x_0 is some reference point and q is a dummy integration variable.

Looking back at Eq. (2.9), and using our solution Eq. (2.10), we get

$$\frac{1}{2\pi}|d\lambda/dx| \ll 1 \tag{2.11}$$

with the de Broglie wavelength,

$$\lambda = \frac{2\pi\hbar}{p(x)}. \tag{2.12}$$

In other words, the de Broglie wavelength of the particle should not vary too quickly on the length scale of itself.

With the 0th order solution, $S_0(x)$, we move onto the next order term, substitute $S(x) = S_0(x) - i\hbar S_1(x)$ into Eq. (2.5), and get the equation

$$2iS_0'(x)S_1'(x) + iS_0''(x) = 0. \tag{2.13}$$

By substituting the solution for $S_0(x)$, (2.10), one can readily solve for $S_1(x)$,

$$S_1(x) = -\frac{1}{2}\ln[p(x)]. \tag{2.14}$$

Substituting a linear combination of S_0 and S_1 back into our ansatz, Eq. (2.3),

$$\psi(x) = \frac{C_1}{\sqrt{p(x)}}\exp\left[\frac{i}{\hbar}\int_{x_0}^{x} p(q)dq\right] + \frac{C_2}{\sqrt{p(x)}}\exp\left[-\frac{i}{\hbar}\int_{x_0}^{x} p(q)dq\right] \tag{2.15}$$

We get traveling waves with probability amplitude proportional to $1/p(x)$. Intuitively, this states that regions where the wave function has large (small) momentum, the particle has a smaller (larger) probability of being measured.

Crucially, it is important to recognize what occurs when $E < V(x)$, or what would be classically forbidden for a particle. In the region where particles would be classically forbidden, $E < V(x)$, the momentum is purely imaginary, and so our oscillating waves turn into exponentially decaying or growing functions,

$$\psi(x) = \frac{C_1}{\sqrt{i\,|p(x)|}}\exp\left[\frac{-1}{\hbar}\int_{x_0}^{x} |p(q)|\,dq\right] + \frac{C_2}{\sqrt{i\,|p(x)|}}\exp\left[\frac{1}{\hbar}\int_{x_0}^{x} |p(q)|\,dq\right] \tag{2.16}$$

This exponential decay through classically forbidden regions describes tunneling. A quick way to see this effect is for a traveling wave with energy E incident on some barrier with $E < V(x)$. The incoming wave function is,

$$\psi_{\text{incident}}(x) = Ae^{ikx} + Be^{-ikx}. \tag{2.17}$$

Inside the barrier, the solution will decay exponentially by Eq. (2.16), with $C_2 = 0$, and on the other side would be a traveling wave

$$\psi_{\text{transmitted}}(x) = Fe^{ikx} \tag{2.18}$$

By comparing incoming, $|A|^2$ and transmitted, $|F|^2$, amplitudes, one finds the probability of penetration $P = |F|^2/|A|^2$,

$$P = \exp\left[\frac{-2}{\hbar}\int_{\text{through barrier}} |p(x)|dx\right]. \tag{2.19}$$

What about an atom trapped in a barrier, rather than a particle scattering of a barrier? Given an atom trapped in a barrier, a meta-stable state in a trap, then one can approximate

the frequency with which the atom "crashes" into the barrier as

$$\nu = \left(m \oint \frac{\mathrm{dx}}{|p(x)|} \right)^{-1}, \tag{2.20}$$

with the closed loop integral signifying integration over one period of oscillation. Combining these together, one can approximate the tunneling rate, Γ of an atom in a meta-stable trap

$$\Gamma = \nu P. \tag{2.21}$$

2.3.3 Gross-Pitaevskii Equation

The derivation in this section follows closely with [68–70]. While an alternative equivalent derivation is possible via an energy functional approach [71], the derivation provided here has natural parallels to the BHH andDNLSE derivations, and makes clear where, in the derivations, physically motivated approximations occur.

In second quantization, the Hamiltonian describing an interacting bosonic system at zero temperature is given by,

$$\begin{aligned} \hat{H} = &\int d\boldsymbol{r} \hat{\Psi}^\dagger(\boldsymbol{r}) \left[\frac{-\hbar^2}{2m} \nabla^2 + V(\boldsymbol{r}) \right] \hat{\Psi}(\boldsymbol{r}) \\ &+ \frac{1}{2} \int d\boldsymbol{r} \int d\boldsymbol{r}' \hat{\Psi}^\dagger(\boldsymbol{r}) \hat{\Psi}^\dagger(\boldsymbol{r}') V_{\mathrm{int}}(\boldsymbol{r} - \boldsymbol{r}') \hat{\Psi}(\boldsymbol{r}') \hat{\Psi}(\boldsymbol{r}). \end{aligned} \tag{2.22}$$

The operator, $\hat{\Psi}$, is the bosonic field operator, with the well-known commutation relations

$$\begin{aligned} [\hat{\Psi}(\boldsymbol{r}), \hat{\Psi}(\boldsymbol{r}')] &= 0, \\ [\hat{\Psi}^\dagger(\boldsymbol{r}), \hat{\Psi}^\dagger(\boldsymbol{r}')] &= 0, \\ [\hat{\Psi}(\boldsymbol{r}), \hat{\Psi}^\dagger(\boldsymbol{r}')] &= \delta(\boldsymbol{r} - \boldsymbol{r}'), \end{aligned} \tag{2.23}$$

with the Dirac delta function, $\delta(\boldsymbol{r} - \boldsymbol{r}')$. The terms in the Hamiltonian are: the kinetic energy, $\frac{-\hbar^2}{2m}\nabla^2$, the potential energy of each constituent, $V(\boldsymbol{r})$, and the interaction energy between atoms, $V_{\mathrm{int}}(\boldsymbol{r} - \boldsymbol{r}')$.

The dynamics described by this Hamiltonian can be found by evolving the bosonic field operator using the Heisenberg evolution equation,

$$i\hbar\frac{\partial}{\partial t}\hat{\Psi} = [\hat{\Psi}, \hat{H}], \tag{2.24}$$

resulting in,

$$i\hbar\frac{\partial}{\partial t}\hat{\Psi} = -\frac{\hbar^2}{2m}\nabla^2\hat{\Psi}(\boldsymbol{r},t) + V(\boldsymbol{r})\hat{\Psi}(\boldsymbol{r},t) + \hat{\Psi}(\boldsymbol{r},t)\int d\boldsymbol{r}'\hat{\Psi}^\dagger(\boldsymbol{r}',t)V_{\text{int}}(\boldsymbol{r}-\boldsymbol{r}')\hat{\Psi}(\boldsymbol{r}',t). \tag{2.25}$$

At this point, we assume the system is sufficiently dilute with binary collisions, which results in a simple contact-interaction term, such that

$$V_{\text{int}}(\boldsymbol{r}-\boldsymbol{r}') = g\delta(\boldsymbol{r}-\boldsymbol{r}'). \tag{2.26}$$

This assumption is well-suited to describe BEC's with interaction,

$$g = \frac{4\pi\hbar^2 a_s}{m}, \tag{2.27}$$

given mass, m, and s-wave scattering, a_s [71]. Further details on BEC's in Section 2.2.

We now invoke the mean-field, or Bogoliubov, approximation. Given fluctuations away from the mean, $\hat{\xi}(\boldsymbol{r},t)$, we expand

$$\hat{\Psi}(\boldsymbol{r},t) = \Psi(\boldsymbol{r},t) + \hat{\xi}(\boldsymbol{r},t). \tag{2.28}$$

describes the condensate portion of the wave function is given by, $\Psi(\boldsymbol{r},t)$, and $\hat{\xi}(\boldsymbol{r},t)$ is the non-condensate part, which is negligible below T_c for a BEC [69]; The total number of atoms is $N = \langle|\Psi(\boldsymbol{r},t)|^2\rangle$.

Combining 2.26 and 2.28 into 2.25 gives the three dimensional Gross-Pitaevskii equation,

$$i\hbar\frac{\partial}{\partial t}\Psi(\boldsymbol{r},t) = \left[-\frac{\hbar^2}{2m}\nabla^2 + V(\boldsymbol{r}) + g|\Psi(\boldsymbol{r},t)|^2\right]\Psi(\boldsymbol{r},t). \tag{2.29}$$

2.3.4 Bose-Hubbard Hamiltonian

The BHH derivation [72, 73] begins similarly to the GPE derivation, starting with the Hamiltonian for an interacting bosonic system at zero temperature, Eq. (2.22), and using the time evolution Eq. (2.25), to arrive at Eq. (2.25) with s-wave scattering dominated contact interaction Eq. (2.27). Now, consider a potential, $V(\boldsymbol{r}) = V_{\text{lat}}(\boldsymbol{r}) + V_{\text{ext}}(\boldsymbol{r})$, where

$V_{\text{lat}}(\boldsymbol{r})$ is a periodic lattice potential and $V_{\text{ext}}(\boldsymbol{r})$ is some additional external potential.

We do not expand the bosonic field operator about a mean, but instead take advantage of the periodicity in V_{lat} to expand the bosonic field operator in the lowest Bloch band $w^{(0)}$, implicitly assuming we have a single-band model,

$$\hat{\Psi}(\boldsymbol{r}) = \sum_j \hat{b}_j w^{(0)}(\boldsymbol{r} - \boldsymbol{r}_j), \tag{2.30}$$

with the operator $\hat{b}_i^\dagger$ ($\hat{b}_i$) that creates (annihilates) a particle at site j.

Substituting Eq. (2.30) into Eq. (2.25) and assuming tight-binding gives,

$$\hat{H} = -J_{ij}^{3D} \sum_{(i,j)} \hat{b}_i \hat{b}_j^\dagger + \frac{U_{ij}^{3D}}{2} \sum_i \hat{b}_i^\dagger \hat{b}_i^\dagger \hat{b}_i \hat{b}_i + \sum_i v_i^{3D} \hat{b}_i^\dagger \hat{b}_i \tag{2.31}$$

where (i, j) is a sum over all nearest neighbors j to site i; tight-binding assumes only on-site energy, U_i^{3D}, and nearest neighbor terms, J_{ij}^{3D} contribute. The factors can be calculated using

$$J_{ij}^{3D} = -\int d\boldsymbol{r} w^{*(0)}(\boldsymbol{r} - \boldsymbol{r}_i) \left[-\frac{\hbar^2}{2m} \nabla^2 + V_{\text{lat}}(\boldsymbol{r}) \right] w^{(0)}(\boldsymbol{r} - \boldsymbol{r}_j) \tag{2.32}$$

$$U_i^{3D} = g \int d\boldsymbol{r} |w^{(0)}(\boldsymbol{r} - \boldsymbol{r}_i)|^4 \tag{2.33}$$

$$v_i^{3D} = \int d\boldsymbol{r} V_{\text{ext}}(\boldsymbol{r}) |w^{(0)}(\boldsymbol{r} - \boldsymbol{r}_i)|^2. \tag{2.34}$$

One can then reduce to a quasi-1D system using harmonic confinement, like in Section 2.3.6, to get,

$$\hat{H} = -J \sum_i (\hat{b}_i \hat{b}_{i+1}^\dagger + \hat{b}_{i+1}^\dagger \hat{b}_i) + \frac{U}{2} \sum_i \hat{n}_i (\hat{n}_i - \hat{1}) + \sum_i v_i \hat{n}_i, \tag{2.35}$$

where $\hat{n}_i = \hat{b}_i^\dagger \hat{b}_i$ is the on-site number operator.

In quasi-1D, the factors are given by

$$J = \int dx w^{*(0)}(x) \left[-\frac{\hbar^2}{2m} \frac{d^2}{dx^2} + V_{\text{lat}}(x) \right] w^{(0)}(x+a) \tag{2.36}$$

$$U = g_{1D} \int dx |w^{(0)}(x)|^4 \tag{2.37}$$

$$v_i = \int dx V_{\text{ext}}(x) |w^{(0)}(x - x_i)|^2. \tag{2.38}$$

2.3.5 Discrete Nonlinear Schrodinger Equation

TheDNLSE can be derived from both the BHH and GPE. For completeness, we present both derivations here.

First, to derive from the BHH, start with Heisenberg picture for the destruction operator $\hat{b}_k$ at site k.

$$i\hbar \frac{d}{dt} \hat{b}_k = [\hat{b}_k, \hat{H}] \tag{2.39}$$

with $\hat{H}$ from Eq. (2.35).

Using the well-known commutation relations for bosons, we get,

$$i\hbar \frac{d}{dt} \hat{b}_k = -J(\hat{b}_{k+1} + \hat{b}_{k-1}) + U \hat{b}_k \hat{b}_k^\dagger \hat{b}_k + v_k \hat{b}_k.k \tag{2.40}$$

The crucial step to get theDNLSE is assuming that each site can be described by a coherent state,

$$|z_k\rangle = e^{-|\psi_k|^2/2} \sum_n^\infty \frac{(\psi_k)^n}{\sqrt{n!}} |n\rangle \,, \tag{2.41}$$

and that we have a product state $|\Psi\rangle = \bigotimes_{k=1}^{M-1} |z_k\rangle$. In other words, there are sufficiently many bosons at any given site, that taking away a single boson doesn't impact the locate density significantly, a mean-field like approximations.

Taking the expectation value of Eq. (2.40) results in,

$$i\hbar \frac{d}{dt} \psi_k = -J(\psi_{k+1} + \psi_{k-1}) + U|\psi_k|^2 \psi_k + v_k \psi_k, \tag{2.42}$$

with, $\langle \hat{b}_k \rangle = \psi_k$ from Eq. (2.41).

Next, we derive theDNLSE from the GPE [74]. Under tight-binding approximation, expand order parameter,

$$\Psi(\boldsymbol{r},t) = \sqrt{N}\sum_j \psi_j(t)\phi(\boldsymbol{r}-\boldsymbol{r}_j), \tag{2.43}$$

with the total number of atoms, N. The function $\phi(\boldsymbol{r}-\boldsymbol{r}_j)$ is localized at $\boldsymbol{r}_j$ such that $\int d\boldsymbol{r}\phi_j^\dagger\phi_{j+1} \approx 0$ and $\int d\boldsymbol{r}|\phi_j|^2 = 1$. The local function, $\psi_j(t) \equiv \sqrt{\rho_j(t)}e^{i\theta_j(t)}$, with local phase, θ_j, local density, $\rho_j = N_j/N$, and $\sum_j N_j = N$. We will talk about "site" j, as referring to the localized area around $\boldsymbol{r}_j$. In other words, we are imposing a series of discretization points $\boldsymbol{r}_j$, or equivalently we are imposing an external lattice. For clarity, we will impose a lattice potential such that $V(\boldsymbol{r}) = V_{\text{lat}}(\boldsymbol{r}) + V_{\text{ext}}(\boldsymbol{r})$.

Insert this approximation for Ψ, Eq. (2.43), back into the GPE, Eq. (2.29), to get the 3DDNLSE. For some site, k,

$$i\hbar\frac{d}{dt}\psi_k = -J_{3D}\sum_{j\in\Omega_k}\psi_j + U_{3D}|\psi_k|^2\psi_k + v_k\psi_k, \tag{2.44}$$

with Ω_k all nearest neighbors about k. The factors are given by,

$$J_{3D} = -\int d\boldsymbol{r}\phi^*(\boldsymbol{r})\left[-\frac{\hbar^2}{2m}\nabla^2 + V_{\text{lat}}(\boldsymbol{r})\right]\phi(\boldsymbol{r}+\boldsymbol{r}_j) \tag{2.45}$$

$$U_{3D} = g\int d\boldsymbol{r}|\phi(\boldsymbol{r})|^4 \tag{2.46}$$

$$v_k = \int d\boldsymbol{r}V_{\text{ext}}(\boldsymbol{r})|\phi(\boldsymbol{r}-\boldsymbol{r}_k)|^2. \tag{2.47}$$

And finally, this can be reduced to quasi-1D to give result in Eq. (2.42), as demonstrated in the following section.

2.3.6 Quasi-1 Dimension Reduction

Here we describe how to reduce 3D equations to quasi-1D [69]. As a quick aside, the following steps can be applied with any confining potential in the y and z directions, such as a box. First, assume harmonic confinement in y, z directions,

$$V_{\text{ext}}(\boldsymbol{r}) = V(x) + \frac{1}{2}m\omega_y^2y^2 + \frac{1}{2}m\omega_z^2z^2. \tag{2.48}$$

with harmonic oscillator frequencies ω_y and ω_z. In this systems, we have length scales given by the harmonic oscillator, $a_y = \sqrt{\hbar/m\omega_y}, a_z = \sqrt{\hbar/m\omega_z}$. Define some length scale in x-direction $\tilde{L}_x$

If $\tilde{L}_x \gg a_y, a_z$ and $a_y, a_z < \xi$, with the healing length,

$$\xi^2 = \frac{1}{8\pi\rho a_s} \tag{2.49}$$

the wave function can be separated into

$$\Psi(\boldsymbol{r}, t) = \psi(x, t)\phi(y, z, t) \tag{2.50}$$

where $\phi(y, z)$ is the wave function in the transverse, xy, direction.

If we plug Eq. (2.50) into the GPE, Eq. (2.44), and then integrate out the ground-sate harmonic oscillator in y, z direction, we get the 1D GPE,

$$i\hbar\frac{\partial}{\partial t}\psi(x, t) = -\frac{\hbar^2}{2m}\frac{\partial}{\partial x}\psi(x, t) + g_{1D}|\psi(x, t)|^2\psi(x, t) + V(x)\psi(x, t). \tag{2.51}$$

For simplicity, assume $\omega_\perp \equiv \omega_x = \omega_y$, $a_\perp \equiv a_y = a_z$. The interaction parameter is now modified in 1D,

$$g_{1D} = g/2\pi a_\perp^2 = 2\hbar\omega_\perp. \tag{2.52}$$

2.4 Matrix Product State: Reduced Hilbert Space and Compression Algorithms

This section gives an overview of the time-evolving block decimation (TEBD) algorithm, and its implementation in Open TEBD [75]. These details include: the decomposition methods which allow for TEBD, the basics of time propagation, and how operators are implemented.

2.4.1 TEBD Basics: Vidal Decomposition

Time-evolving block decimation was originally introduced in [76, 77]. TEBD has been shown to be a time-adaptive density matrix renormalization group (DMRG) routine [78, 79], which can efficiently simulate 1D lowly-entangled systems, with bounds on entanglement

given by an area law [80]. The TEBD algorithm described in this subsection is implemented in Open Source TEBD [75], with a complete guide to the algorithm and open-source code available in [81]. Open Source TEBD has been superseded by Open Source MPS [82], which incorporates, and moves beyond TEBD, with methods such as variational ground state and excited ground state searches, Krylov based time-evolution, long-range Hamiltonians, and infinite-lattice variational ground state search.

The basics of the algorithm are as follows. Consider a lattice of L sites with N particles, then we can write a general state,

$$|\Psi\rangle = \sum_{i_1,i_2,\ldots,i_L=1}^{d} = C_{i_1,i_2,\ldots,i_L} |i_1\rangle |i_2\rangle \ldots |i_L\rangle \tag{2.53}$$

where i_k is an index for the kth site, d is the on-site dimension ($d = N$ would indicate no truncation), and $|i_k\rangle$ is the ith basis state on site k. To fully describe this state, we would need to fully define the d^L sized $C_{i_1,i_2,\ldots,i_L}$; this exponential scaling in lattice size becomes very prohibitive when studying more than a few atoms on more than a dozen lattice sites, where even sparse matrix methods would make an $N = L = 10$ system, with Hilbert space 11^10, difficult to simulate. One key to TEBD comes when we describe the state in Eq. (2.53) via the Vidal Decomposition. Specifically, we expand the state into local tensors $\Gamma^{[k]}$ and vectors $\lambda^{[k]}$,

$$C_{i_1,\ldots,i_L} = \sum_{\alpha_1,\cdots,\alpha_{L-1}=1}^{\chi_s} \Gamma^{[1]i_1}_{\alpha_1} \lambda^{[2]}_{\alpha_1} \Gamma^{[2]i_2}_{\alpha_1\alpha_2} \cdots \lambda^{[L]}_{\alpha_{L-1}} \Gamma^{[L]i_L}_{\alpha_{L-1}}, \tag{2.54}$$

where χ_s is the Schmidt rank, and we have assumed box-boundary conditions. A schematic of this representation is given in Figure 2.1. The tensors, $\Gamma^{[k]}$, and vectors, $\lambda^{[k]}$, are chosen such that any bipartite splitting will be exactly a Schmidt decomposition. Specifically, consider a bipartite splitting between sites k and $k+1$, then the Schmidt decomposition is given by,

$$|\Psi\rangle = \sum_{\alpha_k=1}^{\chi_{s_k}} \lambda^{[k+1]}_{\alpha_k} |\phi^{[1\cdots k]}_{\alpha_k}\rangle |\phi^{[k+1\cdots L]}_{\alpha_k}\rangle . \tag{2.55}$$

In Eq. (2.55), $|\phi_{\alpha_k}^{[1\cdots k]}\rangle$ spans the Hilbert space spanned by $\{|i_1\rangle \cdots |i_k\rangle\}$, $|\phi_{\alpha_k}^{[k+1\cdots L]}\rangle$ spans the Hilbert space spanned by $\{|i_{k+1}\rangle \cdots |i_L\rangle\}$, and $1 \leq \chi_{s_k} \leq \min(d^k, d^{L-k})$, as guaranteed by the Schmidt decomposition theorem. The value of χ_{s_k} is called the Schmidt measure, and actually gives a measure of entanglement; if $\chi_{s_k} = 1$, then the Schmidt decomposition gives a pure state, indicating that there is no entanglement between the two subsystems. Moreso, the Schmidt vectors in Eq. (2.55) are intimately related to the reduced density matrices,

$$\rho^{(1\cdots k)} = \sum_{\alpha_k=1}^{\chi_{s_k}} (\lambda_{\alpha_k}^{[k+1]})^2 \, |\phi_{\alpha_k}^{[1\cdots k]}\rangle \, \langle\phi_{\alpha_k}^{[1\cdots k]}| \tag{2.56}$$

$$\rho^{(k+1\cdots L)} = \sum_{\alpha_k=1}^{\chi_{s_k}} (\lambda_{\alpha_k}^{[k+1]})^2 \, |\phi_{\alpha_k}^{[k+1\cdots L]}\rangle \, \langle\phi_{\alpha_k}^{[k+1\cdots L]}| \tag{2.57}$$

with eigenvalues $(\lambda_{\alpha_k}^{[k+1]})^2$, which are computed using the Singular Value Decomposition (SVD).

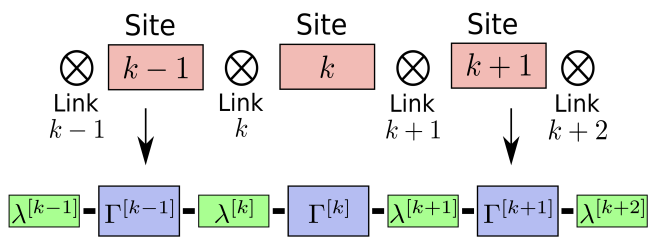

Figure 2.1: *Vidal Decomposition Schematic.* A schematic of how the Vidal decomposition takes a tensor product of lattice sites (Top) and converts it into a tensor representation (Bottom), The Γ are associated with individual sites, and the λ with the links between sites.

With the Vidal and Schmidt decompositions in hand, an approximate state can be found by truncating the sum in Eq. (2.54) to $\chi < \chi_s$, reducing the d^L dimensional parameters in Eq. (2.53) to $d\chi^2 L + \chi(L+1)$ dimensional parameters, and furthermore the local dimension d can be truncated. This truncation in χ is an appropriate approximation for lowly-entangled systems because the SVD results in singular-values which decay exponentially, a large amount of values can be discarded with minimal error [78]. In other words, TEBD works in an adaptive Hilbert space, keeping the mostly highly entangled states. The

discarded eigenvalues are called the discarded weight, or Schmidt error, and is calculated as,

$$\tau_k = 1 - \sum_{\alpha_k=1}^{\chi} (\lambda_{\alpha_k}^{[k+1]})^2 \tag{2.58}$$

with $\sum_{\alpha_k=1}^{\chi_s} (\lambda_{\alpha_k}^{[k+1]})^2 = 1$. Thus, exponentially decaying λ allows Eq. (2.58) to be arbitrarily small for large enough χ. Beyond a user chosen χ, Open Source TEBD also truncates any values with $\lambda_{\alpha_k} < 10^{-10}$. This truncation allows the code to work efficiently since implementations in this thesis often have many sites (beyond the trapping barrier) which have little-to-no occupation for a majority of the simulation, and thus have little-to-no entanglement.

2.4.2 Time Propagation

Time propagation, both real and imaginary, is performed using the 4th order Suzuki-Trotter expansion of the BHH. For simplicity, we describe the 2nd order Suzuki-Trotter expansion, and outline extrapolating to 4th order. The basic idea behind this scheme of time propagation is that we can split the Hamiltonian into parts which operate on even and odd sites, which allows the time-propagation operator to be written as,

$$\hat{U}(\delta t) = \exp\left[\frac{-i\delta}{\hbar}\left(\sum_{k:\text{odd}} \hat{H}_k + \sum_{k:\text{even}} \hat{H}_k\right)\right]. \tag{2.59}$$

Since $\hat{H}_k$ and $\hat{H}_{k+1}$, neighboring operators, are not guaranteed to commute, Eq. (2.59) will not in general factorize, and so the 2nd order Suzuki-Trotter expansion [83] is used,

$$\hat{U}(\delta t) = \hat{U}_{\text{odd}}(\delta t/2)\hat{U}_{\text{even}}(\delta t)\hat{U}_{\text{odd}}(\delta t/2) + O(\delta t^3) \tag{2.60}$$

$$\hat{U}_{\text{odd}}(\delta t/2) = \prod_{k:\text{odd}} e^{-i\hat{H}_k \delta t/2\hbar} \tag{2.61}$$

$$\hat{U}_{\text{even}}(\delta t) = \prod_{k:\text{even}} e^{-i\hat{H}_k \delta t/\hbar}. \tag{2.62}$$

The operator given by Eq. (2.60) will then propagate $|\Psi\rangle$ forward in time an amount δt, with a truncation error of $O(\delta t^3)$; the operation involves three total sweeps of the system, two for odd sites, Eq. (2.61), each for $\delta t/2$, and once for even sites, Eq. (2.62). After each

time step, TEBD evaluates the Vidal decomposition, Eq. (2.54), with a truncation $\chi < \chi_s$, usually $\chi \in (40, 220)$ depending on N, L, and interaction strength U in the BHH. Since TEBD continuously adopts the Hilbert space on which it functions, it is a time-adaptive DMRG.

Generalizing this method to the 4th order Suzuki-Trotter expansion involves replacing Eq. (2.60) with the Forest-Ruth formula,

$$\begin{aligned}\hat{U}(\delta t) =& \hat{U}_{\text{odd}}(\theta\delta t/2)\hat{U}_{\text{even}}(\theta\delta t)\hat{U}_{\text{odd}}((1-\theta)\delta t/2) \\ & \hat{U}_{\text{even}}((1-2\theta)\delta t)\hat{U}_{\text{odd}}((1-\theta)\delta t/2)\hat{U}_{\text{even}}(\theta\delta t) \\ & \hat{U}_{\text{odd}}(\theta\delta t/2) + O(\delta t^5)\end{aligned} \tag{2.63}$$

where $\theta = 1/(2 - 2^{1/3})$ is the Forest-Ruth parameter, and the even/odd operators are still given by Eqs. (2.61) and (2.62). Although the 4th order expansion, Eq. (2.63), now requires 7 sweeps across the lattice, we can use a more coarse time-step δt than for the 2nd order expansion since we have $O(\delta t^5)$ error.

Ground states in Open Source TEBD are found by propagating an initial guess wave function $|\Psi_{\text{guess}}\rangle$ in imaginary time. Imaginary time propagation (ITP), i.e. taking $t \to it$, makes higher energy states decay, leaving the lowest energy states. Thus, an appropriately chosen $|\Psi_{\text{guess}}\rangle$, with enough overlap with the true ground state $|\Psi_{\text{GS}}\rangle$, will give a good approximation for a large enough ITP. The ITP algorithm is as following

1. Define a guess wave function $|\Psi_0\rangle$
2. Propagate in ITP a user-defined number of steps n, $|\Psi_1\rangle = (\hat{U}(i\delta t))^n |\Psi_0\rangle$
3. Normalize the new state $\langle\Psi_1|\,|\Psi_1\rangle = 1$
4. Calculate the largest $\lambda^{[k]}_{\alpha_{\max}}$ at all k links for the new state.
5. Calculate the difference in $\lambda^{[k]}_{\alpha_{\max}}$ between new $|\Psi_1\rangle$ and previous state $|\Psi_0\rangle$ for all k links, and take the largest of these difference.
   (a) If difference in these $\lambda^{[k]}_{\alpha_{\max}}$ is smaller than some tolerance, the state is considered converged.

(b) Otherwise, repeat from Step 2, now propagating $|\Psi_1\rangle$.

Convergence in the above algorithm is highly dependent on the initial state, and so the algorithm is applied twice. Initially, Open Source TEBD runs through the ITP algorithm with some convergence tolerance $O(10^{-3} \backsim 10^{-5})$ in step 5, and then reruns the whole algorithm with a finer tolerance $O(10^{-5} \backsim 10^{-8})$. Initial sweep creates a very rough state, which is then refined by the second sweep. To achieve meta-stable states trapped in a relatively small portion of the lattice see Section 4.3.

2.4.3 Operators

TEBD gives access to many quantum operators, of particular interest being entanglement and quantum fluctuations. Operators which can be simulated by Open Source TEBD are single and two site operators, and involves modifying the appropriate tensors and vectors in Eq. (2.54). Consider a single-site unitary operator acting on the kth site

$$\hat{U}_k = \sum_{i_k, i'_k} U_{i_k, i'_k} \left| i_k \right\rangle \left\langle i'_k \right| . \tag{2.64}$$

The effect of Eq. (2.64) is simply to alter the tensor at site k, creating the new tensor defined by

$$\tilde{\Gamma}^{[k] i_k}_{\alpha_{k-1} \alpha_k} = \sum_{i'_k} U_{i_k, i'_k} \Gamma^{[k] i'_k}_{\alpha_{k-1} \alpha_k} . \tag{2.65}$$

Two-site operators are computationally more intensive. Consider a two-site unitary operator defined by

$$\hat{V}_{k,k+1} = \sum_{i_k, i_{k+1}; i'_k, i'_{k+1}} V^{i'_k, i'_{k+1}}_{i_k, i_{k+1}} \left| i_k i_{k+1} \right\rangle \left\langle i'_k i'_{k+1} \right| . \tag{2.66}$$

Applying Eq. (2.66) to a state $|\Psi\rangle$ now alters the tensors on both sites, as well as the vector (often referred to as the link) between them as follows. First, rewrite Eq. (2.54) using a bipartite splitting to separate out the k and $k+1$ sites

$$\left| \Psi \right\rangle = \sum_{\substack{\alpha_{k-1}, \alpha_{k+1}, \\ i_k, i_{k+1}}} \Theta^{i_k i_{k+1}}_{\alpha_{k-1} \alpha_{k+1}} \left| \phi^{[1 \cdots k]}_{\alpha_{k-1}} \right\rangle \left| i_k i_{k+1} \right\rangle \left| \phi^{[k+2 \cdots L]}_{\alpha_{k+1}} \right\rangle . \tag{2.67}$$

For convenience we have defined the object,

$$\Theta^{i_k i_{k+1}}_{\alpha_{k-1}\alpha_{k+1}} = \lambda^{[k]}_{\alpha_{k-1}} \Gamma^{[k]i_k}_{\alpha_{k-1}\alpha_k} \lambda^{[k+1]}_{\alpha_k} \Gamma^{[k+1]i_{k+1}}_{\alpha_k\alpha_{k+1}} \lambda^{[k+2]}_{\alpha_{k+1}}, \tag{2.68}$$

which makes the effect of the two-site operator more clear. Simply, operating Eq. (2.66) on the state Eq. (2.67) modifies Θ, essentially the tensors on sites k and $k+1$, as well as the link between them,

$$\tilde{\Theta}^{i_k i_{k+1}}_{\alpha_{k-1}\alpha_{k+1}} = \sum_{i'_k, i'_{k+1}} V^{i'_k, i'_{k+1}}_{i_k, i_{k+1}} \Theta^{i_k i_{k+1}}_{\alpha_{k-1}\alpha_{k+1}} \tag{2.69}$$

$$= \sum_{\alpha_k} \lambda^{[k]}_{\alpha_{k-1}} \tilde{\Gamma}^{[k]i_k}_{\alpha_{k-1}\alpha_k} \tilde{\lambda}^{[k+1]}_{\alpha_k} \tilde{\Gamma}^{[k+1]i_{k+1}}_{\alpha_k\alpha_{k+1}} \lambda^{[k+2]}_{\alpha_{k+1}}. \tag{2.70}$$

The numerical implementation for the two-site operators requires several steps, including normalization and SVD, which details can be found in [81].

CHAPTER 3

MACROSCOPIC QUANTUM TUNNELING ESCAPE OF BOSE-EINSTEIN CONDENSATES

This chapter contains follow up work to the first experimental realization of atom-atom interactions altering macroscopic quantum tunneling dynamics of a BEC [84] and is published in Physical Review Letters A. [13]. I acknowledge all collaborators on this project. Xinxin Zhao as the primary author of the manuscript, and the lead on mean-field classical spilling variational Lagrangian dynamics calculations, which were not included in the published manuscript but are in the PhD thesis [85]. Marie A. McClain, for work on writing and editing the manuscript, and helping with calculations. Kenji Maeda and Lincoln D. Carr for laying the groundwork on the modified JWKB and variational Lagrangian calculations. Shreyas Potnis, Ramon Ramos, and Aephraim M. Steinberg, for undertaking the experiment and giving feedback on the manuscript. My contributions to the work include: leading the JWKB calculations, providing the effective mean-field calculations, writing the published manuscript subsection IV.A., for the modified JWKB model, and published manuscript section V., for the effective mean-field model, and reviewing the complete manuscript for accuracy and clarity.

3.1 Interaction Assisted Non-Exponential Macroscopic Quantum Tunneling of a Bose-Einstein Condensate

A BEC of $O(5 \times 10^5)$ rubidium atoms underwent quantum tunneling out of meta-stable trap, schematically depicted in Figure 3.1. The trap is given by the potential,

$$\begin{aligned} V(x,y,z) &= \frac{1}{2}m\omega_x^2 x^2 + \frac{1}{2}m\omega_z^2 z^2 - may + V_{\mathrm{b}}(x,y,z) \\ V_{\mathrm{b}}(x,y,z) &= V_0 \exp\left(-2y^2/\omega(z)^2\right) \\ \omega(z) &= \omega_0 \left(1 + (z/z_{\mathrm{R}})^2\right)^{\frac{1}{2}} . \end{aligned} \tag{3.1}$$

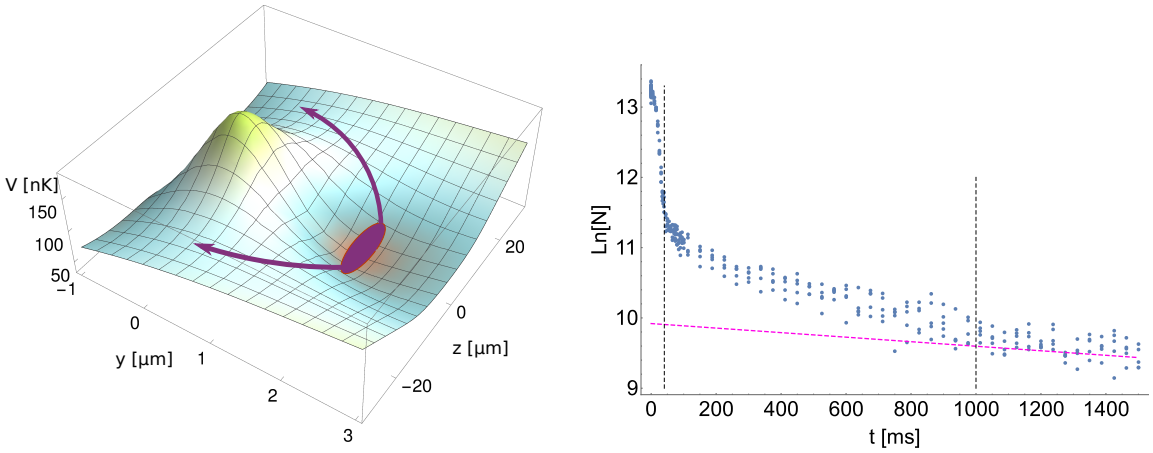

(a) (b)

Figure 3.1: *Macroscopic Quantum Tunneling Experiment.* (a) Experimental 3D potential with a barrier height of 190 nK (peak height) in the weak configuration. The distance between saddle points to the potential minimum is $x_0 = 18(1)\,\mu$m. Sketched is a BEC trapped in the local minimum of the potential (purple ellipse) escaping via the weakest part of the potential (purple arrows). (b) Experimental data, in number of trapped atoms N, exhibits a non-exponential decay, in contrast to the exponential background decay due to atomic losses (pink nearly-horizontal dashed line). The vertical dashed lines divide the experimental dynamics into the three dominant regions of classical spilling, MQT, and background decay.

This trap is formed by harmonic confinement in the x and z coordinates, a linear ramp in the y coordinate with constant acceleration, α, due a magnetic gradient and gravity, and a Gaussian beam with waist, $\omega(z)$. Purple arrows schematically depict the energetically favorable paths for quantum escape Figure 3.1(a); through the weakest points in the potential. Typical experimental data, Figure 3.1(b), shows 3 distinct regions; pink line shows background loss. The first region, approximately the first 40 milliseconds, has a rapid loss of atoms occurring when the harmonic confinement in the y axis is turned off and the chemical potential is higher than the barrier. Afterwards, up to 1,000 milliseconds, tunneling dominated dynamics shows non-exponential decay. Finally, beyond 1,000 milliseconds, background loss, depicted by the pink dashed line, becomes the dominant factor in population decay.

We develop a modified one-dimensional JWKB model which can capture the observed non-exponential decay. It has been shown that complex tunneling dynamics in three-dimensional potentials can simplify to effective one-dimensional tunneling by averaging over

semi-classical trajectories in the trap and approximating tunneling through the barriers via JWKB [48]. Specifically, complicated tunneling dynamics in a multi-dimensional potential can be characterized by tunneling through the weakest point in the barrier, similar to water bursting through the weakest point in a dam. The simplified JWKB model is as follows. To reduce the problem into one-dimension, we take the schematic 1D path in Figure 3.1(a), the shortest path from the center-minimum of the well to the weakest point in the barrier, the lowest point over the saddle, as our effective 1D tunneling path. This 1D slice through the potential is simplified as two triangle barriers separated by some distance, described in Section 3.3. This simplification allows for more tractable analytical calculations, and the dynamics in the well are reduced to semi-classical oscillation between these two barriers.

3.2 Modeling Effective One Dimensional Mean-Field JWKB Quantum Tunneling

Escape from the trap can be described by the tunneling and loss rates in the decay equation

$$\dot{N}(t) = -(\Gamma_{\text{tunn}} + \Gamma_{\text{bg}})N(t) = -\Gamma N(t). \tag{3.2}$$

Background loss rate is measured to be $\Gamma_{\text{bg}} \approx 0.31(0.02)\,\text{Hz}$. The tunneling probability, Γ_{tunn}, determines how the BEC escapes, with constant probability giving simple exponential decay.

To calculate, Γ_{tunn}, we use two offset triangle barriers as the effective 1D potential; we find a square barrier does not reproduce the experimental results, and a Gaussian barrier does not improve the accuracy of the model, while increasing analytical complication. A triangle barrier will have a tunneling rate that decreases as the number of trapped atoms and chemical potential decreases and is analytically tractable. It turns out, in order for this model to reproduce dynamics throughout the entire experiment, the time-dependent mean-field effects are included with a time dependence in the height of the triangle potential, motivated by the mean-field effective potential, $V_{\text{eff}}(x) = V(x) + g|\psi(x,t)|^2$. The triangle

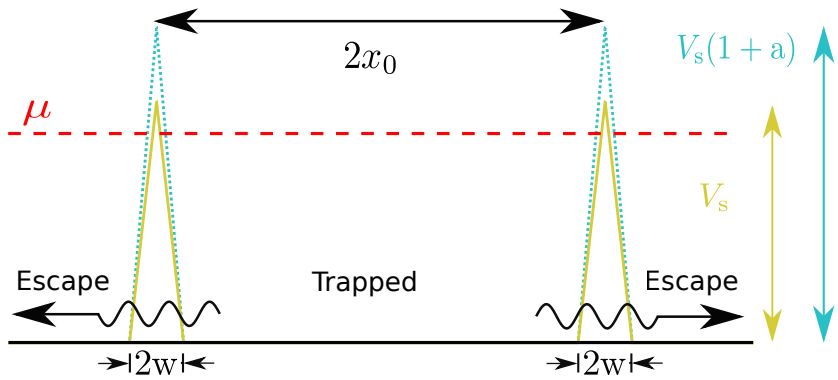

Figure 3.2: *JWKB Potential Schematic.* Tunneling in the full 3D experimental potential can be modeled with a much simpler 1D approach. The minimal feature set required to fit the data is (1) a bare 1D triangle potential of height V_s and width $2w$ (gold, solid); (2) inclusion of the mean-field to create an effective potential of height $V_s(1+a)$ with $a \propto N(t)$ (teal, dotted); and (3) use of the Thomas-Fermi approximation for the chemical potential $\mu \propto N^{1/3}$ (red dashed line). Such a choice of model provides self-consistency between the replacement of E with μ in the usual JWKB treatment, together with the bare $V(x)$ with the effective potential $V_{\text{eff}}(x) = V(x) + g|\psi|^2$.

height, V_s, and separation, $2x_0$, are determined from the experiment, with the two free parameters, full width at half maximum, w, and a unitless mean-field parameter, a.

$$\begin{aligned} V_{\text{eff}}(x,t) &= \begin{cases} -\frac{V_{\text{mf}}}{w}|x \pm x_0| + V_{\text{mf}}, & |x \pm x_0| < w, \\ 0, & \text{otherwise}, \end{cases} \\ V_{\text{mf}} &= V_s\big[1 + a\frac{N(t)}{N_0}\big]. \end{aligned} \tag{3.3}$$

The barrier, V_{mf}, is a dynamic effective barrier, which approaches V_s as atoms escape, schematic in Figure 3.2.

Using the JWKB approximation, Section 2.3.2, the tunneling probability, using the effective mean-field triangle model, $V_{\text{eff}}(x,t)$, is,

$$\Gamma_{\text{eff}} = \frac{P_{\text{eff}}}{\tau_{\text{eff}}}. \tag{3.4}$$

$$P_{\text{eff}} = \exp\left(-\frac{8}{3\hbar} w \sqrt{2mV_{\text{mf}}} \left(1 - \frac{\mu}{V_{\text{mf}}}\right)^{3/2}\right) \tag{3.5}$$

$$\tau_{\text{eff}} = \sqrt{2m}\frac{(x_0 - w)}{\sqrt{\mu}} + 2\sqrt{2m}\frac{w\sqrt{\mu}}{V_{\text{mf}}}. \tag{3.6}$$

The tunneling probability, Eq. (3.5), and semi-classical oscillation frequency, Eq. (3.6), give the tunneling rate Eq. (3.4). Similar to the complex scaling method [86], this gives a time dependent tunneling rate Γ. And finally, the chemical potential is found to be described well by the Thomas-Fermi approximation, giving

$$\mu = bN^{1/3}, \tag{3.7}$$

with $b = 1.15(8)$ nK [84]. Putting this all together to fit the data, we solve the decay equation, Eq. (3.2), with $\Gamma_{\text{tunn}} = \Gamma_{\text{eff}}$, Eq. (3.4), and the chemical potential, Eq. (3.7). This is a minimal model which captures the experimental results, and may be absorbing and hiding many-body effects, Section 3.4. The addition of the time-dependent mean-field parameter allows for self-consistency with the Thomas-Fermi approximation for the chemical potential [87, 88].

3.3 Results and A Case Study

We examine our results in detail for $V_{\text{s}} = 190$[nK], with the case study Figure 3.3, and all fits shown in Figure 3.4. Our model fits the data from the mean-field assisted tunneling region through the background-loss dominated regions. Spilling over the top of the well dominates dynamics during the first 40 ms; a variational Lagrangian method was used to analyze this period but is beyond the scope of this thesis [85]. Tunneling dominates thereafter, up to 1s, and background loss for all later measurements. The first region, portion A, begins when the chemical potential falls below the barrier saddle height. Although there are surely complex dynamics inside the potential, possibly chaotic semi-classical paths, our effective 1D

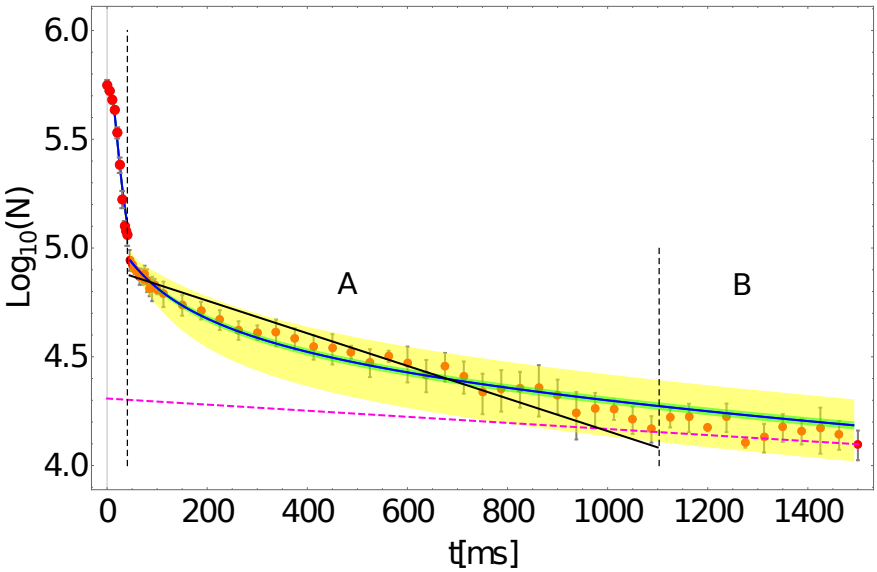

Figure 3.3: *Case Study: Theoretical Model Fit to Macroscopic Quantum Tunneling Data.* Experimental number of trapped atoms as a function of time (red circles: mean values with 1σ error bars) with theoretical fit (solid blue curve), exponential fit through tunneling dominated regime (dash dot black line), and experimental background loss (dashed pink nearly-horizontal line). We divide the decay curve into three sub-regions (indicated by dashed vertical lines): initial transient classical spilling, (A) mean-field assisted quantum tunneling region with non-exponential decay, and (B) background loss dominated region. The green (dark gray) envelope indicates uncertainty in fitting parameters from modified JWKB. The yellow (light gray) envelope indicates combined uncertainty due to: uncertainty in experimental parameters, uncertainty in data, and uncertainty in fit parameters.

model can reproduce the experimental decay dynamics. As a comparison, an exponential fit has reduced chi values of $\chi^2 = 3.32$ and only covers the tunneling dominated region, while our model has $\chi^2 = 1.21$ and fits to the end of the data. The model captures the mean-field effective barrier changing shape in time, which gives faster decay at early times, when repulsive mean-field interactions are stronger. All barrier fits Figure 3.4, show non-exponential decay. Background loss becomes increasingly significant for more trapped atoms from larger barriers.

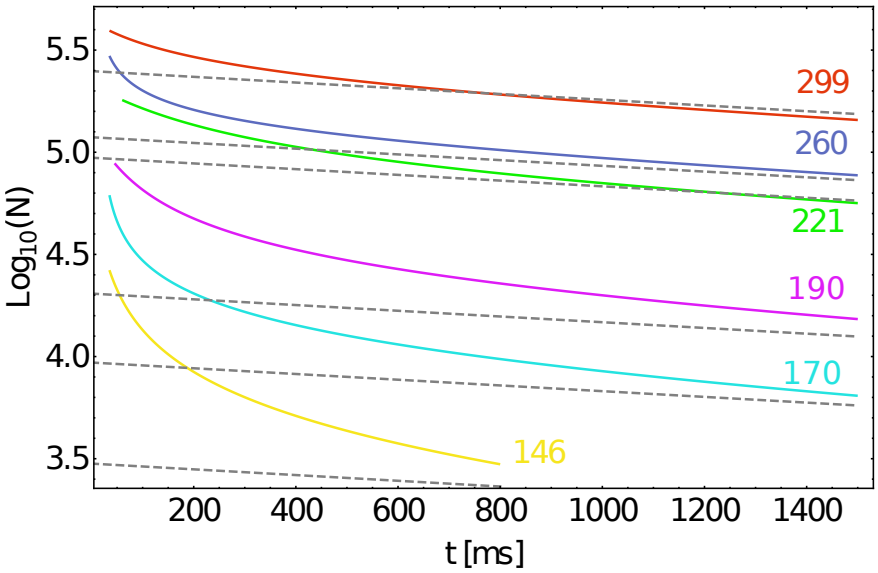

Figure 3.4: *Theoretical Fits of Trapped Particle Number for Weak Configurations.* All fits demonstrate same trends as the case study in Fig. Figure 3.3. Gray dashed lines represent background loss for each barrier height. Colors indicate barrier heights for weak configuration, in nanokelvin.

The results for the fitting parameters is given in Figure 3.5. In general, both the triangle width, w, and effective barrier height, $V_{\mathrm{s}}(1+a)$, increase for larger barriers. The barrier height to the saddle, V_{s}, was taken directly from the experimental data, and is around 1/3rd of the Gaussian peak height. The modified barrier height at the start of tunneling, $V_{\mathrm{s}}(1+a)$, is larger than the saddle height Figure 3.5(a), with an increase of roughly 10 to 30%. Physically, taller experimental potentials can hold more atoms, increasing mean-field interactions, which results in larger a, and slower tunneling rates. One exception to this

trend is the barrier with height 260[nK]. Unaccounted for experimental error is suspected to be the cause; visible in the fact that the number of initially trapped atoms, at $t = 0$, is $N_0 \approx 583,000$ for $V_0 = 260$[nK], which is close to $N_0 \approx 560,000$ with $V_0 = 190$[nK], while $N_0 \approx 630,000$ for $V_0 = 221$[nK]. This result is supported by further analysis on the tight configuration, detail of which are left out of this chapter for clarity, see [13].

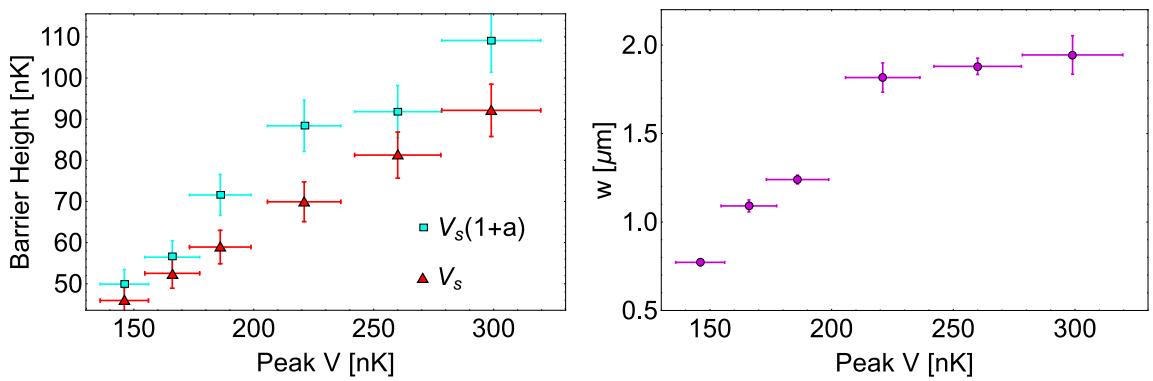

(a) (b)

Figure 3.5: *Fitting Results in Quantum Tunneling Regime.* Optimized values of (a) effective saddle height (teal squares) at start of tunneling dynamics in comparison to the experimentally measured bare saddle height (red triangles) vs. the bare peak height, showing how mean-field effects significantly correct the tunneling dynamics. (b) Effective potential width w for the weak configuration. Both the effective width and height increase as a function of bare experimental barrier height V.

The sources of error in Figure 3.3 are: the initial trapped number in the tunneling region, δN_0 near $t \approx 40[\mu s]$, and experimental uncertainty in the barrier height, δV_s. Generally, the initial number and trap height accounted for $O(10^3$ to $10^4)$ of the total error envelope during the first 100[μs]. Beyond this time, the barrier height uncertainty contribution remains the same, while the initial number error contribution reduces by 1-2 orders of magnitude, because the mean-field interaction strength decreases as fewer atoms remain. All other errors are generally at least one order or magnitude smaller than the barrier height uncertainty.

3.4 Hidden Many-Body Physics

The success of the modified JWKB model with mean-field interactions might be capturing, and thus hiding, many-body physics. In this section we show how a renormalized mean-field is able to capture many-body tunneling in the BHH.

Many-body features like fluctuations, fragmentation, and depletion result in the failure of straight-forward mean-field models in both BEC's and nonlinear optics. To move beyond a straight-forward treatment, multi-node and large vector nonlinear Schrodinger equations describing multi-component optical systems have been shown to be well modeled by a scalar GPE-like effective equation, i.e., a renormalization of the mean-field interaction, by several equivalent methods [89–102]. The success in nonlinear optics, and analogous behavior between BEC's at finite temperature to incoherent light in nonlinear media [103], suggest that depleted and fragmented BEC's may be successfully described by a renormalization of the interaction parameter in a scalar mean-field model, i.e., modifying g in the GPE.

Consider N bosons trapped in a lattice, described by the BHH for many-body dynamics and the DNLSE for mean-field dynamics; like Section 4, but with some key differences to more closely match the experiment. For both mean-field and many-body, a ground state is found with an external potential of height $h = 0.15$[J], and the trapping well covering sites 1 to 15. The barrier is non-adiabatically reduced to a height of $h = 0.10$[J] over sites 16 to 19 at the start of the dynamics, to mimic the experiment, and to create strong fragmentation of the wave function. We consider the interaction strength, $NU/J = 1$, which in a straight-forward mean-field would correspond to $g = 1$ in the DNLSE. In Figure 3.6(a) the straight-forward mean-field treatment, $g = 1.0$, predicts faster tunneling than the BHH. However, a renormalized mean-field interaction, by 23 to 28%, can bound dynamics from above and below. Early times, up to $t \approx 50$, $g = 0.77$ closely following the many-body curve. After this point, the many-body results are closer to $g = 0.72$ curves.

Figure 3.6(b), single-particle density matrix eigenvalues demonstrate the many-body nature of the dynamics. The largest eigenvalue encompasses the largest BEC mode. The second

mode shows fragmentation of up to 30%, while the steady growth in the sum of remaining eigenvalues, $\lambda_{\geq 3}$, shows depletion of up to 10% by $t = 200$. That $\lambda_{\geq 3}$ grows much slower than the two dominant eigenvalues decrease indicates that many modes are being excited and occupied. Despite these facts, the renormalized mean-field can bound the decay dynamics. Taken as error bars, the renormalized mean-field curves would amount to a relative error of $O(10^{-3})$, which would be well within the error bars of many tunneling experiments.

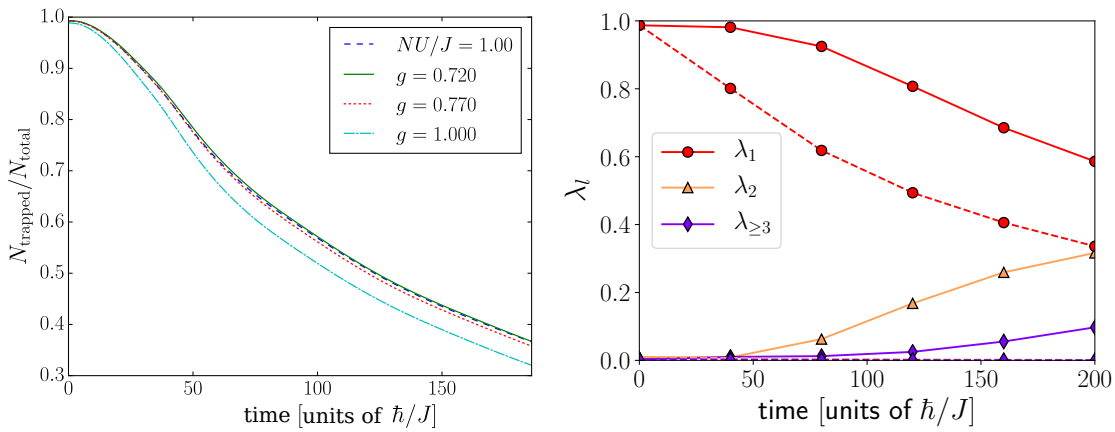

(a) (b)

Figure 3.6: *Effective Mean-Field, Many-Body, and Depletion* (a) Normalized trapped atoms for many-body ($NU/J = 1.00$, dashed curve) is bounded from above and below by effective values $g = 0.72$ (green, upper dark gray curve) and $g = 0.77$ (dotted curve) respectively, while direct mean-field comparison $g = 1.00$ (teal, the lowest dark gray curve) under-predicts. (b) Semi-log two largest eigenvalues (λ_1,λ_2) and sum of remaining eigenvalues $\lambda_{\geq 3}$ of the single-particle density matrix for the total system (solid lines) and trapping well (dashed lines) are plotted versus time. The wavefunction has large occupation of two modes over the whole system (solid lines), with 10% depletion as noted by non-zero $\lambda_{\geq 3}$. Points represent actual data with error bars smaller than marker, and lines are a guide to the eye.

3.5 Conclusions

In this chapter, we use a modified JWKB model, which accounts for mean-field interactions, to capture the experimentally observed non-exponential decay in a Bose-Einstein condensate tunneling out of a meta-stable state. The JWKB model supports the experimental findings, requiring a dynamic mean-field barrier height to capture the non-exponential

decay. Two fit parameters, the barrier width, and effective mean-field interaction, elucidated the how the experimental trap is modified for larger wells and more trapped atoms. The mean-field barrier height increases with the density of trapped atoms, reflecting the repulsive interactions between atoms. The fit parameters also point out unaccounted experimental error in one of the barrier configurations. We also demonstrated how mean-field systems can have hidden many-body physics, using a renormalized scalar mean-field equation to bound many-body dynamics in the Bose-Hubbard Hamiltonian. The renormalized mean-field analysis supports results in nonlinear optics, that multi-component BECs can be adequately described by a renormalized scalar equation.

CHAPTER 4

ENTANGLED DYNAMICS IN MACROSCOPIC QUANTUM TUNNELING OF BOSE-EINSTEIN CONDENSATES

The work presented in this chapter is a continuation and completion of work started by co-author Joseph A. Glick III, master's thesis [104]. The completed work is published in Physical Review Letters [36]. This project analyzes a superfluid-dominated bosonic many-body meta-stable wave function quantum tunneling into free-space, modeled by the BHH, and compared to mean-field simulations, modeled by theDNLSE. My major contributions to this work include: extending the atom-atom interactions into the repulsive interaction regime, demonstrating the explicit convergence of many-body to mean-field dynamics, simulating sufficiently large lattices to approximate escape to free-space, finding scaling laws in several observables, i.e., escape times deviating from well-known exponential dependence for strong interactions, and extensively rewriting the original preprint [105]. All data in this chapter and the published manuscript were simulated by me, using code I modified from Open Source TEBD code [75, 82].

This chapter is outlined as follows. Section 4.1 presents motivations and introduces the models used for the many-body and mean-field dynamics, convergence in many-body dynamics to mean-field escape time, quantifying many-body quantum measures like entropy, depletion, and density-density correlations, and measuring different time-scales in these measures–such as the time at which entanglement is maximized–and their scaling with interaction. Section 4.3 covers the techniques used to achieve large N and large lattice L simulations. And finally, conclusions in Section 4.4.

4.1 Quantum tunneling of a Superfluid from Single Particle to Many-Body Entangled Dynamics

Experimentally and numerically, researchers have access to a wide range of quantum observables, from a single atom to hundreds of thousands of atoms in BEC's[16, 53, 82, 106–109]. We explore how tunneling dynamics of quantum escape is altered from a single atom, to many-body dominated, to mean-field dominated interactions. While Chapters 5 and 6 explore this topic for interactions from the Mott to Superfluid quantum phase transition, in both the Double-Well and Tunneling Escape configurations, here we limit ourselves to the escape problem for superfluid dominated, $U/J < (U/J)_{\text{critical}}$, dynamics.

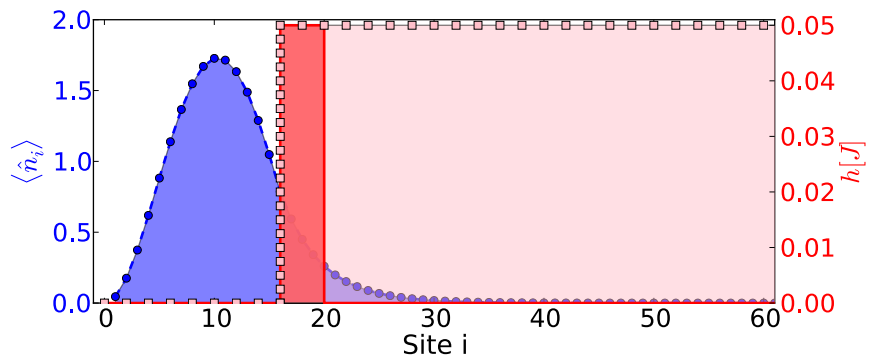

Figure 4.1: *Initial Quasibound State.* The many-body wavefunction for $N = 20$ with $NU/J = +0.15$ (blue shaded region, points show actual TEBD results for the density average $\langle \hat{n}_i \rangle$) is first localized to the left behind the barrier (red line, red and pink shaded areas) via relaxation in imaginary time with a barrier of height h and initial width w_I. The barrier is reduced to width w (solid red line, red shaded area) at $t = 0$ in real time propagation, so that the now quasibound Bose gas can begin macroscopic quantum tunneling. The hard wall at the left and relatively small barrier area push the density tail to partially extend into the barrier.

Many-body dynamics are calculated using TEBD to simulate the BHH and mean-field dynamics are calculated via theDNLSE. The bosons are initially trapped in a meta-stable state, in a well of fixed width, 15 sites, behind a barrier of fixed height, $h = 0.05$[J], with a width of $w = 1$ to $w = 5$ sites, Figure 4.1. In order to compare many-body and mean-field simulations, the number of atoms, N, and the interaction strength, U, are scaled by setting $NU/J \equiv$ const., for a constant ranging from ± 0.15 to ± 0.60. The motivation is

that as $N \to \infty$ and $U \to 0$, while holding NU/J constant, the BHH limits the mean-field. We are able to show this is the case while staying within superfluid-dominated interactions, $U/J << (U/J)_c \approx 3.28$. As we're able to show in Chapters 5 and 6, mean-field fails when interactions U are dominated by the Mott Insulator. We explicitly show mean-field convergence going from $N = 1$ to $N = 80$ atoms. These parameter ranges were chosen to allow for tunneling times observable withing a few hundred seconds. We are able to simulate sufficiently large lattices for pseudo-free-space escape, finite lattices that are large enough to simulate free-space, using the methods in Section 4.3.

4.2 Quantum Observable Dynamics and Scaling

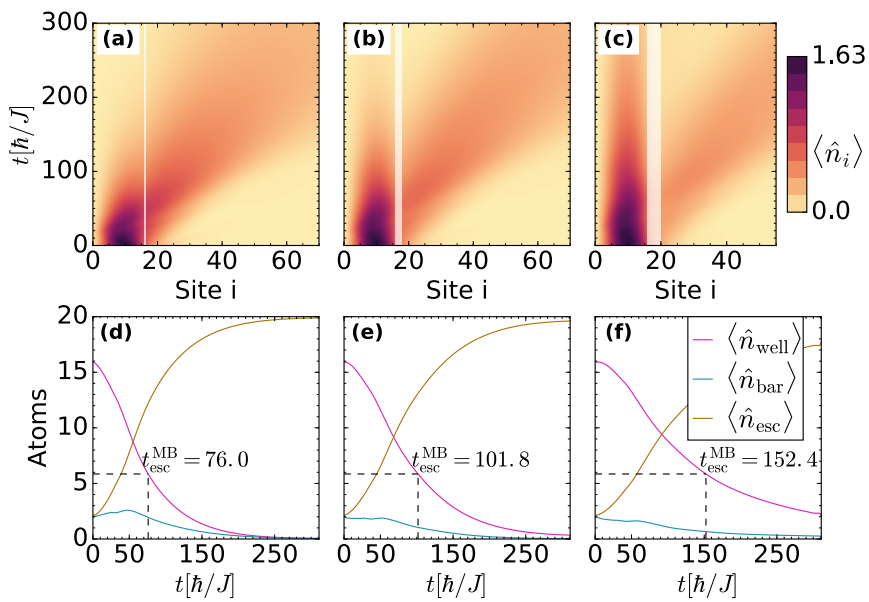

Figure 4.2: *Many-Body Tunneling and Escape Times.* Barrier widths (a,d) $w = 1$, (b,e) $w = 3$, and (c,f) $w = 5$. Top row: average atom number per site. Bottom row: number in well $\langle \hat{n}_{\text{well}} \rangle$ (magenta), number in barrier $\langle \hat{n}_{\text{bar}} \rangle$ (cyan), and escaped $\langle \hat{n}_{\text{esc}} \rangle$ (tan) atoms; the many-body escape times ($t_{\text{esc}}^{\text{MB}}$) all ± 0.1. All plots for $NU/J = +0.30$ with $N = 20$.

Figure 4.2 gives a qualitative overview of the gross features of tunneling. The ground state for each subfigure is identical, with only the barrier area altering dynamics. Lattices are large enough, $L \geq 250$, so that reflections from end of lattice do not return and interfere with escaping atoms. Qualitatively, all barriers have a large initial escape of atoms, which spread

out into the lattice Figure 4.2(a-c). The largest visible differences between the different barrier widths in Figure 4.2(a-c), is that the density of the initially released atoms is larger, and that after $t \approx 100$ in Figure 4.2(c), the density of escaping atoms is very small, although there are still atoms escaping according to Figure 4.2(d). The tunneling time, t_{esc}, when the total number of trapped atoms as reaches $1/e$ of the initial number, increases with the barrier width Figure 4.2(d-f), approximately doubling from $w = 1$ to $w = 5$. This is to be expected, since tunneling rates decrease for larger barrier areas. For the smallest barrier, $w = 1$, the number of atoms inside the barrier, $\langle \hat{n}_{\text{bar}} \rangle$, at any given time increases for the first 50 seconds, as the repulsive interactions inside the well force atoms quickly through the barrier Figure 4.2(d). Note that the number density inside the barrier is much lower, occupying a single site versus 5 sites. Although all subfigures are for repulsive interactions, attractive interactions are similar, with slight differences: the spread in escaped atoms is smaller, tunneling is slower, and maximal on-site occupancy, which is ($\langle \hat{n}_i \rangle \approx 1.63$ for repulsive, is larger.

Escape times are quantified for various barrier areas, showing how the BHH andDNLSE differ in escape time when N is small. Tunneling times increase with barrier areas for both attractive and repulsive interaction. The change in interaction strength has larger effect on attractive interactions. From $NU/J = +0.15$ to $NU/J = +0.30$, repulsive interaction tunneling times decrease by around 15%, while attractive interaction times increase by upwards of 30% for the largest barriers. Figure 4.3(a,b) many-body escape times converge to mean-field escape times for both repulsive and attractive interactions Figure 4.3(c). Attractive (repulsive) interactions slow down (speed up) tunneling; interactions in the well try to "pull in" atoms towards the peak, keeping atoms trapped longer. Depletion in Figure 4.3(d) shows the many-body aspect of tunneling. Attractive interactions cause larger depletion. Except for $N = 1$, with $D = 0$, depletion is overall smaller when more atoms are in the system. This is why mean-field simulations so accurately reproduce many-body results.

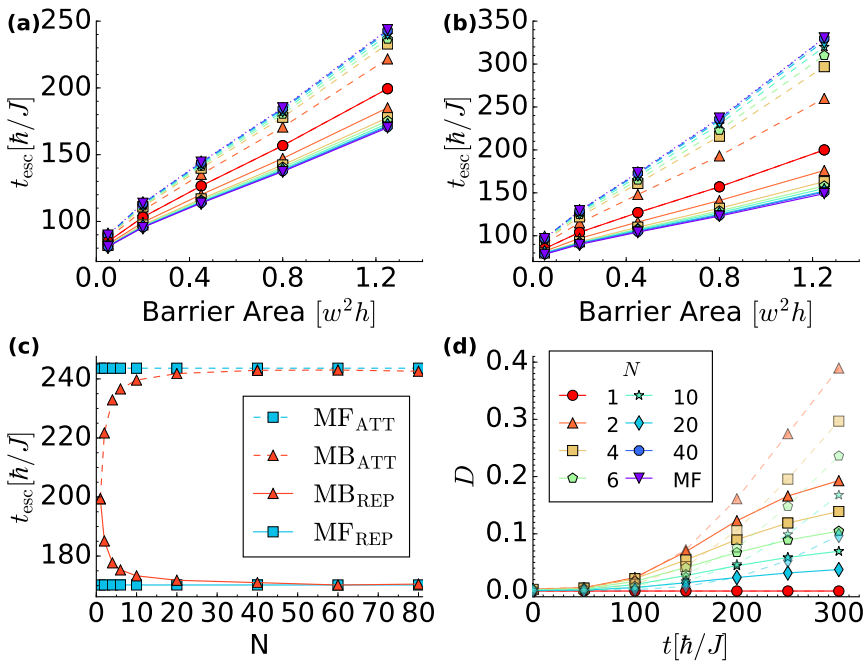

Figure 4.3: *Many-Body (MB) vs. Mean-Field (MF) Escape Time.* Solid lines: Repulsive (REP). Dashed lines: Attractive (ATT). (a)-(b) Dependence of $t_{\rm esc}^{\rm MB}$ on total atom number and barrier area for (a) $NU/J = \pm 0.15$ and (b) $NU/J = \pm 0.30$. (c) $t_{\rm esc}^{\rm MB}$ monotonically approaches $t_{\rm esc}^{\rm MF}$ with increasing N, as shown for $NU/J = \pm 0.15$ and $w = 5$. (d) Depletion for $NU/J = \pm 0.30$ and $w = 5$; attractive markers semi-transparent for readability. Curves are a guide to the eye, points represent actual data with error bars smaller than data point in all panels. Panel (d) legend corresponds to (a),(b), and (d).

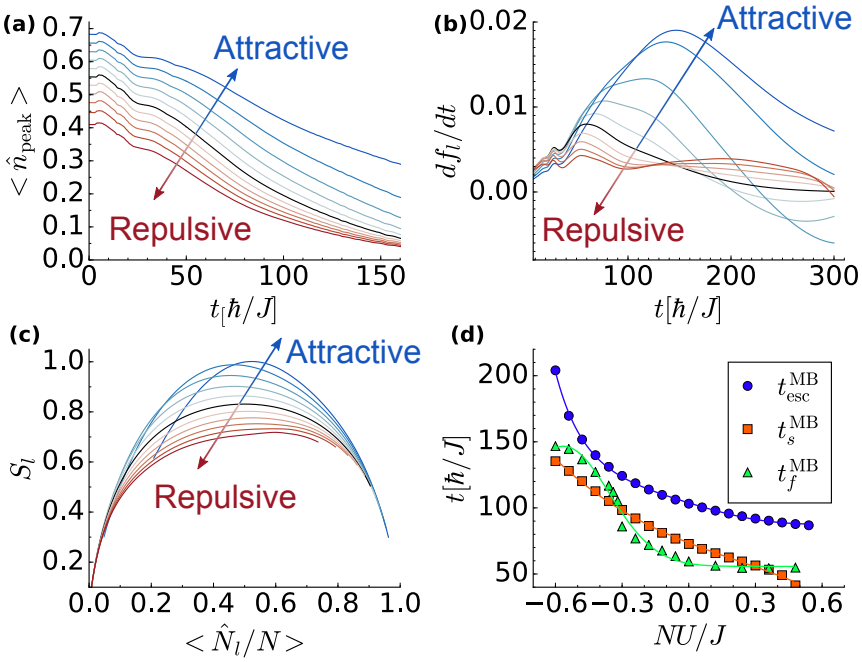

Figure 4.4: *Many-body Quantum Measures.* (a) Average number at the density peak. (b) Time derivative of number fluctuations in the number of trapped atoms are smaller for repulsive interactions (c) Nearly universal curve for the entropy of entanglement vs. the average number of trapped atoms. Black line: No interaction. Darker red/blue corresponds to higher $|NU/J|$. (d) Observables demonstrate very different scaling with interaction. Points show actual data (error bars smaller than points), while lines are best fit curves. All plots treat $N = 6$ with 11 equally spaced values of $NU/J \in [-0.60, 0.60]$.

Figure 4.4(a) plots the largest average on-site number expectation value, $\langle \hat{n}_{\text{peak}} \rangle$, as a function of time. Simply looking at the peak does not allow differentiation between attractive and repulsive dynamics for the first 75 to 100 seconds. The initial flat portion results from information about the barrier drop having to propagate to the peak of the wave function, which is the same for all interactions as the wave-function "recoils" from the non-adiabatic drop of the barrier.

For both attractive and repulsive interactions, the time derivative of fluctuations behind the barrier, df_l/dt, where $i = l$ is the outermost barrier site, have a similar trend for the first 40 seconds Figure 4.4(b). For longer times, weak positive interactions have a negative derivative starting around $t = 200$, while non-interacting and positive interactions approach zero bot remain positive. The rapid tunneling of attractive atoms leaves many open sites in the well, allowing for atoms to maximally delocalize, and thus fluctuations rapidly increase. On the other hand, repulsive interactions energetically favor the localization of a single atom on a single site, leading to a less rapid increase in fluctuations inside the well.

The von Neumann block entropy, $S_l \equiv -\text{Tr}(\hat{\rho}_l \log \hat{\rho}_l)$, with the reduced density matrix for the well plus barrier $\hat{\rho}_l$, measures entanglement between trapped and escaped atoms. In Figure 4.4(c), time $t = 0$ starts at $\langle \hat{N}_l/N \rangle \approx 1$, at the lower-right hand of the curves. As atoms escape, entropy increases, maximizes, and then starts to decrease. The non-interacting system maximizes when half of the atoms have escaped. The largest attractive interaction curve is nearly in the self-trapping regime, where a non-zero number of atoms will remain in the trap at long times.

Given the escape time, $t_{\text{esc}}^{\text{MB}}$, define the times when entanglement entropy, S_l, and the slope of number fluctuations, df_l/dt are largest and less than $t_{\text{esc}}^{\text{MB}}$, respectively, as t_s^{MB} and t_f^{MB}. All three timescales increase as interactions pass from repulsive to attractive interactions Figure 4.4(d). At the endpoints, the strongest interactions, the system approaches self-trapping, $NU/J \to -0.6$, and no meta-stable states, $NU/J \to +0.6$. Scaling in $t_{\text{esc}}^{\text{MB}}$ is approximately exponential for $-0.3 < NU/J < 0.3$, and to fit the stronger interactions a

third order polynomial is required in the exponential. Similarly, scaling for t_f^{MB} is exponential for $-0.3 < NU/J < 0.3$, and requires a second order polynomial in the exponential for the entire interaction range. The entanglement entropy time scale, t_s^{MB}, is quadratic for $-0.4 < NU/J < 0.4$, and cubic polynomial to fit the entire NU/J.

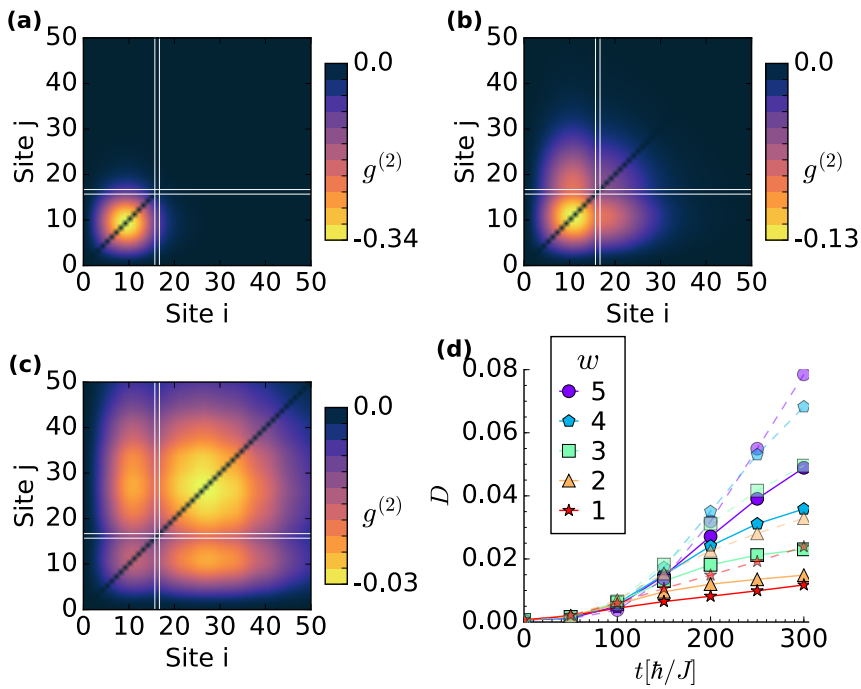

Figure 4.5: *Time-dependence of Density-Density Correlations.* (a)-(c) show $g^{(2)}$ for several time slices, later times indicating correlation between trapped and escaped atoms. The barrier is indicated by white lines; shown are time slices at (a) $t = 0$, (b) $t = 62 \approx t_s$, and (c) $t = 125 \approx t_{\mathrm{esc}}^{\mathrm{MB}}$. (d) Quantum depletion for $N = 2$ with $NU/J = \pm 0.15$. Wider barriers cause larger depletion. Solid lines: repulsive. Dashed semi-transparent lines: attractive. Curves are a guide to the eye, points represent actual data (error bars smaller than points).

Density-density correlations, $g_{ij}^{(2)} = \langle \hat{n}_i \hat{n}_j \rangle - \langle \hat{n}_i \rangle \langle \hat{n}_j \rangle$, or equivalently fluctuation correlations, are a signature of many-body dynamics [55, 110], being zero in a straight-forward mean-field treatment. The diagonal, which measures on-site fluctuations, is set to zero to focus on off-diagonal structure. Correlations are shown in Figure 4.5(a-c) for $N = 40$, $NU/J = -0.015$, and $w = 2$. Initially, at $t = 0$ in Figure 4.5(a), atoms are trapped behind barrier. Near the time when the entropy timescale is largest, Figure 4.5(b), the strongest correlations are inside the well, with the center of correlations moving closer to the barrier,

localized around site 11 to 12. Correlations between trapped and escaped atoms is visible in the upper-left and lower-right regions. By $t \approx 125$, most correlations are in the escaped region, Figure 4.5(c), with a center around site 25 to 27, and correlations have decreased in strength by an order of magnitude. Along with density-density correlations, growing depletion, Figure 4.5(d), indicates the many-body nature of tunneling. Larger barriers and attractive interactions cause larger fragmentation. For any given barrier width, attractive interactions, by $t = 300$, have around double the depletion than the respective repulsive interaction curves. Above $t \approx 200$, attractive interactions still have accelerating depletion, visible from positive concavity, while repulsive interactions have near-zero (for $w = 1$) or negative concavity.

4.3 Efficient Ground-State Creation

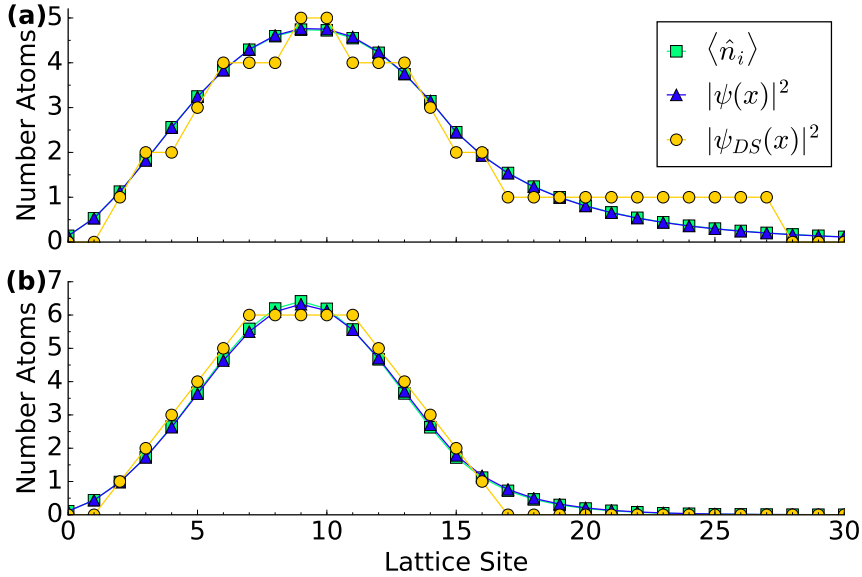

Figure 4.6: *Ground State Wavefunctions.* TEBD $\langle \hat{n}_i \rangle$ (squares), mean-field ground state $|\psi(x)|^2$ (triangles), and digitally-sampled mean-field $|\psi_{DS}(x)|^2$ (circles). (a) Repulsive interaction digital sampling puts more particles in the tail. (b) Attractive interaction digital sampling concentrates particles near peak. Both plots for $N|U|/J = 0.30$ with $N = 60$ particles. Lines are guide to the eye.

Simulating escape-to-free-space can cause difficulty in imaginary time propagation because there are few atoms, up to 80, relative to the lattice size used, over 300, which takes many imaginary time steps to properly spread the atoms into the barrier. We find that two methods alleviate some of this computational difficulty; carefully choosing the trial wave function for imaginary time propagation and beginning with a smaller lattice than required for dynamics.

Because we want to start with a trapped meta-stable state, all calculated many-body ground states are mostly localized behind the barrier, with a tail extending into the barrier. The ground state trial wave function is initialized as a product-state of particles trapped behind the barrier in TEBD. For $N \geq 40$, the initial configuration of the trail wave function is critical; incorrectly chosen trial wave functions fail to converge. We take advantage of the fact that, for $N \geq 40$, $|\psi(x)|^2 \approx \langle\Psi|\,\hat{n}\,|\Psi\rangle$, with $\psi(x)$ calculated from the discrete nonlinear Schrodinger equation, and $|\Psi\rangle$ from the Bose-Hubbard Hamiltonian. To satisfy the product-state form, and closely approximate $|\psi(x)|^2$, we take a digital-sampling of $|\psi(x)|^2$. For attractive (repulsive) interactions we digitally sample to concentrate particles near the wave function peak (tail). Figure 4.6 demonstrates this digital sampling and $|\psi(x)|^2 \approx \langle\Psi|\,\hat{n}\,|\Psi\rangle$.

In order to simulate pseudo-free-space escape, lattices were chosen large enough so that escaping particles never reached the right-wall. However, creating ground-states in large lattices $O(300)$ with many particles ($N \geq 40$) proves to be computationally too expensive in imaginary time, taking many days to converge. We take advantage of numerical precision to circumvent this problem. While running in imaginary time, beyond some given lattice into the barrier, the wave function is numerically zero. For repulsive interactions, the wave function can extend far into the barrier, as far as 250th site, but usually have escape times $t_{\text{esc}} \leq 100$. On the other hand, strong attractive interactions with large N will penetrate up to the 120th site but can have large escape times $t_{\text{esc}} \leq 250$. Although both of these examples, which are the extreme upper limits, would require a lattice $L \approx 350$ for real time simulations, the ground state is found using a smaller lattice. The procedure for finding a

suitable ground-state is as follows:

1. Choose a product-state trial wave function using a mean-field $|\Psi(x)|^2$.

2. Choose an appropriately large lattice size for the particle number and interaction strength.

3. Run imaginary time until ground-state is converged.

4. Check that there are least 5 lattice sites with zero particle occupation at the end of the lattice.

5. If previous step is not satisfied, extend lattice and repeat.

With proper ground-states in hand, it is fairly easy to then extend the lattice sizes for real time propagation. We note that this method of extending states can also be used on the bond-dimension and local-dimension.

4.4 Conclusions

In this chapter, we quantify the quantum tunneling dynamics of a meta-stable state into free space, with superfluid dominated interactions. Many-body dynamics of the Bose-Hubbard Hamiltonian are calculated using matrix product states, which allow for calculation of many-body observables like correlations and entropy. We compare the dynamics to mean-field simulations, using the discrete nonlinear Schrodinger equation. We demonstrate how many-body escape times converged to mean-field times for sufficiently many atoms, for both repulsive and attractive interactions. Repulsive interactions give faster tunneling rates, while attractive interactions slowed down tunneling. We calculate the depletion of the system, with larger number of atoms having lower depletion; this allows mean-field to properly capture many-body dynamics. Number fluctuations in the trap and entanglement entropy, entropy between trapped and escaped atoms, both increased (decreased) for attractive (repulsive) interactions. Entanglement entropy between trapped and escaped atoms maximizes when

half of the atoms have escaped in the non-interacting limit. Attractive interactions resulted in maximization when more than half of the atoms had escaped, while repulsive interactions maximized entropy when fewer than half had escaped. We find drastically different time scaling in different observables. Up to the strongest interactions, time scales for entropy are polynomial, for fluctuations are an exponential with a quadratic in the exponent, and escape times scale as an exponential with a third order polynomial in the exponent. For weaker interactions, these scaling were reduced in the order of the polynomials. Finally, we also quantify correlations throughout the system, showing weak negative correlations between trapped and escaped atoms up to the escape time of the system.

CHAPTER 5

QUANTUM PHASES DRIVE THE DYNAMICS OF MACROSCOPIC QUANTUM TUNNELING ESCAPE IN QUANTUM SIMULATORS

This chapter is from a manuscript which has been submitted to Physical Review X.

Diego A. Alcala, Marie A. McLain, and Lincoln D. Carr

5.1 Abstract

Quantum tunneling remains unexplored in many regimes of many-body quantum physics, including the effect of quantum phase transitions on tunneling dynamics. In general, the quantum phase is a statement about the ground state and has no relation to far-from-equilibrium dynamics. Although tunneling is a highly dynamical process involving many excited states, we find that the quantum phase completely changes the tunneling outcomes. In particular, we consider quasi-bound state dynamics or tunneling escape in the Bose-Hubbard model from a behind a finite barrier, which can be realized in quantum simulators such as ultracold atoms in optical lattices. In the superfluid regime we find that escape dynamics are wave-like and coherent, leading to interference patterns in the density with a non-exponential but still rapid decay process. Quantum entropy production peaks when about half the atoms have escaped. In contrast, in the Mott insulator regime we find the dynamics are atom-like and incoherent, with no interference fringes. Quantum entropy production peaks at double the value of the superfluid case and when only about one quarter of the atoms have escaped. Despite stronger repulsive interactions, tunneling is significantly slowed by the presence of a Mott gap, creating an effective extra barrier to overcome, since only one atom can tunnel at a time, and the decay process is nearly linear, completely defying the standard exponential model. Moreover, we introduce a new quantum tunneling rate, the fluctuation rate, which shows oscillatory interference between the trapped and the

escaped atoms on short time scales beyond the constant waiting time known for single-particle tunneling before exponential decay ensues. The fluctuation rate is overall positive for the superfluid and initially negative for the Mott insulator, only turning positive in the latter case when about half the atoms have escaped. Finally, off-diagonal correlators show entirely different structure for the two quantum phases. In the superfluid case, the barrier height and interaction strength can be used to tune from pulsed to continuous-wave positive correlation emissions in the escape region. In the Mott insulator, negative correlations between the trap and the escape region emphasize emission one atom at a time. Thus the Mott tunneling dynamics are entirely distinct from the superfluid ones and ground state properties of quantum phases can in this case predict highly non-equilibrium behavior.

5.2 Introduction

Quantum phase transitions are the study of abrupt transitions in ground state properties of quantum matter. In particular, a non-analyticity or singularity, typically in a correlator, occurs at zero temperature as a function of some parameter in a governing Hamiltonian. Remarkably, the effects of this singularity emanate into the finite temperature plane as a quantum critical fan [2, 65]. Qualitatively speaking, this effect is like observing the effects of a gravitational singularity, or black hole, from a distance. A major goal of quantum simulators, or analog quantum computing devices, is to discover the phase diagrams of quantum matter, by pinpointing and characterizing quantum phase transitions. However, many quantum simulators, such as ultracold atoms in optical lattices, are in fact much more effective at studying dynamics than statics, and thus a major application of these computing devices is uncovering the principles of far-from-equilibrium dynamics in the many-body quantum context [54]. Such dynamical contexts often deviate very far from the thermal states of the quantum critical fan. To what extent can one relate quantum phase transitions to such dynamics? To date, the principal example of a connection between the ground state phases of quantum matter and dynamics is the Kibble-Zurek mechanism [67], in which the density of defects when ramping through a quantum phase transition is determined by the critical

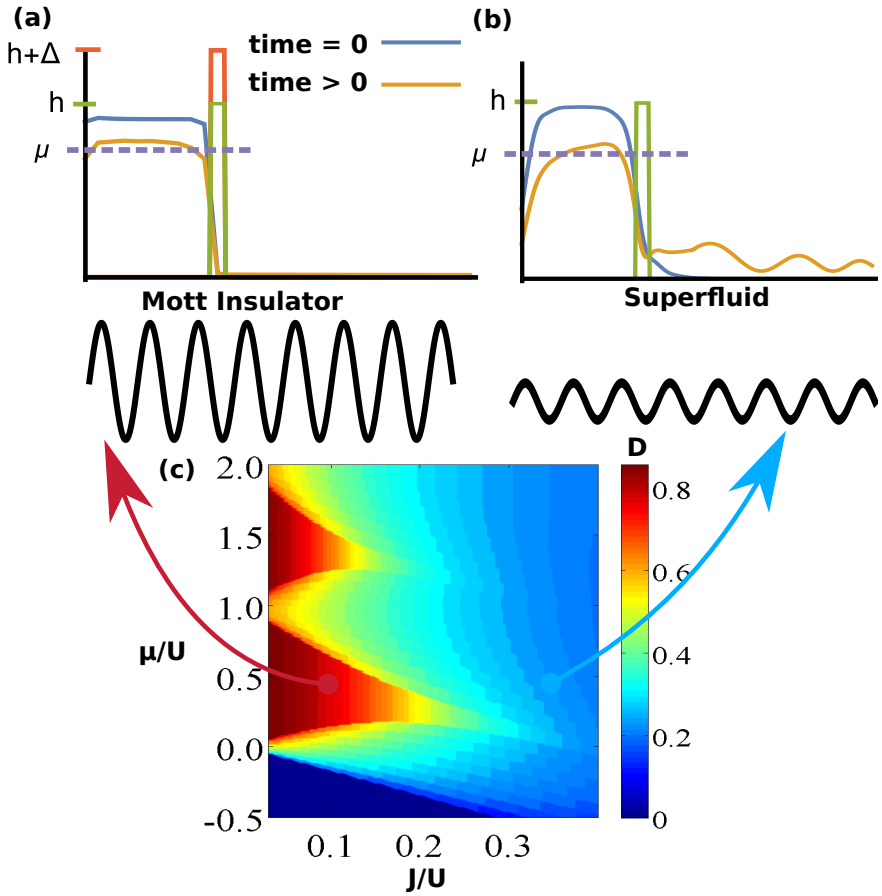

Figure 5.1: *Sketch of effects of the quantum phase on macroscopic quantum tunneling* (Upper left): The Mott insulator phase slows down tunneling due to the presence of the Mott gap over and above the effective barrier height of $h-\mu$, preventing more than one atom from escaping at a time. (Upper right): The superfluid undergoes more rapid tunneling with characteristic wave-like interference fringes in the escape region. (Lower panel): The mesoscopic quantum phase diagram shows the quantum depletion, or portion of the atoms outside one macroscopic semi-classical mode, as a function of chemical potential μ vs. lattice hopping energy J, both scaled to interaction energy U. The quantum phases occupy well-defined Mott insulating lobes (left, red region) and a superfluid continuum (right, blue region), even for just $N = 10$ atoms, as shown here (adapted from [66]).

exponents of the quantum phase and the ramp rate. In this Article, we discover and present a new example of the quantum phase determining dynamical outcomes far from equilibrium, namely, macroscopic quantum tunneling.

Although quantum tunneling is a well-known phenomenon in single-particle quantum physics, beginning with Gamow's 1928 [111], and then Gurney and Condon's [112] independent 1929 explanation of radioactive decay, both theoretical predictions and experimental demonstrations in many-body quantum physics have yet to be discovered in most regimes [13]. However, there have been a few cases of new tunneling regimes uncovered in quantum simulators. These are dominated by either nonlinearity, a classical wave effect and very much in the semiclassical limit, or by bosonic or fermionic statistics. Examples include observation of the tunneling to nonlinear self-trapping transition of a Bose-Einstein condensate (BEC) in a double well potential [25]; controlled tunneling escape of fermions via pairing and quantum statistics [16]; and interaction-assisted escape of a BEC and emergence of a non-exponential escape rate [84]. In all of these cases the interactions inherent in the quantum matter, whether bosonic or fermionic, significantly modify the tunneling dynamics. However, correlations beyond Fermi/Bose statistics and entanglement have not yet played a role. Thus the study of macroscopic or many-body quantum tunneling has to-date mainly been constrained to those features we primarily associate with developments in physics before the era of quantum information science and tunable quantum computational devices. By incorporating quantum phase transitions into macroscopic quantum tunneling, we take tunneling into a new regime in this Article.

A surprising fact about quantum phase transitions is that despite the Mermin-Wagner-Hohenbeg theorem demonstrating lack of a limit to a perfect non-analyticity in one dimension, nevertheless 1D systems such as quasi-1D BECs [113] effectively demonstrate phase transitions [114]. The decay of correlations in a given phase may change form, e.g. from exponential to algebraic, but transitions at the critical point remain sharp. In particular, in the Bose-Hubbard Hamiltonian (BHH), the most common model realized in cold atom

quantum simulators, it takes only 5-10 sites before the quantum phase diagram begins to emerge [66]. In nuclear physics the study of such mesoscopic phase transitions is key due to the relatively small number of nucleons in a given nucleus, e.g. in nuclear shape transitions [115]. It is thus possible to create a finite-sized region of quantum matter in a quantum simulator set behind a barrier and observe the many-body quantum generalization of the original notion of tunneling, the quasi-bound or tunneling escape problem. As we will show, the quantum phase then determines the tunneling outcome. Quantum simulators in which such experiments can be performed cover a wide range of architectures [54] in the quasi-1D context, including superconducting Josephson-Junction based circuits and Rydberg chains, as all these systems can create mesoscopic quantum phases.

We focus here on cold atoms in optical lattices. The 1D BHH has both a mean-field U(1) second order quantum phase transition and a Berzinskii-Kosterlitz-Thouless (BKT) or continuous quantum phase transition. In Figure 5.1(c) we show how such transitions appear for a mesoscopic system. In Figure 5.1(a)-(b) we show how the tunneling outcome is radically different between the wave-like, coherent, more semiclassical superfluid phase, and the atom-like, incoherent, interaction-induced Mott insulator phase. As we will show, there are many other distinguishing features in the dynamical many-body quantum outcomes as observed in number fluctuations, entanglement, and two-point correlators. For example, the Mott gap in the Mott insulator presents an extra barrier to overcome, leading to a surprising slowdown in quantum tunneling despite the stronger repulsive interactions in this quantum phase that would otherwise push the atoms more rapidly through the barrier. Yet the peak of entanglement occurs much earlier, when only one quarter of the atoms have tunneled through as compared to one half for the superfluid phase.

This Article is outlined as follows. In Section 5.3, we show how the quantum phases of the BHH, although slightly modified by the presence of the barrier, remain intact. In Section 5.7, we present the results of our matrix-product-state simulations [116] on macroscopic quantum tunneling escape of a meta-stable state into free space, calculating single-body

observables like the number of atoms remaining in the trap, where we find distinct patterns of wave-like and atom-like tunneling for the superfluid and Mott-insulator interaction regimes, respectively. In Sec 5.8 we go beyond such traditional measures derived from the single-particle quantum tunneling picture, demonstrating that number fluctuations and von Neumann quantum entropy both show significant differences in the two quantum phases, and introducing a new quantity to characterize macroscopic quantum tunneling, the *fluctuation rate*. Finally, in Sec. 5.11 we show how extremely different the tunneling dynamics of correlations is in each case, highlighting that it is positive and negative correlations that ultimately explain the difference in tunneling outcomes. Our findings and conclusions are summarized in Section 5.14.

5.3 Tunneling Initialization

In the following we describe the Bose-Hubbard Hamiltonian. We describe the effects of mesoscopic confinement on the usual notion of the quantum phase. Then we show that for sufficiently high barriers, scaled to interaction strength, the initial quantum state is well-confined and has a superfluid or Mott-insulating character on either side of the quantum critical point. This sets up the problem for the study of tunneling dynamics in Sec. 5.7.

5.4 The Bose-Hubbard Hamiltonian

The BHH models cold bosonic atoms in optical lattices in the tight-binding and lowest-band approximation, which is valid for typical atomic interaction strengths and a lattice potential energy several times the recoil energy or greater [117]. For weak interactions the BHH can alternately be considered as a discretization of the continuum field theory in the deep superfluid regime for long wavelength properties. However, for strong interactions the BHH undergoes a superfluid to Mott insulator quantum phase transition at a critical point $(J/U)_c = 0.305$, where the BHH takes the form

$$\hat{H} = -J \sum_{i=1}^{L-1} (\hat{b}_i^\dagger \hat{b}_{i+1} + \text{h.c.}) + \sum_{i=1}^{L} [\frac{U}{2} \hat{n}_i (\hat{n}_i - \hat{1}) + V_i^{\text{ext}} \hat{n}_i]. \tag{5.1}$$

The coefficients J and U are the hopping and on-site interaction energies, respectively. Hopping is often called "tunneling" but refers to a single-particle effect in which occupation of one lattice site tunnels to the next via an overlap integral between the site-local wavefunctions. Here, we study in contrast *macroscopic* quantum tunneling, referring to the collective tunneling of many atoms. In order to study the macroscopic quantum escape problem, which can also be viewed as decay of a many-body quasi-bound state, we include an external, site-dependent, potential barrier as V_i^{ext}, where $i \in [1, L]$, and the total lattice size is L. Such a barrier can be realized e.g. by a tightly focused Gaussian beam on top of the lattice [84]. For the remainder of our study we work in hopping units, scaling all energies to the hopping energy, J, and time to $\hbar/J$. For simplicity, we choose a square barrier of form $V_i^{\text{ext}} = h$ for $a < i < b$ with a the well width and $w = b - a$ the barrier width, and 0 otherwise. Our BHH is stated in terms of finite atom number N, and therefore does not include a chemical potential term. However, for the sketch in Figure 5.1, μ may be taken as

$$\mu(N) = \partial E/\partial N \simeq E(N+1) - E(N), \tag{5.2}$$

where $E = \langle \hat{H} \rangle$ with respect to the ground state or quantum phase. The BKT phase transition occurs at the tip of the Mott lobe for commensurate filling, i.e. $N = L_{\text{trap}}$, while the $U(1)$ mean field transition occurs as one transitions vertically through the phase diagram. In our case, the latter translates into a noncommensurate filling created by subtracting atoms, as naturally occurs in the quantum escape process.

Our main solution method is matrix-product state (MPS) simulation, in particular time-evolving block decimation (TEBD) in our openMPS codes under imaginary time relaxation to obtain the initial state, and real-time propagation to determine tunneling dynamics. Our usage of these open-source codes and convergence criteria are detailed thoroughly in [116] and have been established in prior works on the semiclassical limit to tunneling in [36] and [13]. In summary, we converge in Schmidt truncation error, or error due to only a finite number of elements retained in the reduced density matrix after a partial trace, and local dimension, allowing sufficient number fluctuations on-site. These simulations are time-

adaptive, as standard for MPS methods. Local dimension is converged from 4 to up to 8 atoms per site ($d = 5$ to $d = 9$ including the vacuum state of zero atoms on-site), while entanglement is converged with a Schmidt number of from $\chi = 60$ to $\chi = 200$. In previous work much lower χ was required as superfluids are not highly entangled, but to capture Mott dynamics we needed to consider higher χ in this work. All results are converged to much better than visible to the eye, and sufficient for the conclusions of this Article. In particular, all curves and surfaces shown in figures have a maximal relative error of 10^{-2} at the longest times of $t = 300$ to 500 for the highest interaction strengths, where relative error is taken as $\varepsilon = |(f_1 - f_2)/[2(f_1 + f_2)]$ with f_1 and f_2 observables of increasing χ, local dimension d, etc. Within the key part of the dynamics at $t = 0$ to $t = 150$ we maintain a convergence of $\varepsilon \leq 10^{-4}$ in all observables.

5.5 Mesoscopic Quantum Matter

We first examine the effect of the barrier on the ground-state parameter space for both commensurate and non-commensurate cases. Our initial meta-stable state, localized inside the well of size $a = L_{\text{trap}} \lesssim N$, will be close to a commensurate filling, with a few atoms penetrating into the barrier, Figure 5.1. Under time evolution, this state will tunnel into a near-continuum escape region of an extended lattice, where the number of lattice sites far exceeds the number of escaping atoms. The motivations behind this initial study are twofold. First, we need to understand how the penetration of the tail of the many-body wavefunction into the barrier will affect the Mott-to-Superfluid transition shown in Figure 5.1. Second, the statics will help clarify which values of U and h to use in tandem. For example, if the barrier h is too high, then the wave function will tunnel too slowly to be observed within a reasonable time scale for our simulations and for experiments, resulting in self-trapping, as observed also for the double well [25]. If h is too low, the repulsive interactions in the trap will overcome the barrier, the many-body wavefunction will spill classically over the top of the barrier, and no meta-stable states will exist.

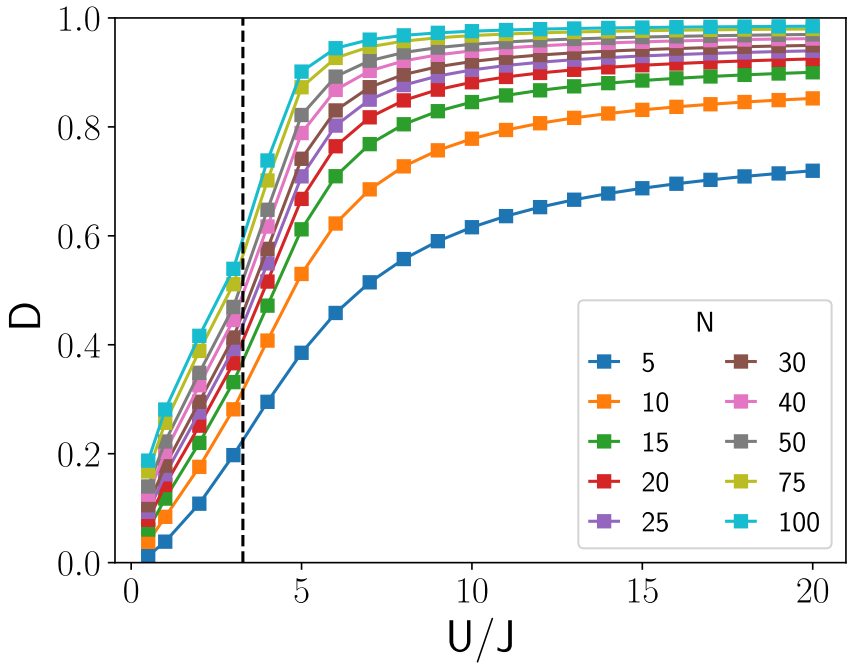

Figure 5.2: *Finite size crossover in quantum depletion through the quantum phase transition.* Quantum depletion measures the fraction of atoms not in the dominant semiclassical mode in the superfluid or Bose-Einstein condensate (BEC) regime [117]. Shown are $N = 5$ to 100 atoms with commensurate filling $L = N$, as a function of U/J. As N increases, the quantum depletion approaches an infinite system size limit. High levels of quantum depletion approaching and beyond the quantum critical point at $(U/J)_c = 1/0.305 = 3.28$ [64] (black dashed vertical line) indicate semiclassical methods such as the JWKB and path integral approximations will fail [118], necessitating our MPS approach to capture strong correlations.

We first consider a small uniform finite-size system, that is, the well only, without the barrier. Figure 5.2 shows how quantum depletion, D, trends towards the infinite size limit for increasing U/J and N, where

$$D = 1 - \frac{\lambda_1}{\sum_{m=1}^{L} \lambda_m}, \tag{5.3}$$

with the eigenvalues, λ_m, determined from the single-particle density matrix, $\langle \hat{b}_i^\dagger \hat{b}_j \rangle$, and λ_1 the largest eigenvalue. Because a many-body treatment of our meta-stable state neccessarily has a finite number of atoms, Figure 5.2 roughly outlines how "Mott-like" or "superfluid-like" a finite commensurate filled system will behave. The true BKT phase transition occurs at $(U/J)_c \approx 3.28$ [64]. Even for just 5 or 10 sites, the quantum depletion rises rapidly as the theoretical quantum critical point from the infinite size extrapolation is crossed. The quantum critical point for finite-size systems is often taken as the point of inflection in this curve [66]; however, for simplicity, it suffices to refer to the theoretical infinite size limit for the rest of our paper, as we will test values of U/J well to the left and right of the vertical line shown in Figure 5.2.

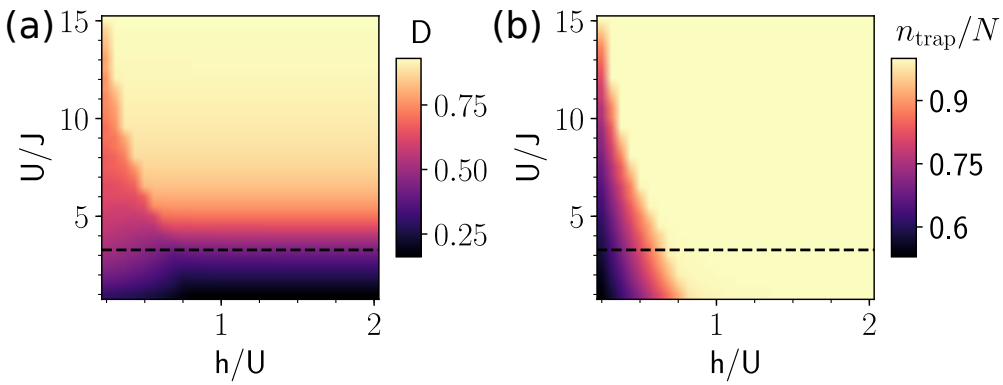

Figure 5.3: *Effect of the barrier on the quantum phase transition.* (a) Quantum depletion and (b) number of trapped atoms as a function of interaction strength U/J and barrier height h/U. The critical point for the quantum phase transition is indicated with a dashed black line. In the Mott regime the depletion is only decreased by sufficiently small barriers $h/U \lesssim 0.5$, indicating the quantum phase is maintained. Likewise, interactions, although repulsive, prevent penetration into the barrier.

5.6 Effects of the Barrier on the Quantum Phase

Next, we consider the effects of the finite barrier, Figure 5.3. In this Article, we study escape dynamics from a confinement area of size L_{trap} behind a narrow barrier into a quasi-continuum escape region, i.e., in systems with $L >> N$. Previous research, analyzing double-well dynamics, looked at highly discrete systems with $L \sim 2N$. In fact, a frequent approximation is the two-mode approximation or Lipkin-Meshkov-Glick model [119], which assumes just one discrete state on each side of the barrier [25, 120]. The much larger lattice in this Article alters the ground state regimes, introducing restrictions to achieve sufficient containment in the trap. To allow observation of meta-stable quantum tunneling into a quasi-continuous free space, we require a barrier that is balanced between being large enough to trap the atoms, and sufficiently small to allow for tunneling rates on a reasonable time scale. Furthermore, the interaction strength, U/J, must span superfluid- and Mott-dominated regimes.

To explore such questions, we first determine the ground state with TEBD for an initial very wide barrier beginning at $i = a$ and ending at $i = b = L$, i.e., covering the whole escape region. This is the initial state, explored in Figure 5.2. Dynamics begins in Figure 5.4 when we abruptly reduce b to $a + w \ll L$, where w is the barrier width, with the remaining escape region from b to L a quasi-continuum. For dynamics, we often take $L = 500$ or more to avoid reflections in the escape region over the time scale of the simulation.

To illustrate maintenance of the quantum phase and penetration of the wavefunction into the barrier in Figure 5.2, we chose $N = 25$, $a = 25$, and $b = L = 100$ for illustration purposes. The quantum depletion D and average scaled number of trapped atoms $n_{\text{trap}}/N \langle \hat{n}_{\text{trap}} \rangle /N$ both show a clear boundary as a function of interaction strength U/J and barrier height h/U. We choose to scale barrier height to U rather than J because in a semiclassical picture the effective barrier height for tunneling [13] is $h - \mu \simeq h - U * 1$, since $\mu \simeq U * n_{\text{trap}}/L_{\text{trap}} \simeq U * 1$. Although a semiclassical picture proves insufficient for the Mott regime in particular, this is a good starting point as a baseline. As long as the barrier is not too low with respect to the interaction strength, Figure 5.2(a) shows that the quantum phase is well maintained, while

Figure 5.2(b) show the initial penetration of the wavefunction into the barrier is small.

We explored from $N = 100$ to $N = 5$, and these effects persist for $N = L_{\text{trap}} = a$ throughout this regime, although with slightly less sharp boundaries in Figure 5.2 for smaller N. These results are consistent with the mesoscopic quantum phase transition conclusions in [66], and show the presence of the boundary, as long as not too low, maintains the quantum phase even for small regions of quantum matter.

5.7 Coherent Superfluid vs. Incoherent Mott Tunneling Dynamics

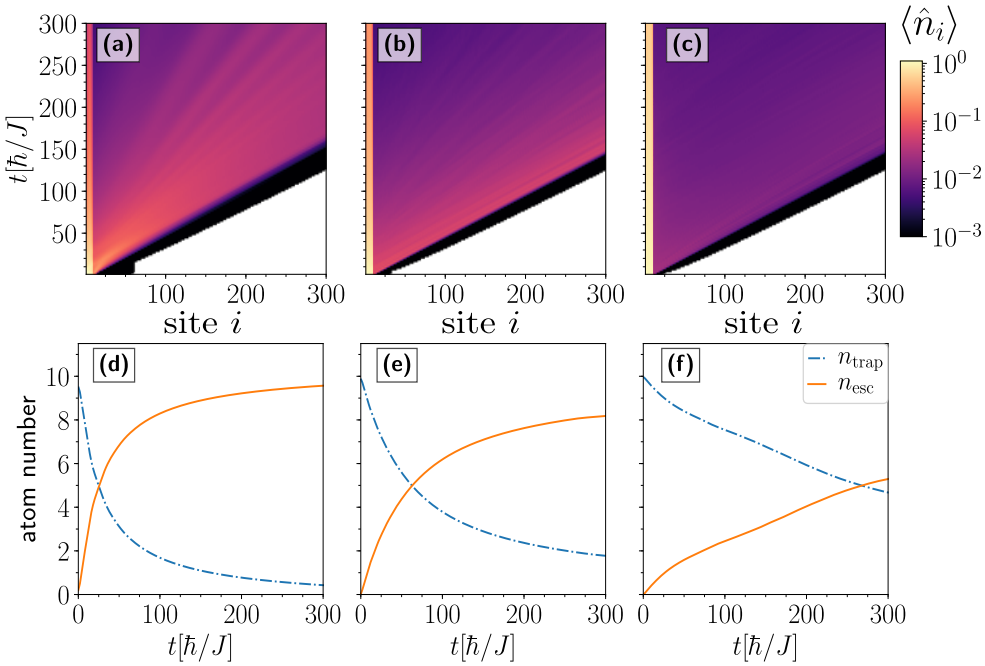

Figure 5.4: *Wave-like vs. atom-like quantum tunneling escape dynamics.* (a)-(c) Space-time evolution of average on-site occupation number $\langle \hat{n}_i \rangle$. (d)-(f) Evolution of total atom number in the trap, $\langle \hat{n}_{\text{trap}} \rangle$ and in the escape region, $\langle \hat{n}_{\text{esc}} \rangle$. Interactions increase from left to right: (a,d) weakly interacting superfluid regime, $U = 1.0$; (b,e) critical regime, $U = 3.0$; and (c,f) strongly interacting Mott insulator regime, $U = 6.0$; all with $N = 10$ and $h/U = 1.0$. Weaker interactions show strong wave-like interference patterns, as one expects for a superfluid. The Mott-insulator, despite being a ground state property, persists in the lack of interference in the incoherent escape dynamics, generating a much more atom-like behavior, albeit with a much slower rate influenced by the Mott gap. The Mott gap creates an effective additional barrier to overcome, as one can observe in the slower decrease of atoms remaining in the trap in (f).

After initializing the quasi-bound state as described in Sec. 5.6 via imaginary time propagation with TEBD, we drop the barrier except for a narrow delta-function-like remnant, creating a thin barrier through which the many-body quantum wavefunction can tunnel through on experimental timescales. The rationale for such a thin barrier is key to making experiments work, and is detailed experimentally in [84] and theoretically in [13, 121]. Thus the new barrier in Eq. 5.1 takes the form $V_i = h\delta_{i,N}$, where $\delta_{i,N}$ is the Kronecker delta set so that the filling factor, or average occupation per site, is initially very close to 1, or commensurate.

Thus, at the start of the dynamics, $t = 0$, the wave function is in a meta-stable state, able to escape into a quasi-continuum escape region. The hard wall at the end of lattice, at $i = L$, is taken sufficiently far that any reflected atoms do not interfere with the dynamics near the barrier, and typically chosen at $L = 300$ to 500. We proceed to propagate in real time with TEBD. Figure 5.4(a-c) shows a space-time heatmap of the average on-site atom number, $\langle \hat{n}_i \rangle$, with time along the vertical axis and lattice site along the horizontal axis. From left to right are shown increasing interaction strength from an initial weakly-interacting superfluid ($U/J = 1.0$ to a near-critical system $U/J = 3.0$ to an initial strongly-interacting Mott insulator ($U/J = 6.0$). For the initial superfluid state, during the first 50 time steps in Figure 5.4(a), the escaped wave function stays together, before fanning out into an interference-like pattern, with each anti-node covering upwards of 10 lattice sites, starting around $t \approx 90$ and sites $i \geq 50$. These patterns have been called "blips" in semiclassical studies [122]. Such blips appear for both attractive and repulsive interactions, and even in the non-interacting or single-particle case, and are therefore due to interference phenomena obtainable with the Feynman propagator [123]. In contrast, for initial critical and strongly-interacting regimes, Figure 5.4(b-c), the wave-like interference phenomena disappear. Instead, there are only weakly distinguishable and narrow streaks, immediately after the atoms start escaping. Each streak is very narrow, and does not show a regular interference pattern. Note that in all regimes the black line is a result of the well-known

Lieb-Robinson bound [124] or "quantum speed limit" for Eq. (5.1).

The bottom row of Figure 5.4 shows the number of atoms remaining in the trap, n_{trap} and the number that have escaped into the quasi-continuum, n_{esc}. The number of atoms under the narrow barrier is always much less than 1, and is not shown. For the superfluid regime it was previously demonstrated [13, 36] that stronger repulsive interactions, U, in general cause faster escape for a given barrier height, $h \equiv$ const.. This is because in the semiclassical limit repulsive interactions lead to an effective nonlinear term which push the tail into the barrier. The dependence of rate on interaction strength as a function of n_{trap} is somewhat subtle, and in fact the rate very slightly decreases in a small region near the point of spilling classically over the barrier due to deformation of the barrier by the mean field or nonlinearity [121].

However, consideration of the critical to strongly-interacting regime and solution with a fully entangled dynamical method as we perform here with TEBD shows a massive decrease in the tunneling rate, as observed in the bottom row of Figure 5.4. A key feature of the Mott insulator is the Mott gap, $\Delta = 2U$. This is the energetic barrier required to move one atom by one site, as evident in Eq. (5.1) for $U \gg J$. In order for tunneling to occur in a Mott insulator atoms have to hop one site at a time, rather than all together and collectively as in the superfluid limit, and thus the Mott gap must be overcome. Especially early in the tunneling process where the initial state has a Mott gap due to initial commensurate filling, here of 10 atoms on 10 sites, the Mott gap thus presents an additional barrier that must be overcome, decreasing the tunneling rate significantly. This effect is sketched in Figure 5.1 qualitatively and born out here in dynamical simulations. We observe the same kinds of slow-down effect for 25 atoms on 25 sites in critical and strongly interacting regimes (simulations not shown).

Loosely speaking, we may quantify this transition from superfluid to Mott-insulating regimes as wave-like to atom-like. In the wave-like limit a semiclassical theory provides guidance, and we see a clear and regular pattern of interference fringes. In the atom-like

limit tunneling is dominated by atom-like hops influenced by the Mott gap. We remind the reader that Mott insulator refers to the resistance of the quantum state to atom flow, or current. Escaping through the barrier is analogous to water flowing through a break in a dam, or current through a weak point in a barrier as in a Josephson Junction. The superfluid flows in the Josephson regime. Placing a Mott insulator behind the barrier greatly reduces the ability of the atoms to rapidly flow.

We already know that the decay curve of n_{trap} is non-exponential [13, 84] even in the weakly interacting superfluid regime. This is interpreted as being due to the single-particle energy (equivalent to a chemical potential) dropping relative to the barrier height. However, here we see that for the Mott insulator the distortion from the well-known single-particle exponential form is much more extreme. To examine this question more closely, in Figure 5.5(a)-(b) we show the dependence of n_{trap} on both the barrier height h/U and the interaction strength U/J. As we described in Sec. 5.3, the barrier height is scaled with interaction to keep the effective barrier height at the same level, as the effective chemical potential in Eq. (5.2) scales with U and sets the single-particle tunneling energy in the presence of the trapped many-body wavefunction. Although the slow-down in the rate for stronger interactions is easily apparent, the time-dependent rate $\Gamma(t) = dn_{\text{trap}}/dt$ clarifies the extreme difference in the non-exponential behavior beyond wave-like or atom-like classifications. For single-particle quantum tunneling the rate equation takes the form $dn/dt = -\Gamma n$, with Γ constant. Here, whether plotted for $\Gamma(t)$ in Figure 5.5(c)-(d) or $\Gamma(n_{\text{trap}})$ in Figure 5.5(e)-(f), Γ is very clearly non-constant and therefore non-exponential. The rates are calculated from numerical derivatives on our data in Figure 5.5(a)-(b) using Python's SciPy interpolating function.

For weak interactions at $U = 1.0$ the wave-like interference effects are apparent in oscillations in the rates, and the rates are initially rapid, then slow down. However, at the critical point of $U = 3.0$ and beyond into the strongly interacting Mott insulator regime of $U = 6.0$, the rates are an order of magnitude smaller. They at first increase rapidly on a

very short time scale, then decrease linearly as a function of time. In the case of $\Gamma(n_{\text{trap}})$ one can see very small oscillations in the rate corresponding to the faint streaks seen in Figure 5.4(c). The narrow width of these indicates single atom effects. The Mott gap prevents more than one atom leaving the system at a time, or indeed any kind of collective escape, as for two atoms to act together they must overcome the Mott gap of $2U$ over and above the trap barrier. Lower barriers (left column of Figure 5.5) allow wave-like interference effects to persist to higher interaction strengths as compared to higher barriers (right column of Figure 5.5). This is due to higher barriers creating a more commensurate initial state with strong confinement, as also observed in Figure 5.2.

5.8 Number Fluctuations, Entropy, and a New Rate to Characterize Macroscopic Quantum Tunneling

So far we have looked at how the typical observables from the single-particle quantum tunneling escape problem are modified by interactions and an initial quantum phase. We observed wave-like and atom-like dynamical in the space-time dependence of the number density and a highly non-exponential decay rate. However, in many-body quantum systems we can also measure new quantities which provide new information not relevant to a single-particle picture.

In the primarily mean field or semi-classical picture of macroscopic quantum tunneling explored in many weakly-interacting or statistically driven scenarios prior to this Article [25, 84], number fluctuations were necessarily zero, as the mean field approximation neglects these. An outstanding question has thus been how number fluctuations affect tunneling dynamics, over and above the semiclassical limit. Here we can track their evolution explicitly with TEBD, and determine a new quantum tunneling rate, the *fluctuation rate*, which clearly demarcates the boundary between superfluid and Mott insulating phases.

An understanding of number fluctuations is also important because bipartite entanglement measures like the bond entropy between the trapped and escaped atoms have been shown to be driven by local fluctuations in a globally conserved quantity [125]. Since total

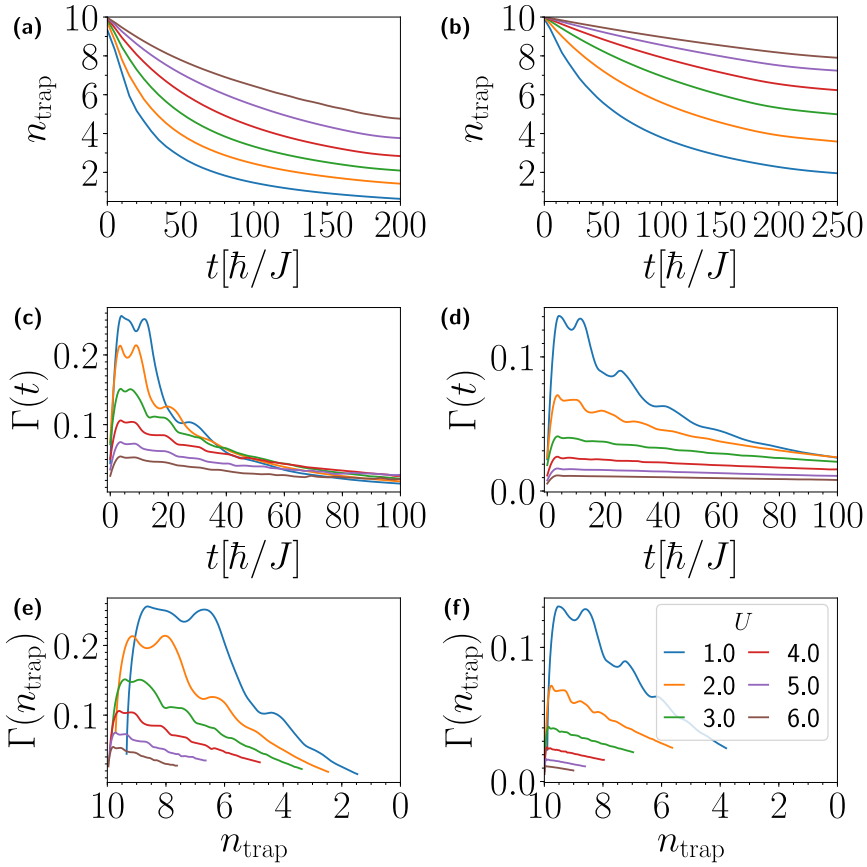

Figure 5.5: *Non-exponential tunneling rates from superfluid to Mott-insulating regimes.* (a)-(b) Number of trapped atoms n_{trap} for increasing interaction strengths from weakly interacting to critical to strongly interacting regimes show a rapid slow-down in tunneling, in contrast to semiclassical predictions. (c)-(d) Time-dependent tunneling rates $\Gamma(t)$ and (e)-(f) number-dependent tunneling rates $\Gamma(n_{\mathrm{trap}})$ show a highly non-exponential behavior, with wave-like interference phenomena for weak interactions and an order-of magnitude difference in rates as a function of interactions. The low barrier case of $h/U = 0.9$ (left column) shows more persistent wave-like interference patterns as compared to the high barrier case of $h/U = 2.0$ due to weaker and therefore less commensurate confinement of the initial state. The initial Mott insulator is affected more by the Mott gap when more strongly initially confined.

atom number is conserved in our TEBD simulations, we can consider first number fluctuations in 5.9, then explore the generated quantum entropy in Sec. 5.10.

5.9 Number Fluctuations

Number fluctuations can be defined on a single site as

$$\Delta(n_i)^2 \equiv \langle \Delta(\hat{n}_i)^2 \rangle = \langle \hat{n}_i^2 \rangle - \langle \hat{n}_i \rangle^2 \tag{5.4}$$

or between trap and escaped region as

$$\Delta(n_{\text{trap}})^2 \equiv \langle \Delta(\hat{n}_{\text{trap}})^2 \rangle = \langle \hat{n}_{\text{trap}}^2 \rangle - \langle \hat{n}_{\text{trap}} \rangle^2 \tag{5.5}$$

with $\hat{n}_{\text{trap}} = \sum_{i=1}^{\ell} \hat{n}_i$ the sum over number operators for all atoms remaining in the trap.

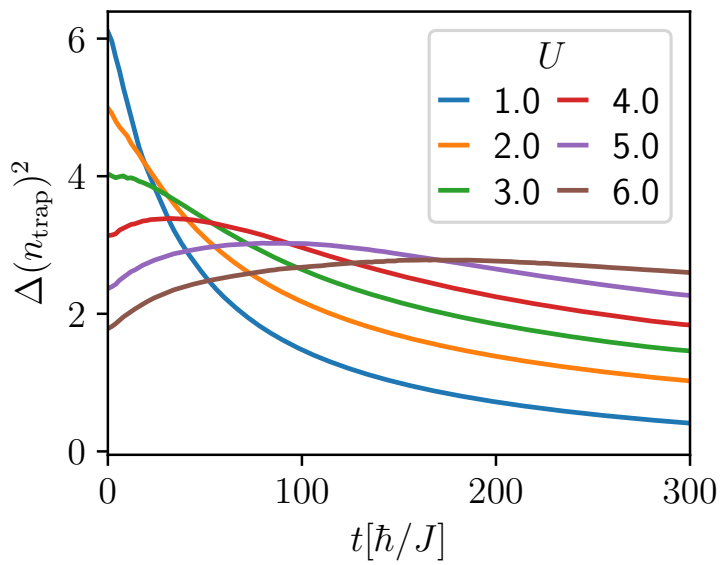

Figure 5.6: *Time evolution of number fluctuations in trap.* Many previous models of macroscopic quantum tunneling focused on the semiclassical or mean field limit in which number fluctuations are assumed to be zero. Here we show that they depend strongly on the initial quantum phase, with a monotonic decrease in the weakly interacting superfluid regime and a non-monotonic increase followed by a decrease in the Mott insulating regime. The transition occurs around the critical point.

In Figure 5.6 is shown the time evolution of the number fluctuations in the trap for a barrier of height $h/U = 1.0$. Number fluctuations start at 6, or $6/10 = 60\%$, for $U/J = 1.0$. They then rapidly decrease to zero in the superfluid regime as the tunneling proceeds. As

repulsive interactions increase, the starting level of number fluctuations is lower, and the decrease is slower, but the behavior is still monotonic. However, starting in the critical region at $U/J = 3.0$, the time evolution changes character, turning from concave to convex, and for stronger interactions into the Mott insulating regime the number fluctuations become non-monotonic. They at first rise, then decay slowly, with a time scale that grows as the interactions are made stronger.

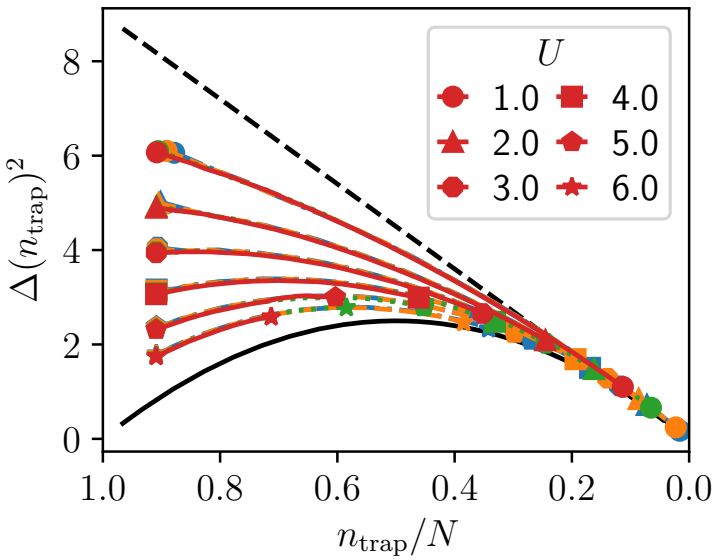

Figure 5.7: *Number fluctuations as a function of the remaining trapped atoms.* Number fluctuations dynamics depend principally in interaction strength U/J ($U = 1$ to $U = 6$, symbols in key). Different barrier heights of $h/U = 0.9, 1.0, 1.5, 2.0$ (blue, orange, green, and red) collapse onto nearly the same curves. The extreme $U/J = 0$ and $U/J = \infty$ limits are shown as dashed black and solid black curves, respectively, clarifying the emergence of non-monotonicity in the time evolution in Figure 5.6.

To help interpret this distinct non-monotonicity of the number fluctuations in the Mott insulating phase in Figure 5.7 we plot the number fluctuations as a function of the number of remaining atoms in the trap, normalized to the total atom number N. The dashed curve shows the extreme case of $U/J \to 0$, while the solid curve shows the case of $U/J \to \infty$ – both can be calculated straightforwardly from perturbation theory. In the $U/J \to \infty$ limit, the number fluctuations start at zero because the system is in a Fock state of one atom per

site. As the tunneling proceeds, one particle at a time passes through the barrier, increasing number fluctuations as more holes appear in the system, since atoms can hop both left and right. When half the atoms have left the trap, fluctuations are maximal, and then decrease as the number of arrangements of n_{trap} atoms on ℓ sites decreases.

In Figure 5.7, we observe that it is at the critical point where the transition between monotonic and non-monotonic behavior occurs. In Figure 5.6 we showed only the barrier heigh $h/U = 1.0$; here we show that all barrier heights nearly collapse onto the same curves, and that number fluctuations depend mainly on interaction strength.

Although the evolution of the number fluctuations appears smooth, in fact on shorter time scales it is oscillatory. Early time evolution of even single-particle quantum tunneling is known to be non-exponential [126], due to a waiting period for tunneling to begin, that is, the exponential decay of single-particle tunneling does not turn on instantaneously. In Sec. 5.7 we demonstrated non-constant rates in the average number over and above single-particle expectations. To complete our study of number fluctuation dynamics, we consider the rate of change of number fluctuations,

$$\Gamma^{\text{fluct}}(t) \equiv -\frac{d}{dt}[\Delta(n_{\text{trap}})^2]. \tag{5.6}$$

In Figure 5.8 we show that initial oscillations in the number fluctuations occur mainly from $t = 0$ to $t = 20$. For a trap of size $L_{\text{trap}} = 10$, this is the time for excitations at the barrier edge to reflect back through the trap and interfere in the escape process. Such oscillations are much weaker for the Mott insulator as they must flow over the top in a superfluid "skin" as seen also in the well-known wedding cake structure in trapped BHH systems [127]. Once these trapped oscillations created by the initial state escape, the rate is positive and rapidly decreases for the superfluid. However, the Mott insulator has an initial negative fluctuation rate, which only later becomes positive. The critical point determines where the fluctuation rate passes from positive to negative as interactions are increased.

We emphasize the number fluctuations can be determined experimentally in BECs and cold atoms in optical lattices by subtracting the ensemble average of many density measure-

ments from each individual density measurement. The ensemble over the resulting images is related to the average fluctuations [54], from which the average fluctuation rate can be determined.

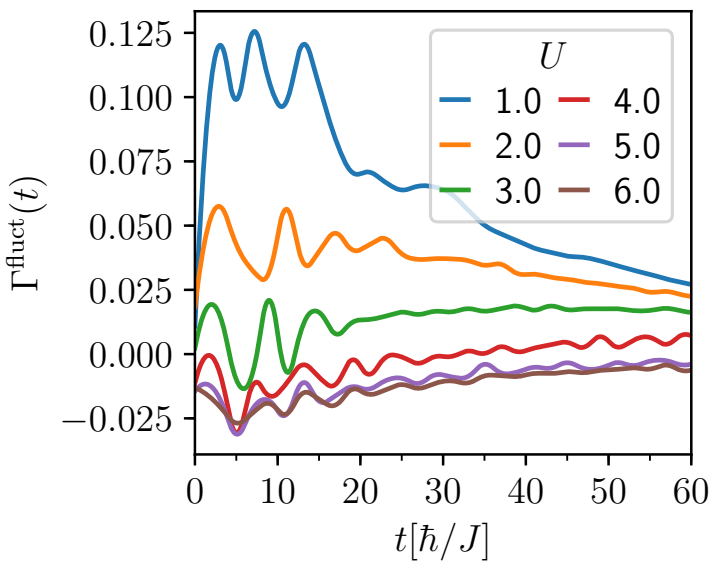

Figure 5.8: *Rate of number fluctuations in the trap.* In single-particle quantum tunneling there is only one rate, proportional to the survival probability of an escaping atom. Here we show a new rate for the many-body tunneling problem, the *fluctuation rate*, exhibiting a clear boundary between quantum phases. Below the critical point the superfluid has a positive fluctuation rate. Above the critical point the Mott insulator has an intial negative rate, which only later become positive as seen in Figure 5.6- Figure 5.7. Initial oscillations on the time scale of $tJ/\hbar = 0$ to 20 correspond to internal reflections within the trap of size $L_{\text{trap}} = 10$.

5.10 Quantum Entropy

There are many entropy measures in a quantum many-body system. The most relevant one for macroscopic quantum tunneling is the entropy of entanglement generated by escaping atoms. The resulting density matrix of the atoms remaining in the trap is

$$\rho_\ell = \text{Tr}_{j>\ell}(\rho), \tag{5.7}$$

where ℓ is taken as the site at the right-most edge of the barrier, and $\rho = |\psi\rangle\langle\psi|$ is the pure state density matrix formed from the complete time-dependent state. The resulting mixed

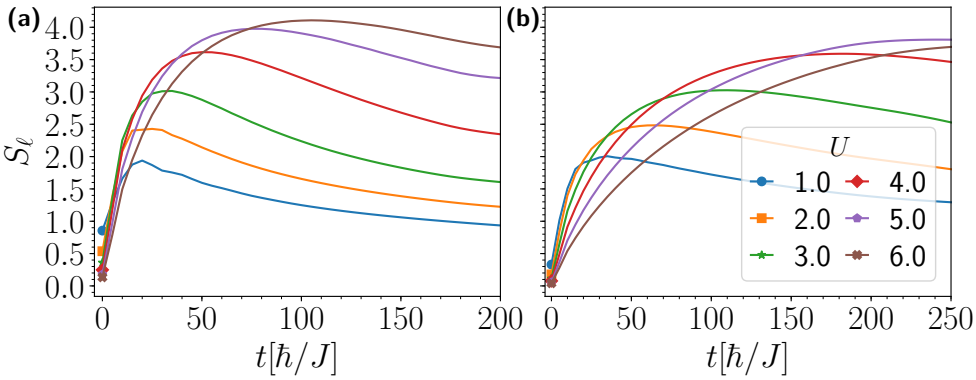

Figure 5.9: *Trap quantum entropy dynamics for superfluid and Mott insulator.* The von Neumann entropy of entanglement between trapped and escaped atoms, S_ℓ, as a function of time for (a) lower barrier height $h/U = 0.9$ and (b) a higher barrier of $h/U = 2.0$. The entropy shows two distinct regimes during the tunneling escape dynamics: rapid rise to a peak value which depends on interactions, and a slow decay. The rise time is slower for higher barriers as a few atoms must tunnel for entropy to build up. The maximal entropy is about twice as high for the strongly interacting regime of an initial Mott insulator behind the barrier.

state has an associated quantum entropy of the trap of

$$S_\ell = -\mathrm{Tr}(\rho_\ell \ln \rho_\ell), \tag{5.8}$$

which quantifies the lack of information about the remaining atoms due to the escaped atoms not being measured. This is in fact a bond entropy, and is a well-known quantity characterizing the convergence of MPS methods [116] as well as area vs. volume law scaling,Page curves, and information scrambling [128]. In our case the bond entropy grows but remains close enough to an area law to be simulatable, as seen in Figure 5.9. To see this, first observe that for N atoms on ℓ sites without other truncations the size of the Hilbert space is $N+\ell-1$ choose N, due to number conservation in the initial state. Then the Hilbert space dimension Ω for $N = 10$ and $\ell = 11$ is $\Omega = 184,756$. The maximal entropy for a maximally mixed state is $S_\ell = \ln(\Omega) = 12.13$. As we observe in Figure 5.9, the maximal entropy ranges from about 2 to about 4 in the weakly to strongly interacting regimes. The bond entropy at other points in the system is lower. Our maximal Schmidt number $\chi = 200$ yields an entropy of $\ln(200) = 5.29$. This is another way to demonstrate convergence beyond the discussion in

Sec. 5.4.

The initial state at $t = 0$ in Figure 5.9(a) has a higher trap quantum entropy S_ℓ for weak interactions because the superfluid has a tail extending further into the barrier. This effect is suppressed by a higher barrier, shown in Figure 5.9(b). As the tunneling escape process ensues the initial superfluid and Mott states at first sight show similar dynamics. A rapid rise time is followed by a slow decay. Both the rise time and the decay time are slower for stronger interactions, and seem to vary smoothly with U/J. A higher barrier again differentiates these regimes more strongly, just like with the suppression of coherent interference patterns observed in Sec. 5.7. This is because a higher barrier makes the initial state more strongly commensurate, and therefore a better Mott insulator in the strongly interacting limit.

However, there are in fact two key differences between the superfluid and Mott insulating regime. First, the Mott insulator shows a maximal entropy which is about twice that of the superfluid, as observed in Figure 5.9. This maximum occurs slightly later in time, but considering how slowly the Mott insulator tunnels, it is important to ask not at what time the entropy maximum occurs, but for how many escaped atoms it occurs. In Figure 5.10 we plot the trap entropy as a function of the number of escaped atoms, scaled to the total number. In this view, all barrier heights nearly collapse onto each other for a fixed interaction strength, except in the initial state in Figure 5.10 where in the superfluid regime the initial penetration of the tail into the barrier is suppressed by higher barriers, therefore decreasing the initial entropy. Thereafter the tunneling escape dynamics, as followed by the number of atoms tunneled collapses nearly all onto the same curve, and depends mainly on the interaction strength. This brings us to the second key difference between the superfluid and Mott insulator regime. In the superfluid case, the trap entropy maximizes when about half the atoms have tunneled, while in the Mott insulator case, maximization occurs when only about one quarter of the atoms have escaped. Thus in the Mott insulating case it takes only a small fraction of the atoms to carry away the maximal amount of information and

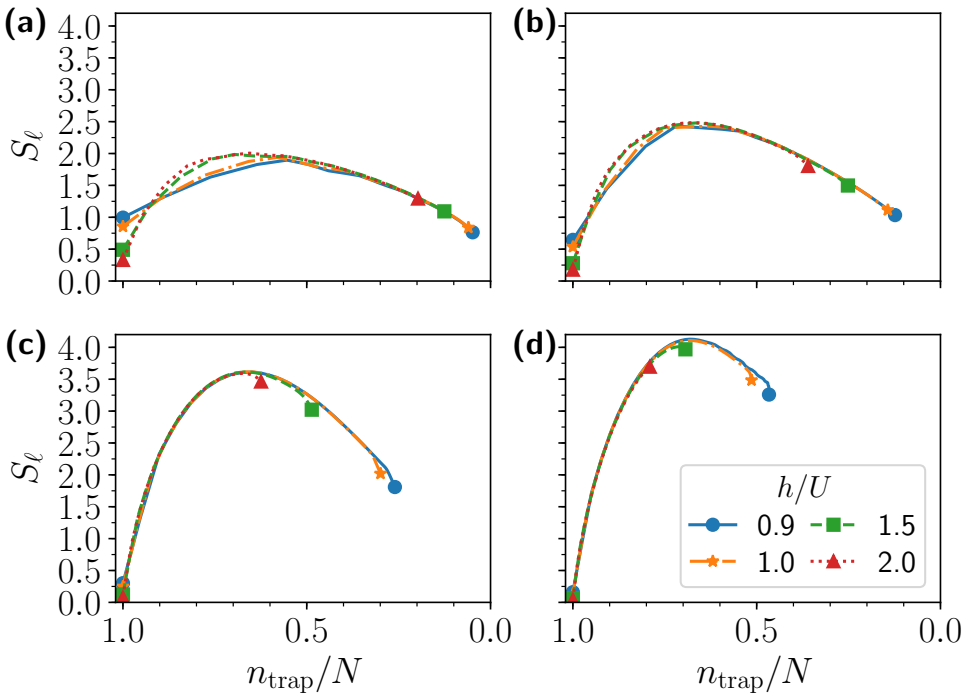

Figure 5.10: *Trap quantum entropy dependence on the number of escaped atoms.* $S_\ell(n_{\mathrm{trap}}/N)$ for trap heights h/U=0.9, 1.0, 1.5, 2.0 and increasing interaction strength from (a) superfluid regime, $U = 1$, (b) $U = 2$, (c) $U = 4$, to (d) the Mott insulator regime $U = 6$, all for $N = 10$. The effects of the barrier are very weak in this view, whereas the effects of interactions are quite noticeable. The maximal entropy of the superfluid is about half that of the Mott insulator. In the superfluid case, the trap entropy maximizes when about half the atoms have tunneled, while in the Mott insulator case, maximization occurs when only about one quarter of the atoms have escaped.

drive the remaining trapped atoms toward their maximum entanglement, as compared to the superfluid.

5.11 Number Correlations in Macroscopic Quantum Tunneling

So far we have considered only local or scalar terms, such as the tunneling rate, the fluctuation rate, and the quantum entropy in the trap during the escape process. However, quantum phases are best characterized by second-order correlations [2, 65]. For the superfluid to Mott insulator transition, these take the form of number correlations. The number fluctuations studied in Sec. 5.9 and the fluctuation rate considered only the local, diagonal part of the number correlations. We now consider local simultaneous measurements of separated regions, or the off-diagonal part. In Sec. 5.12 we highlight the role of positive and negative correlations in the superfluid and Mott insulator regimes, and in Sec. 5.13 we present preliminary evidence of an application using the barrier to control pulsed and continuous-wave correlations.

5.12 Positive and negative correlations

In order to examine the question of the evolution of the quantum phase during the tunneling process, we therefore turn to the second order number correlator, given by

$$g_{ij}^{(2)} \equiv \frac{\left\langle \left(\hat{n}_i - \langle \hat{n}_i \rangle\right)\left(\hat{n}_j - \langle \hat{n}_j \rangle\right) \right\rangle}{\sqrt{\langle \Delta n_i \rangle^2}\sqrt{\langle \Delta n_j \rangle^2}} \tag{5.9}$$

$$= \frac{\langle \hat{n}_i \hat{n}_j \rangle - \langle \hat{n}_i \rangle \langle \hat{n}_j \rangle}{\sqrt{\langle \hat{n}_i^2 \rangle - \langle \hat{n}_i \rangle^2}\sqrt{\langle \hat{n}_j^2 \rangle - \langle \hat{n}_j \rangle^2}} \tag{5.10}$$

Throughout our plots of $g_{ij}^{(2)}$, we subtract off the diagonal correlations as otherwise off-diagonal correlations can only be seen on an inconvenient log scale. In Figure 5.11 we show Eq. (5.9) at the onset of macroscopic quantum tunneling highlighted in our study of the fluctuation rate in Figure 5.8. For a trap of size $L_{\text{trap}} = 10$, at $t = 20$ in our units of $\hbar/J$, oscillations damp out as the internal reflections within the trap have had time to escape. In

all panels, the two pale horizontal and vertical lines at $i = 11$ and $j = 11$ indicate the presence of the barrier, dividing the plots into four distinct regions. The lower-left 10×10 region of $i, j \leq 10$ shows correlations within the atoms remaining in the trap. The vertical-left region for $j \leq 10$ and $i > 11$ is equivalent to the lower right region with $i \Longleftrightarrow j$ corresponds to correlations between the trap and the escaped region. Finally, the large upper-right region with $i, j > 11$ contains correlations purely within the escaped region.

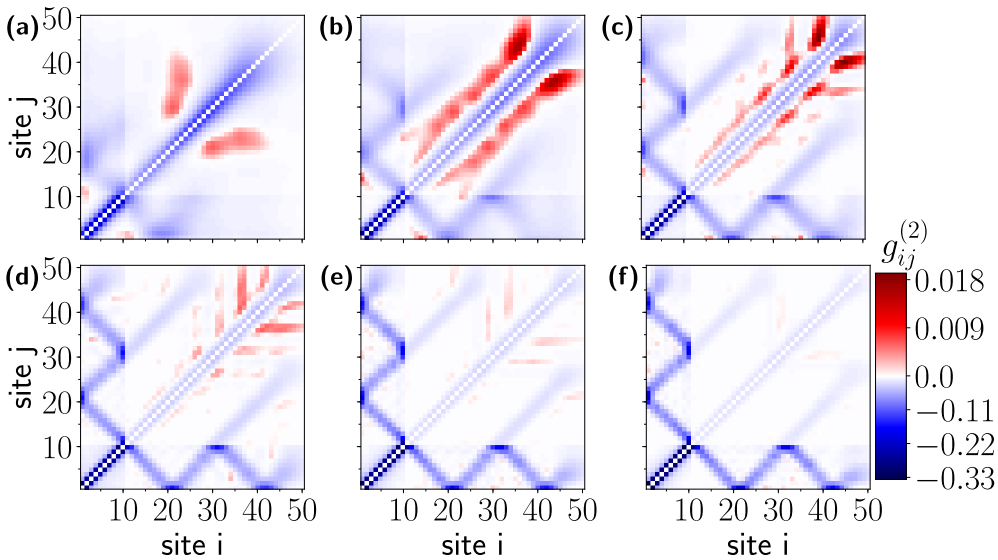

Figure 5.11: *Off-diagonal number correlations at the onset of macroscopic quantum tunneling.* Two-point correlators at $t = 20$, $N = 10$, $L_{\text{trap}} = 10$ for increasing interaction strength from superfluid regime (a) $U = 1$ and (b) $U = 2$ to the critical region (c) $U = 3$ to (d) $U = 4$ to the strongly interacting Mott insulating regime from (e) $U = 5$ to (f) $U = 6$. Starting near the critical interaction strength, $U = 3$, a multiple off-diagonal "fork-like" feature emerges and is persistent. Above $U = 4$, the positive correlation regions become increasingly less pronounced. Note negative (blue) and positive (red) correlations have separate scales to highlight the role of positive correlations more clearly.

We first observe that positive correlations are created in the escaped region for the initial superfluid regime in Figure 5.11(a)-(b). This is despite the fact that only negative correlations show up within the trap. Thus tunneling of a superfluid through a barrier creates positive correlations where none existed before. We interpret this as due to bunching: atoms tend to tunnel together in clusters a few at characteristic scales of a 1-3 lattice sites, due to

bosonic statistics. A very small amount of positive correlation can also be observed between the sites 1 and 11, but this is due only to the internal reflections at time $t = 20$. Positive correlations extend into the critical region Figure 5.11(c), but quickly begin to fragment in Figure 5.11(d). For the strongly interacting Mott-insulator in Figure 5.11(f), they have disappeared entirely.

In contrast, negative correlations are most pronounced in the Mott insulating regime. In Figure 5.11(e)-(f) a fork-like structure emerges. The sharp lines in the structure emphasize the particle-like tunneling described in Sec. 5.7, here seen very clearly. When a particle has tunneled into the escape region, it is subtracted from the trap region, leading to a clear negative correlation. The slope of the lines in the fork is determined by our choice of units, and is just identical up to a sign throughout this region, ± 10, for 10 sites traversed in 10 time units due to the trap-size of 10. The reflections in the trap-escape region thus occur at 10, 20, 30, 40, etc. This structure emerges in Figure 5.11(c)-(d) showing that the transition to particle-like tunneling occurs in the critical region. The transition is not completely sharp due to the mesoscopic nature of the quantum phase transition as seen in Figure 5.1(c). For larger systems we expect it to be much sharper, but as many quantum simulators outside the field of cold atoms are expected to have about 10 quantum components (qubits, qudits, etc.) on the NISQ computing time scale [54], we focus on the features already readily apparent at mesoscopic scale.

In Sec. 5.8 we emphasized the difference between the dependence of number fluctuations, fluctuation rate, and quantum entropy on the tunneling time vs. the number of atoms escaped. Therefore, as a complement to Fig. Figure 5.11, in Fig. Figure 5.12 we show the difference between correlations in the superfluid, critical, and Mott insulating regimes when approximately 1/3 of the atoms have escaped from the trap. The fork-like structure that emerges near the critical regime, $U = 3$ in Fig. Figure 5.12, has weaker negative correlations, but is still persistent. However, periodic structure in the positive correlations at the onset of macroscopic quantum tunneling around the critical region, $U = 3, 4$ in Fig. Figure 5.11(c,d),

is no longer present. The rate of escaping atoms is much slower, producing only a faint positive correlation region in Fig. Figure 5.12(c,d). In the Mott insulating regime, $U = 5, 6$ in Fig. Figure 5.12, the negative correlation fork-like structures dominate the dynamics, with diagonal lines of negative correlation indicating that at each reflection time of $t = 10, 20, 30, 40, 50, \ldots$ in the trap another atom has a chance of being emitted at the barrier. An average negative correlation pattern like this will be built up over many experiments, in each of which a single atom either is or is not emitted.

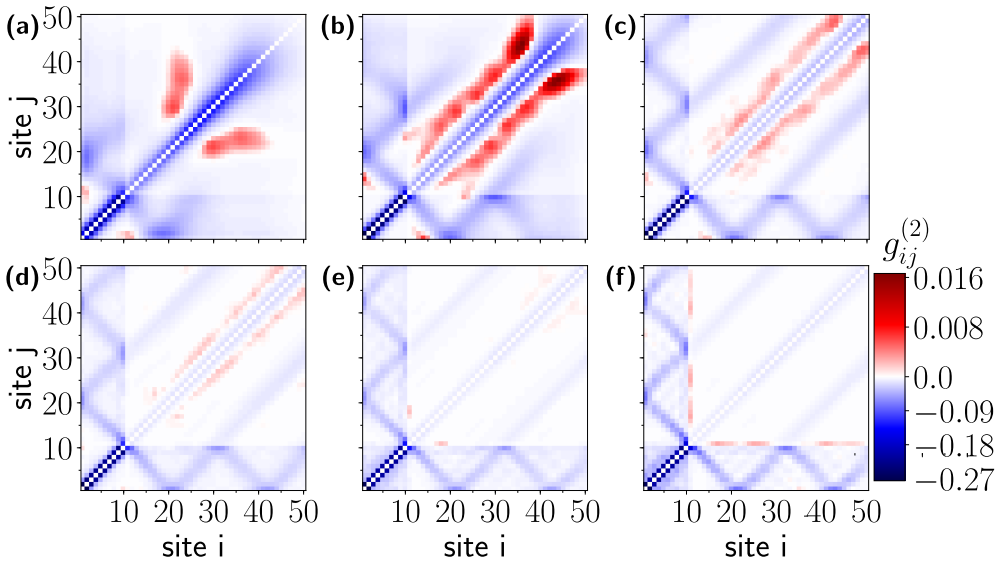

Figure 5.12: *Off-diagonal number correlations when 1/3 of the atoms have escaped.* Same plot as Fig. Figure 5.11, but for a fixed number of escaped atoms rather than a fixed time: (a)-(f) $U = 1, 2, 3, 4, 5, 6$. Near the critical region, $U = 3$, the positive correlations in the escape region begin to damp out, and are entirely lost in the Mott insulating regime of $U = 5$ to $U = 6$, while the fork-like structures persist showing negative correlations between the escape region and the trap. Note negative (blue) and positive (red) correlations have separate scales to highlight the role of positive correlations more clearly.

5.13 Preliminary evidence of a pulsed and continuous-wave correlation atom laser

Finally, we want to emphasize an application of this work to atom lasers. The orignal concept of the atom laser was continuous-wave and emphasized the emission of atoms through a hole in a harmonic trap created by a localized state transition in the atoms [129].

This is a classical hole – no quantum tunneling was involved. It was subsequently shown that attractive interactions could be used to create a pulsed solitonic atom laser [130, 131]. Although the emphasis in these works was on number density, the correlations in the tail for an atom laser were measured experimentally in [132], leading to the field of atom interferometry and the remarkable observation of up to 10th order phase correlators [133]. It was subsequently suggested that tunneling could cause fragmentation, or condensation into multiple modes, in attractive BECs in particular [35].

In Sec. 5.13 we observed the creation of strong positive correlations in the escaped region in the superfluid region. This effect can be further enhanced and focused by controlling the barrier height and interaction strength, creating a correlation atom laser. Such atom laser concepts have potential use in the field of atomtronics [134], where the flow of information may occur not only in currents and densities but also in higher order fluctuations. In Figure 5.13 we show how the barrier can be used to control off-diagonal number correlations. For a low barrier and weak interactions the positive correlations appear in bursts, similar to the "blips" observed in the mean-field semiclassical limit of [122] but here seen in a higher order off-diagonal quantity. However, higher barriers and stronger interactions create extended and structured regions of positive correlation which flow continuously through the escape region. Thus one can tune from pulsed to continuous-wave positive correlations by raising the barrier and tuning interaction within the superfluid regime.

We emphasize that the results of this section are preliminary and merit further detailed exploration of different pulsed and continuous-wave regimes, as this Article is not intended to focus on device applications. For instance, our pulses range from about 2×3 sites to about 3×8 sites, indicating the barrier can used to shape as well as localize various off-diagonal correlation structures. The axes of interactions vs. barrier size vs. initial filling factors all require a detailed study.

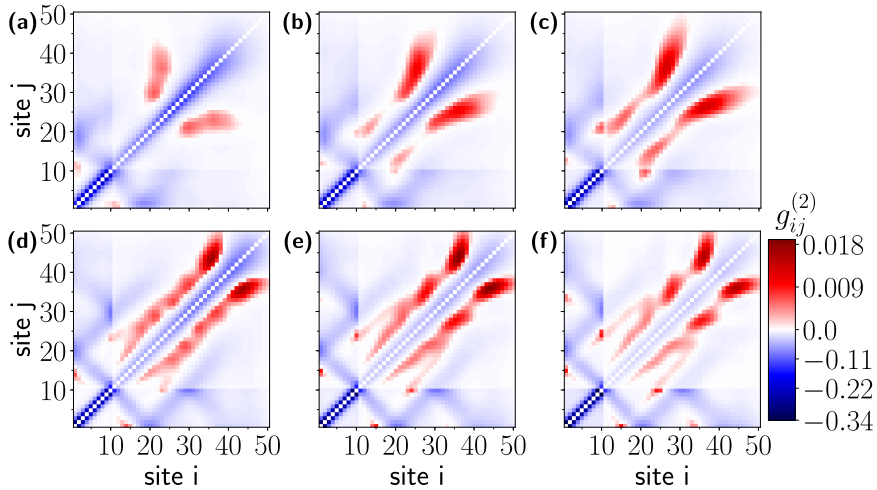

Figure 5.13: *Preliminary demonstration of a correlation atom laser.* Barrier height and interactions are is used to control Top row $U = 1$ and Bottom row $U = 2$, with columns, from left-to-right, $h/U = 1.0, 1.5, 2.0$. All at time $t = 20$. Larger barriers do not decrease the correlation strength, but instead produce visibly different positive correlation regions.

5.14 Conclusions

We have demonstrated that two quantum phases, the superfluid and Mott insulator, show distinct macroscopic quantum tunneling escape dynamics. This result is complementary to the Kibble-Zurek mechanism, in that non-equilibrium dynamics are determined primarily by the characteristics of quantum phases in the ground state, and change radically across a quantum phase transition. To demonstrate this new regime of macroscopic quantum tunneling, we evolved an entangled initial state of the Bose-Hubbard Hamiltonian modeling cold atoms in optical lattice quantum simulators trapped behind a narrow barrier of controlled height. We found the effects persisted even in the mesoscopic regime of 10 particles on 10 sites accessible to many present or near-term quantum simulator platforms beyond cold atoms [54], and are therefore experimentally realizable.

The subsequent dynamics were first characterized by analogies to single-particle tunneling, where highly non-exponential decay was observed. In the weakly-interacting superfluid regime tunneling dynamics were found to be wave-like, with coherent interference patterns in the escape region, and decay was rapid and non-exponential, leading to a rapidly diminish-

ing and non-constant tunneling rate. This is interpreted as due to the single-particle energy (equivalent to a chemical potential) dropping relative to the barrier height. In the strongly-interacting Mott insulator regime we found particle-like tunneling, which was interpreted as suppression of two-particle tunneling events by the Mott gap. The tunneling rate was found to also be non-constant, was an order of magnitude smaller despite stronger repulsive interactions, and decreased nearly linearly. Overall, this effect is caused by the resistance of a Mott insulator to particle flow or mass current.

Beyond such analogies to single-particle tunneling, we explored number fluctuations. We defined a new tunneling rate, the *fluctuation rate*, which can be used to characterize tunneling of fluctuations beyond the semiclassical picture. We found that while the superfluid always has a positive rate, the Mott insulator at first has a negative rate, during which fluctuations actually increase, before they again decrease as the trap empties. We explained this effect using the weakly and strongly interacting limits of the BHH, showing that when atoms tunnel one-by-one for strong interactions, fluctuations are maximized when about half the atoms have tunneled. We then went on to examine quantum entropy created in the trapped atoms during the tunneling escape process, where we found that while in the superfluid regime entropy is maximized when about half the atoms have tunneled, whereas in the Mott insulator regime twice the amount of entropy is created and this occurs when only about one-quarter of the atoms have tunneled. Our interpretation of these numerical results remains an open question for future research.

Finally, we emphasized the nature of the tunneling process in off-diagonal second-order number correlations. We showed the superfluid phase creates positive correlations in the escape region, similar to the bunching effect seen in other contexts, from entangled electrons [135] to the quark-gluon plasma [136]. The Mott insulator phase leads to negative correlations between the trap and the escape region, demonstrating the single atom character of tunneling, further highlighting the role of the gap. Only at very late times when the the fluctuation rate again turns positive have enough particles been emitted that some of

the superfluid character is recovered.

Applications of quantum phases in tunneling devices have been suggested in the context of Josephson junctions [137, 138]. The escape dynamics considered here present a generalization of the concept of an atom laser [129], where correlations have already been measured explicitly [132]. Our work thus offers the possibility of future technological applications in guiding and controlling entangled quantum matter from atomtronics [134] to quantum information science. In particular, we offered a very preliminary demonstration of pulsed and continuous-wave correlation atom laser regimes controlled by barrier height and interaction strength, which bear further investigation. Likewise, the Mott insulator quantum phase can used to control emission of atoms one-by-one rather than collectively.

In future investigations, exploration of macroscopic tunneling dynamics of a variety of quantum phases presents itself as a natural growth of the work here. From the Fermi-Hubbard model to Ising models to Heisenberg models to exotic XYZ magnetism and many other phases of quantum matter, quantum simulators [54] can directly access macroscopic quantum tunneling dynamics. Especially when such calculations are inaccessible on a classical computer the many quantum simulator platforms offer an exciting opportunity to answer such fundamental questions in quantum dynamics as the nature of macroscopic quantum tunneling.

5.15 Acknowledgments

We acknowledge useful conversations with Joseph Glick, Matthias Weidemueller, and Xinxin Zhao. This work was performed in part with support by the NSF under grants OAC-1740130, CCF-1839232, PHY-1806372; and in conjunction with the QSUM program, which is supported by the Engineering and Physical Sciences Research Council grant EP/P01058X/1.

CHAPTER 6

MANY-BODY QUANTUM TUNNELING: DOUBLE WELL AND ADDITIONAL RESULTS ON ESCAPE

The work in this chapter stems from two sources. First, Section 6.2, my contributions to [137], and second, Section 6.2, additional work that was unpublished in Chapter 5. I acknowledge co-authors Marie A. McLain and Lincoln D. Carr for their contributions to both works. The first project, with primary author Marie A. Mclain, studied a double-well system, while the second project, primary author Diego A. Alcala, studied escape into free space; both looking at the Mott-Superfluid quantum phase transition.

6.1 For High-Precision Bosonic Josephson Junctions, Many-Body Effects Matter

This research focuses on the interplay of two quantum phase transitions, $\mathbb{Z}_2$ spontaneous symmetry breaking and the $U(1)$ quantum phase transition between Superfluid and Mott insulators. In a double-well system, the ground state will undergo a symmetry-breaking phase transition by tuning a control parameter beyond some critical value, resulting in asymmetric ground states. This is spontaneous $\mathbb{Z}_2$ symmetry breaking, which leads to a quantum phase transition between Josephson oscillations and self-trapped states [139–141], such as in BEC's [140, 142], and nonlinear optics [143, 144]. Our guiding research question is, how do these two phase transitions influence each other in both ground-state and dynamics; the control knobs being interaction for $U(2)$ and barrier height for $\mathbb{Z}_2$. Many-body simulations are done with the BHH using TEBD 2.4, and mean-field results are with theDNLSE, using time-adaptive method. We explicitly look U/J from weak to strong interactions, or strongly-correlated systems, while weakly-interacting [139, 140, 142, 145, 146], and the single-particle limit, which reduces to Rabi oscillations [22, 147], have previously been studied.

The ground state phases are quantified by the ratio of tunneling to interacting energies. The mean-field version [148], with initial population imbalance, n_0, and relative phase between the wells, ϕ_0, is given by

$$\xi_{\mathrm{MF}} = \frac{n_0^2}{2(1+\sqrt{1-n_0^2 cos\phi_0})} \tag{6.1}$$

The many-body analogue of this equation is

$$\zeta_{\mathrm{MB}} = \frac{\sum_{j\in\text{Left Well}} n_j^{(0)}(n_j^{(0)}-1) - \sum_{j\in\text{Right Well}} n_j^{(0)}(n_j^{(0)}-1)}{4(\sum_{\langle j,k\rangle\in\text{Left Well}}(\rho_{jk}^{(0)}+\rho_{jk}^{(0)*}) - \sum_{\langle j,k\rangle\text{Right Well}}(\rho_{jk}^{(0)}+\rho_{jk}^{(0)*}))}, \tag{6.2}$$

with the number at site j at time $t=0$, $n_j^{(0)}$ and $\rho_{jk}^{(0)} \equiv \langle \hat{b}_j^\dagger \hat{b}_k^\dagger \rangle (t=0)$. These equations describe the dynamical regimes for,

- $\xi < 0$: Josephson oscillations
- $\xi = 1$: the critical point
- $\xi > 1$: the self-trapped "Fock" regime.

The energy ratio phase predictions for both many-body and mean-field are shown in Figure 6.1. For interactions $U/J \leq 1$, both xi_{MF} and xi_{MB} predict the $\mathbb{Z}_2$ phase transition through $V_0 = 1$. For stronger interactions beyond $U/J = 2$, the mean-field energy ratio, unlike ξ_{MB} stays below the critical value, failing to predict the symmetry-breaking phase transition from Josephson to Fock dynamics.

Beyond energy ratios, we also look at on-site number expectations for weak Figure 6.2(a), $U/J = 0.3$, and strong Figure 6.2(b), $U/J = 30$ interactions. Weakly interacting ground states are dominated by the superfluid and are "smooth". In stark contrast, strong interactions, show low-lying excitations of particle-hole states. From $V_0 = 3.0$ to $V_0 = 3.5$, there is a drastic smoothing of the ground state in the well Figure 6.2(b)l. This smoothing occurs because the energy barrier becomes comparable to, and then exceeds, the Mott Gap, resulting in near-commensurate filling in the well, i.e., atom occupation inside the barrier becomes much smaller than 1. For both interactions, larger barriers trap larger number of

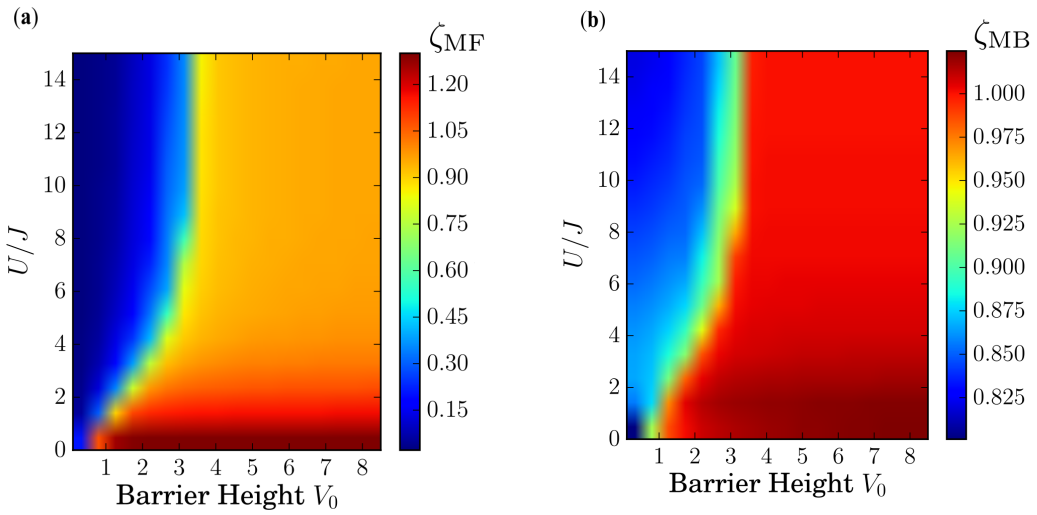

Figure 6.1: *Dynamic regimes predicted by initial states.* Using the ratio of the interaction to the tunneling energy, we can predict dynamics using information from static initial states. For a system of 15 lattice sites and 7 total particles, (**a**) the mean-field energy ratio depicts the Josephson regime in blue, the Fock regime in red for weak interactions, and the orange region does not reach the critical point $\zeta = 1$: the mean-field ratio fails to predict the symmetry-breaking phase transition for stronger interactions. In contrast, the many-body energy ratio (**b**) demonstrates a decisive Fock region in red where $\zeta_{\mathrm{MB}} = 1$ for all interaction strengths.

atoms, increasing population imbalance.

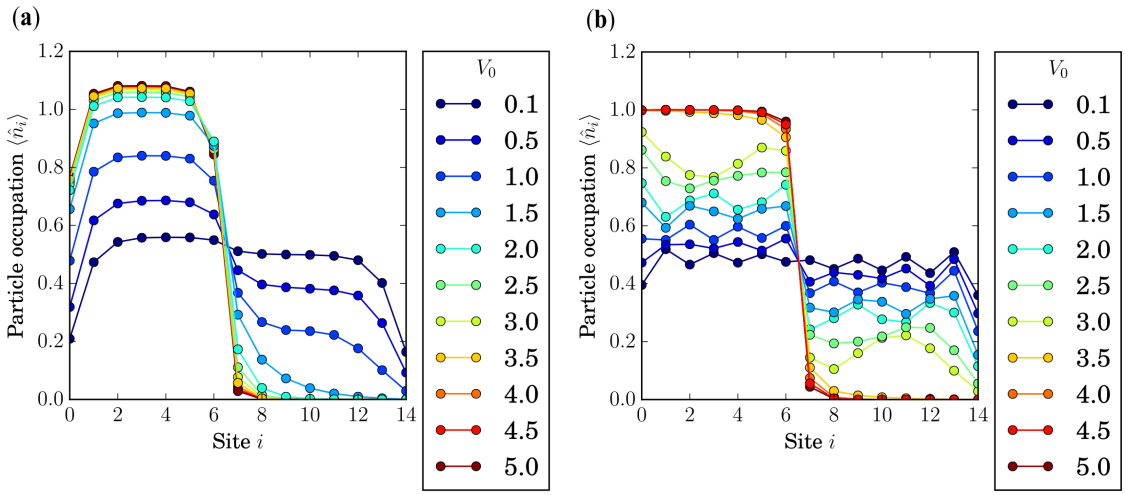

Figure 6.2: *Initial bound states through the Mott-superfluid critical point.* State initialization traps the bosons largely in the left well for an optical lattice with 15 sites and 7 total particles. (**a**) Beyond the Mott-superfluid critical point, interactions are weak, $U = 2.0$, $J = 1$, and smooth superfluid behavior aligns more closely with mean-field theory. (**b**) In the Mott regime, interactions are strong, $U = 15$, $J = 1$, and low-lying excited modes inject deviations from mean-field theory that provide significant influence even with fluctuations as small as ± 0.05 particles.

Mean-field for stronger interactions are found to be "stiff' and required adaptive methods to properly converge. For weak interactions, $U/J = 0.3$ in Figure 6.3(a), mean-field and many-body dynamics of population imbalance qualitatively agree. Josephson dynamics occur for $V_0 = 0.2$, since the initial population imbalance is below the critical value of $n_0 = 0.5$; critical population imbalance is found by setting $xi = 1$ and relative phase $phi_0 = 0$ in the energy imbalance equation. Larger barriers are in the self-trapping regime, where a time-averaged current is near zero, which both ξ_{MB} and xi_{MF} predict. Strong interactions, $U/J = 30$ in Figure 6.3(b), has Josephson oscillations for all barrier heights in the mean-field. The Fock regime for $V_0 = 5$, as predicted by xi_{MB}, is clearly visible, with most atoms remaining trapped inside the well. Strong, Mott dominated, interactions are not expected to be modeled well by a mean-field, which does not capture the large fluctuations and

correlations produced in the system.

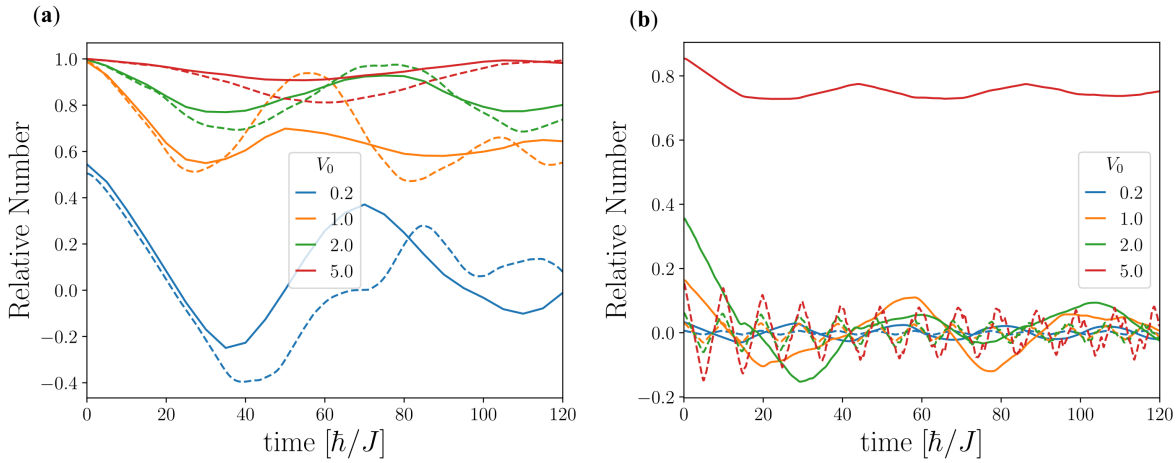

Figure 6.3: *Weak interaction similarities and strong interaction disparities: TEBD and GPE.* For a system of 27 lattice sites and 14 particles, GPE (dashed curves) and TEBD (solid curves) simulations show (**a**) agreement of dynamical regimes for weak interactions and (**b**) a GPE failure to predict self-trapping for strong interactions. (**a**) Larger barrier heights $V_0 = 1, 2$, and 5 are self-trapped for $J = 1$ and $U = 0.3$, and the low barrier $V_0 = 0.2$ is in the Josephson regime. (**b**) For $J = 1$ and $U = 30$, TEBD results (solid) predict self-trapping for a barrier height of $V_0 = 5$ whereas GPE results (dashed) predict Josephson oscillations for all barrier heights.

While population imbalance gives the gross dynamical features, on-site occupation shows more aspects of many-body dynamics, and further demonstrate the phase transition from Josephson to Fock regime. For weak interactions, $U/J = 0.3$ in reffig:weakpt, the superfluid dominates, and interference of wave-like dynamics from delocalized groups of atoms are clearly visible from Josephson Figure 6.4(a) to Fock Figure 6.4(d). Critical population imbalance occurs for Figure 6.4(c,d). While most atoms are self-trapped in the left-well, a few atoms escape, resulting in interference patterns. For strong interactions, $U/J = 30$ in Figure 6.5, the barrier induced $\mathbb{Z}_2$ phase transition is also visible from $V_0 = 0.2$, Figure 6.5(a), to critical $V_0 = 1$, Figure 6.5(b), and then $V_0 = 3.0, 5.0$ for Figure 6.5(c,d), respectively. The transition to self-trapping, as predicted by the many-body energy ratio, occurs at $V_0 = 3$. The Mott-dominated interactions create localized excitations throughout the well, a start

contrast to the spread-out superfluid dynamics. The Josephson oscillations for these Mott-dominated interactions are likely due to a superfluid fragment or film overlaying the Mott-insulated atoms [149].

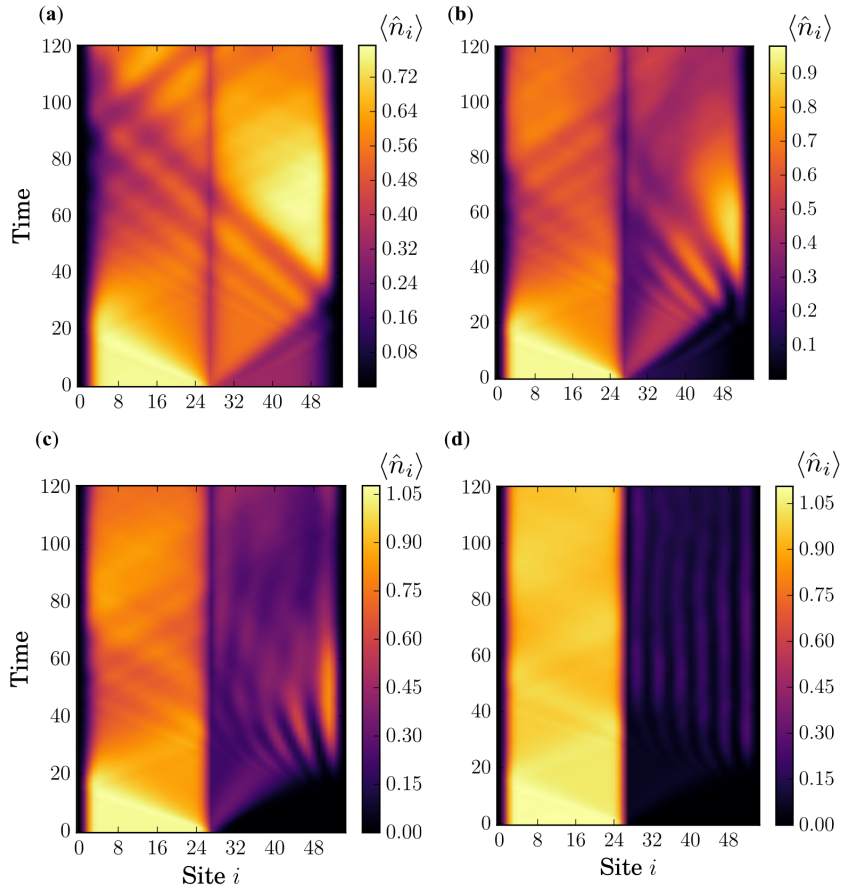

Figure 6.4: *Weakly-interacting spontaneous symmetry breaking transition.* Tunneling dynamics range from (**a**) the Josephson regime to (**d**) the Fock self-trapping regime for a system of 55 sites and 27 atoms, $U = 0.3$ and $J = 1$. The barrier height increases from (**a**) $V_0 = 0.2$ to (**d**) $V_0 = 2$. In the critical regions, (**b**) $V_0 = 0.4$ the dynamics are Josephson-like with interference patterns due to the interferometer nature of the double well. The diffraction fringes become more pronounced in the right well as the barrier height increases to (**c**) $V_0 = 0.6$ and becomes self-trapped in (**d**).

Additional important results in the manuscript [137], which we mention here for completion, but are and beyond the scope of this thesis include the following. Observation of symmetry-breaking particle-hole solitons for incommensurate filling in the wells. Dynamics

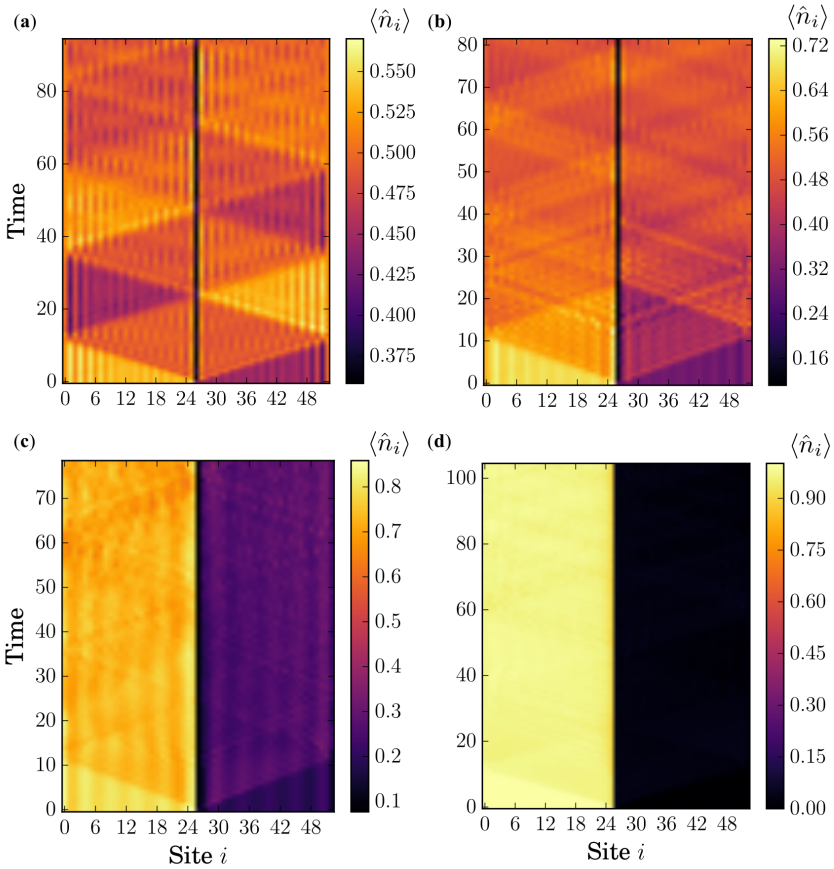

Figure 6.5: *Strongly-interacting spontaneous symmetry breaking transition.* For low barriers such as (**a**) $V_0 = 0.5$, particle-holes emerge across the entire lattice. Through the critical region of (**b**) $V_0 = 1$, the damping is large and phase coherence rapidly decays – likely due to interaction of the quasiparticles with the condensate. Just beyond the critical point into the Fock regime for $V_0 = 3$ (**c**), the nonlinear waves that would otherwise dominate the dynamics are suppressed, making way for more timid modes of the double well, a result of the diabatic quench: these modes are sustained for unexpectedly long time scales. Finally, the bosons are self-trapped (**d**) for a larger barrier, $V_0 = 5$.

of depletion for strong interactions clearly show the influence of the Mott gap. Classification of fluctuation, g^2, dynamics: self-trapping, symmetric fluctuations, and the "Fock flashlight" for strong interactions. Finally, sudden approximation and second-order perturbation theory were used to show how the non-adiabatic quench of the barrier, the drop at time $t = 0$, tends to favor excitation of modes with comparable symmetry to the well and whether there are an odd or even number of sites.

6.2 Additional Results for Quantum Phases Drive the Dynamics of Macroscopic Quantum Tunneling Escape in Quantum Simulators

This subsection includes a set of preliminary results and findings that were not pursued further when completing the manuscript for Chapter 5. These results arose from studying the escape velocity of atoms after they had tunneling through the barrier. As the preliminary results in this subsection will indicate, the question of escape velocity quickly becames a question about atom transport and information speed limits, such as the well-known Lieb-Robinson bound [150–153]. This went beyond the scope of the manuscript, which sought to understanding how QPTs modified the tunneling dynamics through the barrier. We present preliminary results which show how interaction strength in the BHH can alter the speed of propagation of the bulk of atoms after tunneling through the barrier. Furthermore, we present sudden approximation results, in which atoms can expand freely, without a barrier present. These results indicate that the number of atoms can have a strong influence on atom transport and expansion. This exploration uncovers many more questions than are answered regarding the expansion of atoms, with and without tunneling through a barrier in the BHH, and forms the basis of a potential future paper; much more rigorous analysis and convergence studies are required.

After atoms tunneling through the barrier in the BHH, they further interact and expand in the escape region. To quantify an "escape velocity", we use a simple approximation of tracking the site with the largest occupation of atoms, $\langle \hat{n}_i \rangle$. Figure 6.6(a) is heatmap of on-site number expectation value, $\langle \hat{n}_i \rangle$, with a teal line showing the maximally occupied site

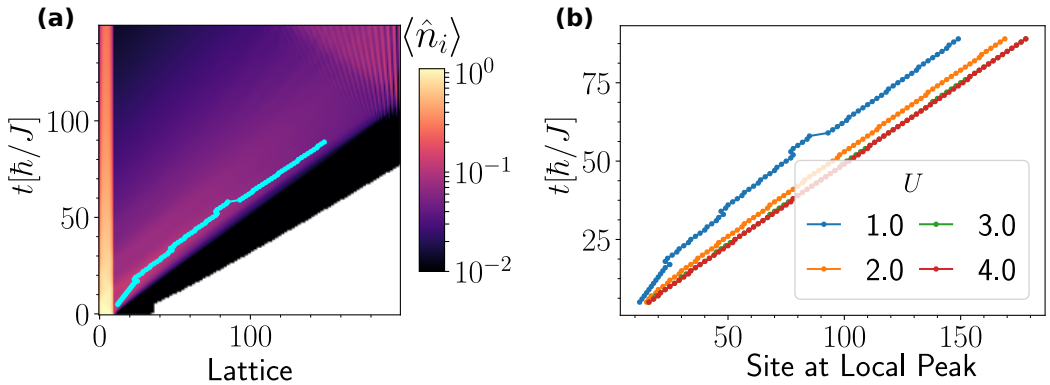

Figure 6.6: *Interactions Increase the Escape Peak Velocity.* (a) heatmap of on-site number occupation, $\langle \hat{n}_i \rangle$ for $N = 10$, $U = 1$, $h/U = 1.5$, and $L = 200$. The peak, teal blue line, is the location of largest $\langle \hat{n}_i \rangle$ in the escape region. (b) the escape region peak for various values of U. Superfluid tunneling, $U = 1$, has strong wave properties in the escape region which results in the peak shifting around slightly as the atoms coherently interfere. Stronger interactions produce faster travel in the peak lines, approaching a slope of 2 sites per time unit.

in the escape region, for $U = 1$ and $h/U = 1.5$. Starting around $t \approx 5$, the teal line moves into the lattice, where the slope of the line approximates the escape velocity, reaching site $i \approx 160$ at $t \approx 90$. For $U = 1$, the long-wavelength nature of the escaping atoms produces wiggles and sudden shifts between a few sites. Note, these are preliminary studies and the lattice is not big enough to prevent reflections from the right-hand wall but proves useful in for the sudden approximation studies.

Figure 6.6(b) plots the peak lines for several interaction strengths, $U = 1, 2, 3, 4$. As interactions increase, the lines straighten out, the system is more particle-like as interactions increase through the critical region, $U = 3$ to 4. These straighter lines also indicate a speed increases with interaction strength, and the paths for $U = 3, 4$ are nearly on top of each other. For $U = 1, 2$, the slope, the escape speed, for early times $t \approx 10$ to 15 is somewhat less, suggesting that the escape speed for weak interactions increases as more atoms escape. Even for stronger interactions, the peak lines seem to suddenly jump between sites, due to the digital sampling nature of the peak finding algorithm. We don't find the peak in space; we are simply tracking the most occupied state. A more sophisticated approach would use

fitting algorithms to track the peak moving between sites.

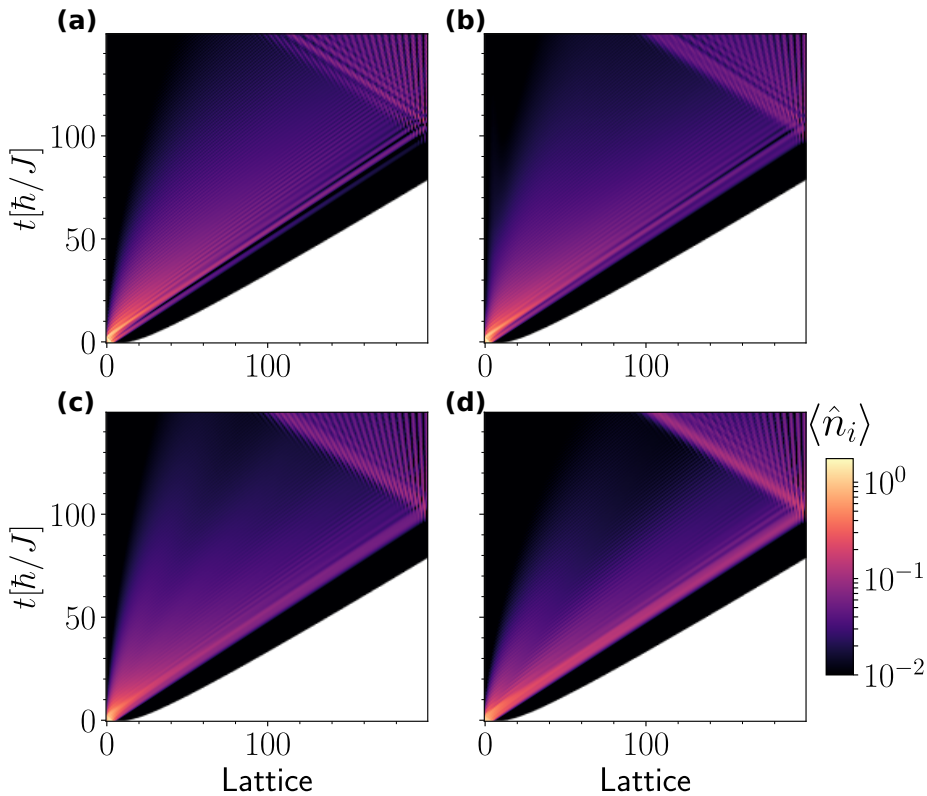

Figure 6.7: *Sudden Approximation for 5 atoms.* A ground state with $N = 5$ and $L = 5$ is placed in a lattice of $L = 200$ with $U = 0.25, 0.5, 1.0, 6.0$ for (a,b,c,d), respectively. All interaction strengths have atoms reaching the end of the lattice near $t \approx 100$.

For the sudden approximation method, we find the ground state with $N = L$, and then place that state into a lattice with $L \gg N$, placed against the left-hand wall, to mimic the tunneling simulations. The motivation is to remove quantum tunneling and the barrier variables, and simply understand the propagation and spreading of tightly packed atoms. First, Figure 6.7 demonstrates very weak to strong Mott-dominated interactions, $U = 0.25, 0.5, 1.0, 6.0$. Recall, the interaction parameter space in Chapter 5 was limited by the barrier, requiring $h/U \gtrapprox 0.9$ for weak interactions. For these few atoms, the interaction strength does not have a strong influence on the speed of the right-most section of atoms. For $U = 0.25, 0.5$, the atoms spread out into a relatively uniform cone, with coherent interference on the scale of nearest neighbors. Starting with $U = 1$, some long-wavelength coherent

interference effects can be seen, with 3 to 4 anti-nodes visible in the expansion region. For $U = 6$, a large collection of atoms travels together, visible as a beam which bounces off the right wall around $t \approx 100$.

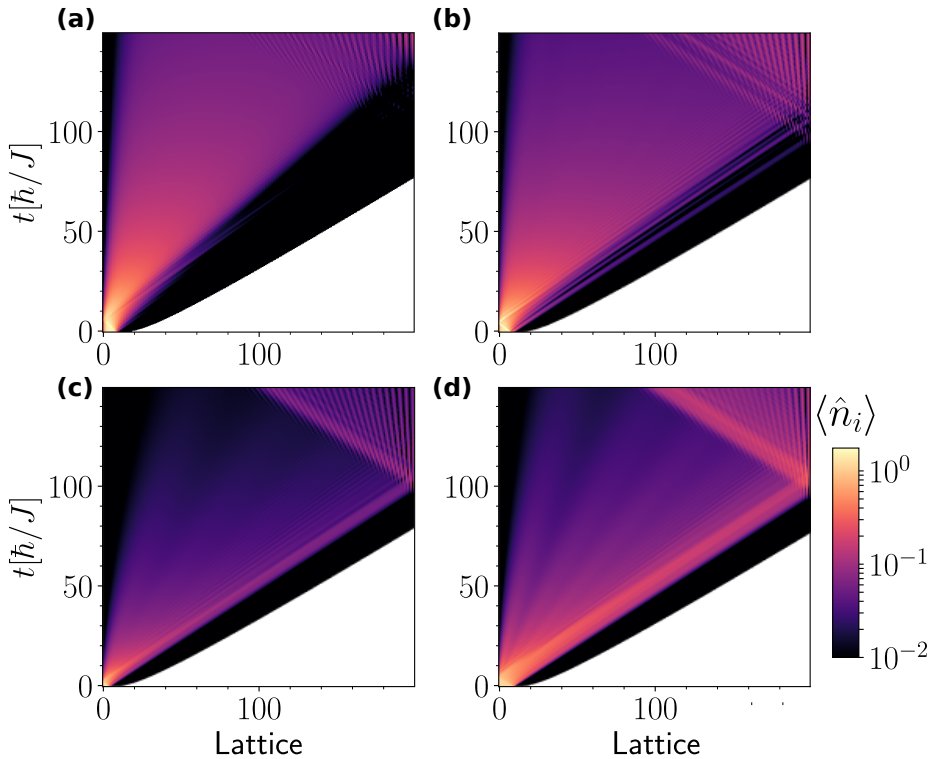

Figure 6.8: *Sudden Approximation for 10 atoms.* Same as Figure 6.7, except for $N = 10$. Interactions cause a significant difference in the expansion speed. The bulk of the atoms reach the end of the lattice for $t \approx 160$ for $U = 0.25$ and near $t \approx 100$.

Increasing the number of atoms to $N = 10$, Figure 6.8, produces some pronounced effects. For $U = 0.25, 0.5$, the expanding atoms form a nearly uniform cone, with the nearest neighbor coherent interference effects from Figure 6.7(a,b), either less visible or completely gone. The expansion velocity is significantly altered by interactions, reaching the right-hand wall at $t \approx 130$, unlike $N = 5$ which reached the wall at $t \approx 100$. The long wavelength coherent interference effects are still visible for $U = 1, 6$. However, here the interference patter is enhanced for $U = 6$, Figure 6.8(d). We note, even though the bulk of the cone for $U = 0.25$, Figure 6.8(d), has a slower expansion speed, there are still visible interference

streaks near $t \approx 120$ and site 160 from atoms which have reflected off the right wall. These seem to emanate from atoms that would have reflected form the wall near $t \approx 100$. Even though these atoms have on-site occupations below 10^{-2}, the black region, they can still produce small visible effects.

CHAPTER 7

MACROSCOPIC QUANTUM ESCAPE OF BOSE-EINSTEIN CONDENSATES: ANALYSIS OF EXPERIMENTALLY REALIZABLE QUASI-ONE-DIMENSIONAL TRAPS

This work is an extension and completion of an unpublished draft by Gregor Urban, parts of which are included in his bachelors thesis [154]. I acknowledge all collaborators in this project. Co-author Gregor Urban for starting this project, writing the initial variational Mathematica code, and authoring the original unpublished draft. Matthias Weidemüller, the principle investigator at Heidelberg University and adviser to Gregor. Lincoln D. Carr, the principle investigator at Colorado School of Mines, and adviser to Gregor and myself. My contributions to this project include: independently running all data except for that in Figure 7.9, running additional ansätze calculations, explicitly fitting scaling laws to all relevant trap parameters, fully describing the ideal trap parameters for BEC of rubidium, lithium, and sodium, and I wrote the published versions of the paper which is completely distinct from the original draft.

7.1 Macroscopic Quantum Tunneling in Symmetric and Linearly Ramped Gaussian Traps

Tunneling times for single-body physics are well known to depend exponentially on the barrier area [3–6, 111, 112], and thus the tunneling time through a barrier can easily go from nanoseconds to longer than the lifetime of the universe with a factor of 7 increase in a barrier. For this reason, tunneling is often restricted to very light objects with small barriers, such as electrons tunneling in scanning tunneling microscopes, or solid state devices like flash memory and tunneling diodes, or light atoms like hydrogen, deuterium, and helium [7, 8, 111, 112]. Despite these restrictions, quantum tunneling is present in carbon atoms tunneling over sub-angstrom scales in complex molecules at Kelvin temperatures [9], and

biological systems see tunneling in the kinetic isotope effect and enzyme catalysis [10–12].

Macroscopic quantum tunneling (MQT) involves tunneling in systems with larger/heavier atoms, molecules, or many interacting atoms, and produces a rich landscape, as discussed in Section 2.1 and [13]. In this chapter, we focus on a dilute ultracold gas with repulsive weakly-interacting boson atoms tunneling out of two experimentally realizable quasi-1D traps; reduction to quasi-1D is fully discussed in Section 2.3.6. First, we consider a symmetric trap formed from two displaced Gaussian barriers. Second, a Gaussian barrier with a linear ramp, in other words, a tilted Gaussian barrier. Both are experimentally realizable with Gaussian lasers and magnetic traps. For example, in Chapter 3, the experiment used the combination of gravity and a magnetic gradient to control the linear ramp, albeit the trap used there was more complicated than the ones tackled in this chapter.

For such systems the GPE, a mean-field approach, which neglects quantum fluctuations, is an adequate approximation [71]. We use a combination of the variational and JWKB methods to approximate the ground states and the calculate the tunneling rates. Both the variational and JWKB methods require some modifications to account for the nonlinearity in the GPE [87, 88], details discussed in Section 7.2. In brief, the variational method requires careful treatment of the normalization condition and the JWKB tunneling probability and classical oscillation frequency integrals include the effective mean-field barrier.

7.2 Variational JWKB Method and Numerical Procedure

The first step in the variational-JWKB method is to find a ground state of the GPE with chemical potential μ,

$$\left(-\frac{\hbar^2}{2m}\frac{\partial^2}{\partial x^2} + V(x) + g|\psi(x)|^2\right)\psi(x) = \mu\psi(x). \tag{7.1}$$

Given some number, m, of variational parameters, $\alpha_1, ..., \alpha_M$, in both the wave function and potential, the total energy is

$$E(\alpha_1, ..., \alpha_M) = \int_{-\infty}^{\infty} dx \frac{\hbar^2}{2m}\left|\frac{\partial\psi(x)}{\partial x}\right|^2 + V(x)|\psi(x)|^2 + \frac{1}{2}g|\psi(x)|^4. \tag{7.2}$$

Crucially, the wave function normalization constants are taken as varational parameters throughout the variational procedure, in other words, not substituted until all parameters are solved for. Numerically, the total energy, Eq. (7.2), and normalization condition, $\langle\Psi|\Psi\rangle = N$, are minimized by finding where partial derivatives with respects to the variational parameters are zero, and checking that the 2nd derivatives and the determinant of the hessian are positive.

The well-known JWKB tunneling rate, Γ, and classical oscillation frequency, ν, are given by,

$$\Gamma = \nu \exp\left(-\frac{2}{\hbar}\int_{x_{\text{in}}}^{x_{\text{out}}} \mathrm{dx}|p(x)|\right) \tag{7.3}$$

$$\nu = \left(m \oint \frac{\mathrm{dx}}{|p(x)|}\right)^{-1}. \tag{7.4}$$

To account for the nonlinearity, $g|\Psi(x)|^2$, in the GPE, the semi-classical momentum, $p(x)$, is modified to include the effective mean-field potential, $V_{\text{eff}}(x)$,

$$p(x) = \sqrt{2m\left(V_{\text{eff}}(x) - \mu\right)} \tag{7.5}$$

$$V_{\text{eff}}(x) = V(x) + g|\Psi(x)|^2,, \tag{7.6}$$

where $g \to 0$ results in the usual expressions. The inner and outer classical turning points, x_{in} and x_{out}, are the points of zero momentum, $p(x_{\text{in}}) = p(x_{\text{out}}) = 0$. For BECs, which are condensed into a single energy state, the atoms in the well move with approximately the semi-classical momentum, $p(x)$ in $V_{\text{eff}}(x)$. The oscillation frequency, Eq. (7.4), is calculated over one oscillation period with the barriers, ν^{-1}; for V_{sym}, Figure 7.1, this would be from one Gaussian barrier to the other and in V_{tilt}, Figure 7.2, this would be from the Gaussian barrier, to the ramp, and back to the barrier.

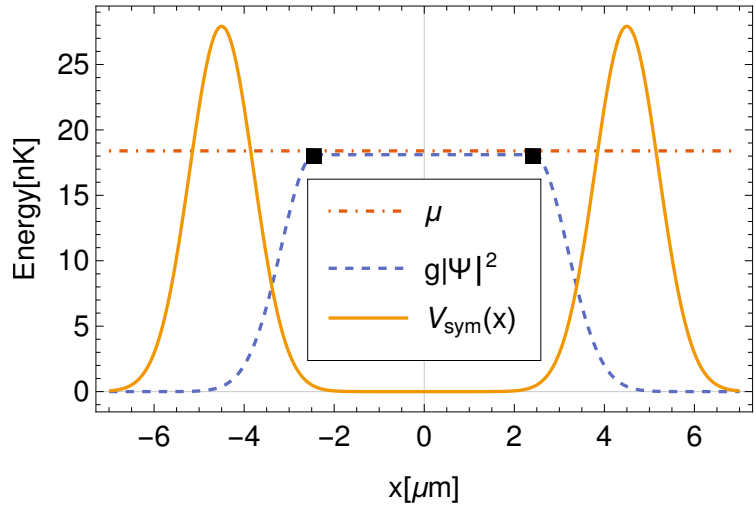

Figure 7.1: *Symmetric trap variational wave function.* A typical wave function solution, $g|\Psi|^2$ (dashed blue line), and chemical potential, μ (dash-dotted red line), for $V_{\text{sym}}(x)$ (solid yellow line) with parameters $V_0 = 27.9$[nK], $\sigma_0 = 1.41[\mu\text{m}]$, and $x_0 = 4.5[\mu\text{m}]$ are shown. Black squares mark the connection points in the wave function between the two Gaussian tails for $|x| > 2.43$ and the flat region in the middle.

7.3 Barrier Configurations and Ansätze

The two potentials we consider are experimentally accessible via a combination of magnetic trapping and lasers,

$$V_{\text{sym}}(x) = V_0 \left[e^{-(x-x_0)^2/2\sigma_0{}^2} + e^{-(x+x_0)^2/2\sigma_0{}^2} \right] \tag{7.7}$$

$$V_{\text{tilt}}(x) = V_0 e^{-x^2/2\sigma_0{}^2} - \alpha_0 x. \tag{7.8}$$

The trap parameters are: separation between the barrier peaks, x_0, the Gaussian width, σ_0, the barrier peak height, V_0, and linear acceleration, α_0. We modify the Gaussian ansatz with a constant (linear) region for the tilt (symmetric) potential, which allows the wave-function to interpolate between a pure Gaussian function and the Thomas-Fermi approximation in wider potentials, Figure 7.1 and Figure 7.2.

For the V_{sym}, the wave function ansatz is given by

$$\Psi(x) = \begin{cases} A \ \exp\left(-|x - x_1|^2/2\sigma_1^2\right) & |x| > x_1 \\ A & |x| \leq x_1, \end{cases} \tag{7.9}$$

with normalization constant, A, Gaussian width, σ_1, and width of the constant region, x_1. The subscript 1 is used to differentiate from the potential parameters, which all have subscript 0. The potential and a solution are shown in Figure 7.1.

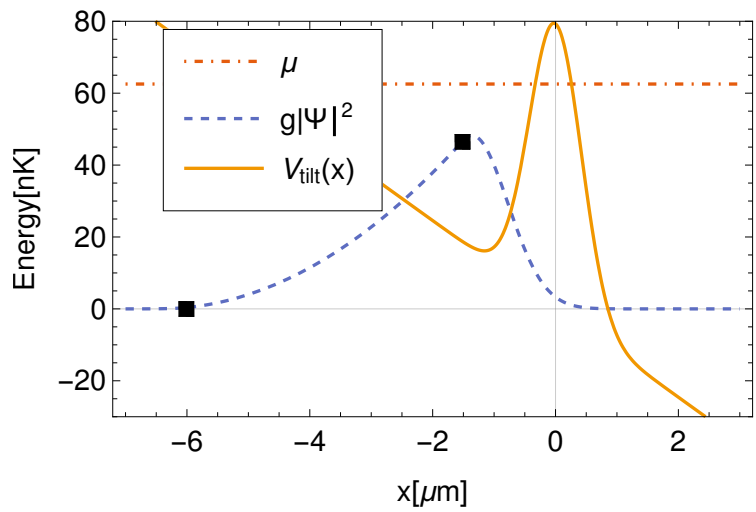

Figure 7.2: *Tilt trap variational wave function.* A typical wave function solution, $g|\Psi|^2$ (dashed blue line), and chemical potential, μ (dash-dotted red line), for $V_{\text{tilt}}(x)$ (solid yellow line) with parameters $V_0 = 79.3$[nK], $\sigma_0 = 0.85[\mu\text{m}]$, and $\alpha_0 = 1.07[\text{m/s}^2]$ are shown. Black squares show the connection points for the different wave function pieces; the left Gaussian tail below $x \approx -6$, middle connection region between $x \approx -6$ and $x \approx -1.5$, and right Gaussian tail above $x \approx -1.5$.

For V_{tilt}, the ansatz wave function is

$$\Psi(x) = \begin{cases} B_L \ \exp\left(-(x+x_L)^2/2\sigma_L^2\right) & x < C_L \\ A_1 x + A_2, & C_L \leq x \leq C_R \\ B_R \ \exp\left(-(x-x_R)^2/2\sigma_R^2\right) & x > C_R, \end{cases} \tag{7.10}$$

with the parameters for the left and right Gaussian tail widths, σ_{L} and σ_{R}, the left and right Gaussian tail offsets, x_{L} and x_{R}, the slope and intercept of the linear function, A_1 and A_2, as well as the normalization constants, B_{L} and B_{R}, and points of connection, C_{L} and C_{R}. The potential and typical solution are shown in Figure 7.1, with black squares showing the connection points.

7.4 Scaling Results in Symmetric Gaussian Traps

Figure 7.3 shows the general trends in tunneling rate for different barrier heights, in V_{sym}, as a function of mean-field strength Ng, given in units of scattering length a_{s}. Each curve has a fixed barrier height, starting with the smallest, left-most curve, $V_0 = 14$[nK] to the largest with 125.6[nK]. Each point corresponds to some interaction strength g, which is swept for each curve until reaching the maximum allowed for that given barrier height, g_{max}. In general, one would expect that larger barriers allow for stronger mean-field interactions in the well, and thus larger tunneling rates, Γ. However, maximal tunneling rates, the peak of any given curve, begins to decrease around $V_0 \approx 85$[nK]. This is due to the creation of mean-field "islands". The mean-field barrier inside the trap exceeds the chemical potential, resulting in an *island* inside the trap. This requires a modification of the classical oscillation calculation, discussed in Section 7.7. Because tunneling rates maximize in narrow range of Ng, we look at scaling laws in the maximal tunneling rate, Γ_{max}, for a given set of barrier parameters.

The maximal tunneling rate as a function of barrier separation for $V_0 = 27.9$ and 85.8[nK], respectively, is shown in Figure 7.4. In general, the barrier height and width do not play a large role in how maximal tunneling rates scale when it comes to barrier separation, for the parameter ranges considered here. For fixed barrier heights and widths, changes in the tunneling rate are mainly due to changes in the classical oscillation frequency. This is apparent with how closely the curves trend, despite the Gaussian barrier width increasing by a factor of 3 in both plots. A visible *kink* is present in all curves near $x_0 = 2, 3$, caused by the appearance of mean-field islands when the traps become sufficiently narrow, and are present for all lower x_0. Since the region before the cusp is smallrelative to the whole figure, the entire curve can be fit by,

$$\Gamma_{\text{max}} \simeq (a_0 + a_1 x_0 + a_2 x_0^2)^{-1}, \tag{7.11}$$

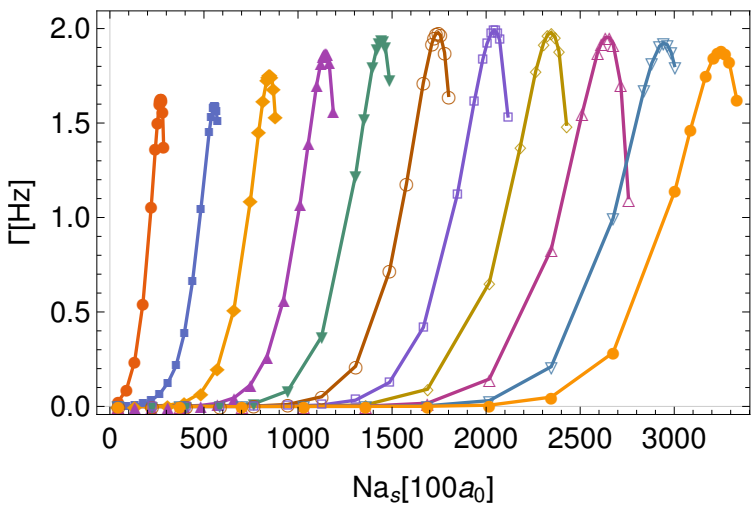

Figure 7.3: *Tunneling rate for various barrier heights.* Tunneling rate vs interaction strength, given by number of atoms N and scattering length a_s in units of Bohr radius a_0, is shown for V_{sym} with 11 equally spaced barrier heights between $V_0 = 14.0$ and 125.6[nK] with parameters $x_0 = 4.5[\mu\text{m}]$ and $\sigma_0 = 1.41[\mu\text{m}]$, assuming transverse frequency $\omega_\perp = 2\pi \times 500[\text{Hz}]$. Larger barriers allow for greater mean-field interaction. The maximal tunneling rate shows a non-trivial trend, initially decreasing, followed by increasing, and then decreasing again. For rubidium, the largest barrier $V_0 = 125.6[\text{nK}]$ would allow $N \approx 3000$. Markers are data with error bars smaller than marker, and curves are a guide to the eye.

with fit parameters a_0, a_1, and a_2. This scaling can be attributed to the classical oscillation frequency being the dominant factor in how $\Gamma_{\max}$ changes, Eq. (7.11).

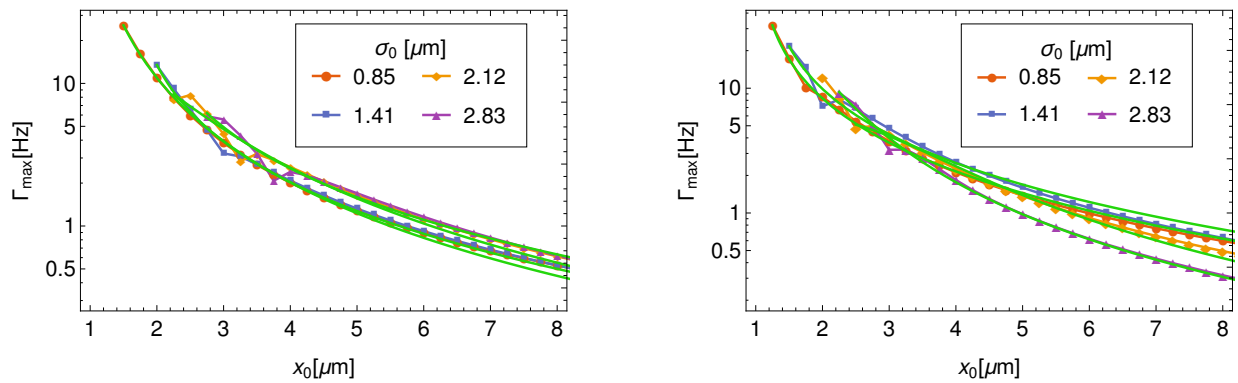

Figure 7.4: *Scaling in barrier separation for symmetric trap.* Maximal tunneling rate $\Gamma_{\max}$ on a semi-log scale as a function of barrier separation for (a) $V_0 = 27.9$[nK], and (b) $V_0 = 85.8$[nK], with various Gaussian widths σ_0; solid green curves are fits and points are data (data points are connected as a guide to the eye). Tunneling rate decreases with both increasing x_0 and increasing V_0. All data exhibit a kink due to the mean-field islands for smaller x_0, but fits still capture the overall trend. Larger σ_0 don't produce bound states for smaller traps. Error bars for data points are smaller than markers.

Scaling in barrier height, with fixed barrier width and separation, are shown in Figure 7.5; narrow Figure 7.5(a) and mid-range Figure 7.5(b) traps with $x_0 = 1.0[\mu\text{m}]$ and $5.0[\mu\text{m}]$, respectively. Narrow traps require smaller Gaussian widths of 0.14 to 0.42[μm]. producing much faster tunneling rates and allow barrier heights an order of magnitude larger. The appearance of mean field islands is apparent in both plots; tunneling rates decrease initial decrease for larger barrier heights, and then reach a cusp and start to increase after the mean-field islands appear. Because the regions before and after the mean-field islands make up a large portion of the curves, scaling is broken up between pre and post cusp regions. Classical oscillations dominate scaling before the kink, where $\Gamma_{\max}$ is decreasing, and we fit scaling to

$$\Gamma_{\max} \simeq V_0(a_0 + a_1 V_0^{a_2})^{-1}, \tag{7.12}$$

yellow fit lines in Figure 7.5(a,b). Weak linear dependence on tunneling probability probably contributes the V_0 factor, while the exponent a_2 is due to nonlinear dependence in 7.5. When the mean-field islands are present and V_0 is larger, tunneling probability contributes more strongly, resulting,

$$\Gamma_{\max} \simeq a_0 \sqrt{V_0} \exp\left[-a_1 V_0\right], \tag{7.13}$$

with the exponential term contributing to the scaling, green fit lines in Figure 7.5(b).

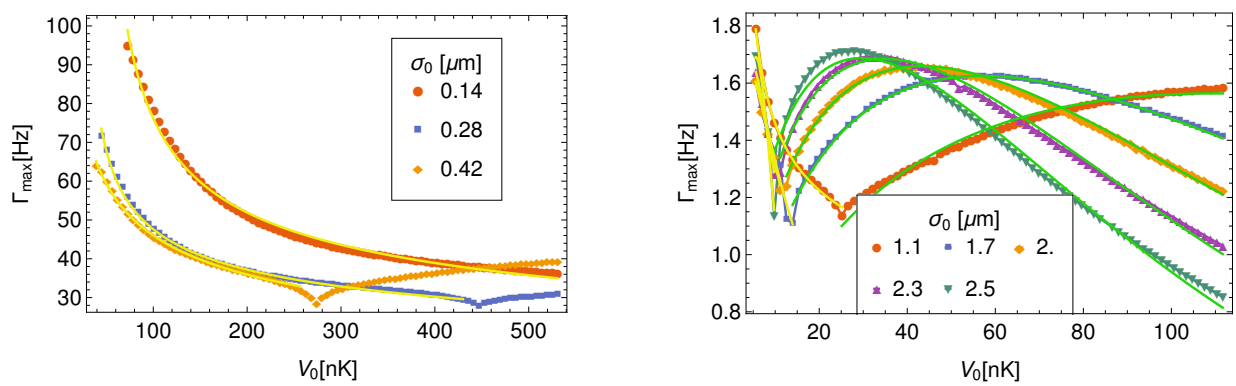

(a) (b)

Figure 7.5: *Scaling in barrier height for symmetric trap.* Maximal tunneling rate as a function of V_0 for different values of σ_0, with barrier separation for (a) $x_0 = 1.0[\mu\text{m}]$ and (b) $x_0 = 5.0[\mu\text{m}]$; solid yellow (green) curves are fits before (after) kink, emergence of effective mean-field islands. For smaller barrier width $x_0 = 1.0[\mu]$, scaling is dominated by the classical oscillation frequency. Error bars for data points are smaller than markers.

7.5 Scaling Results in Tilted Gaussian Traps

Tunneling rate trends as a function of mean-field strength, Figure 7.6(a), differ from the double-Gaussian configuration. Tunneling rates are not as narrowly peaked around $\Gamma_{\max}$, and steeper ramp slopes have lower cutoffs for maximal mean-field interactions. The appearance of mean-field islands is again visible in the formation of a cusp for $\alpha_0 \leq 2$. Similar to V_{sym}, we look at scaling in $\Gamma_{\max}$. Unlike V_{sym}, where the scaling in $\Gamma_{\max}$ could be easily attributed to either a large change in the classical oscillation period or the tunneling probability, changing any of the trap parameters results in a strong change in both the width of the trap and the

penetration barrier area.

Scaling in linear acceleration, α_0, for several barrier heights is given in Figure 7.6(b). Larger barriers allow for stronger accelerations, but have overall lower tunneling rates, barely reaching $\Gamma = 8$[Hz] for $V_0 = 125.6$[nK]. Experimentally, the control knob of choice would be barrier height, rather than acceleration in this configuration, having a more drastic effect on the tunneling rate. Before the appearance of the mean-field island, scaling is nearly linear,

$$\Gamma_{\max} \simeq a_0 + a_1\alpha_0. \tag{7.14}$$

Afterwards, the tunneling rate scales polynomially,

$$\Gamma_{\max} \simeq a_0 + a_2\alpha_0^2 + a_3\alpha_0^3, \tag{7.15}$$

the yellow fit lines in Figure 7.6(b).

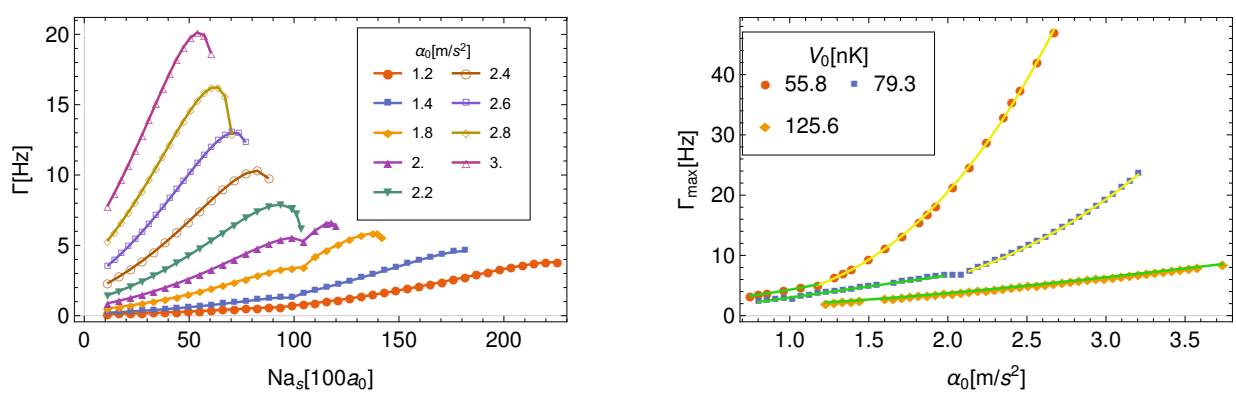

(a) (b)

Figure 7.6: *Scaling in ramp slope for tilt trap.* (a) Tunneling rate, Γ, is plotted as a function of interaction, in terms of effective scattering length a_s in units of Bohr radius a_0 and number of atoms N, for several tilt α_0, with $V_0 = 79.3$[nK] and $\omega_\perp = 2\pi \times 1000$[Hz]. Emergence of effective mean-field islands is apparent for $\alpha_0 = 2$ with appearance of a *kink*. Markers are data points and curves are a guide to the eye. (b) Maximal tunneling rate $\Gamma_{\max}$ as a function of α_0 for several barrier values. Fit curves are split with (solid green) and without (solid yellow) emergence of the effective mean-field islands. The largest barrier, $V_0 = 125.6$[nK], is sufficiently large to have mean-field islands for all plotted α_0. All data points have error bars smaller than markers.

Tunneling rate as a function of interaction strength, for various barrier heights, and for a fixed width Figure 7.7(a), have curves with trends similar to Figure 7.6(a). Larger barriers

have lower maximal tunneling rates but allow for larger mean-field interaction Ng. The appearance of mean-field island is, again, visible with a sudden change for $V_0 > 72.6$[nK], and after mean-field islands appear, increasing barrier height does not change the maximal tunneling rate as much. Scaling laws as a function of barrier height for the ramped Gaussian Figure 7.7(b), for the region before mean-field islands, yellow fit lines, trend as

$$\Gamma_{\max} \simeq a_0 + a_1 V_0 + a_2 V_0^2 + a_3 V_0^3, \tag{7.16}$$

and linearly for larger V_0, where mean-field islands are present, green fit lines.

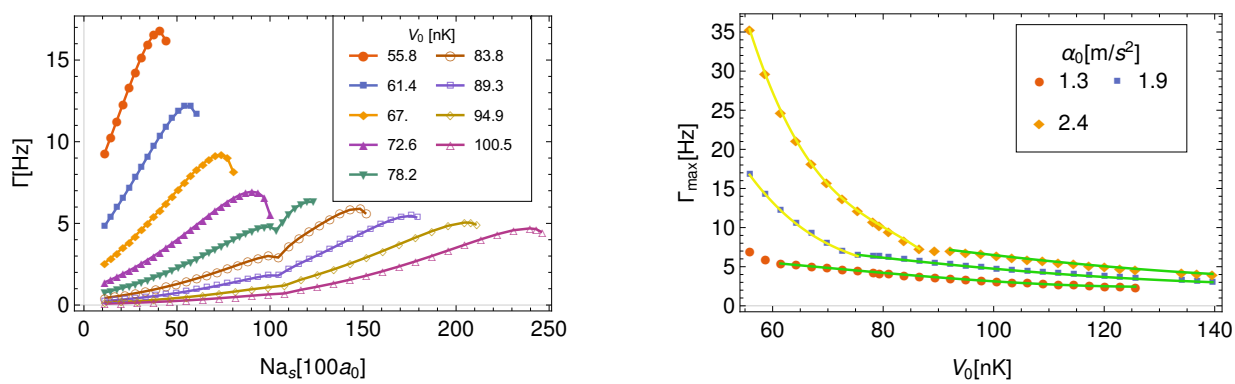

(a) (b)

Figure 7.7: *Scaling in barrier height for tilt trap.* (a) Tunneling rate, Γ, is plotted as a function of interaction, in terms of number of atoms N and effective scattering length a_s in units of Bohr radius a_0, for several barrier heights V_0, with $\alpha_0 = 1.87$[m/s^2] and $\omega_\perp = 2\pi \times 1000$[Hz]. A kink in Γ for $V_0 = 78.2$ marks the appearance of effective mean-field islands. Markers are data, while curves are a guide to the eye. (b) Maximal tunneling rate, $\Gamma_{\max}$, as a function of V_0 for various α_0 show clear trends before and after appearance of effective mean-field islands; fit curves are split before (solid yellow) and after (solid green) emergence of islands. All data points have error bars smaller than markers.

7.6 Experimental Implementation

For experimental realization, there are 4 conditions that must be met in the trap configurations.

1. The chemical potential must be below the transverse energy spacing.

In order to keep the transverse wavefunction its ground state, the chemical potential must be below transverse energy spacing, $\mu < \hbar\omega_\perp$. This ultimately gives an upper bound to the barrier heights $V_{\max} = \hbar\omega_\perp$; for transverse frequencies of up to $2\pi \times 1000$[Hz], this will give a maximal height around 50[nK]. V_{sym} with smaller widths, x_0, will require smaller Gaussian widths, and $\Gamma_{\max}$ scaling will be dominated by the classical oscillation period. Larger trap widths allow access to tunneling with and without mean-field islands Figure 7.4(b). For V_{tilt}, tight transverse confinement will lead to densities $n \geq \mathcal{O}(10^{-15}[\text{cm}^{-3}])$; Rubidium BEC's would be dominated by 3-body loss.

2. For meta-stable trapped states, the mean-field interaction Ng is bounded by the chemical potential.

   Since the chemical potential is bounded by the transverse energy, $\hbar\omega_\perp$, we can relate the mean-field interaction and transverse frequency, $gN < \mu < \hbar\omega_\perp$. Using the Thomas-Fermi approximation and infinite hard-wall approximations of V_{sym} and V_{titl}, one finds upper limits $Ng^{1D}_{\text{sym}} = 2\mu x_0$ and $Ng^{1D}_{\text{tilt}} = \frac{1}{2}\mu^2/\alpha_0$. These rough approximate limits turn out to be good upper bounds, since, compared to these analytical limits, our numerical values $Ng^{1D}_{\max}$ are typically 5 to 10% lower. Combining the hard-wall limits, $\mu < \hbar\omega_\perp$, and $g^{1D} = 2\hbar\omega_\perp a_s$, the total atom number and scattering lengths are bounded by $Na_s^{\text{sym}} < \frac{1}{4}\hbar\omega_\perp/\alpha_0$ and $Na_s^{\text{tilt}} < x_0$ This gives $N = \mathcal{O}(100 \text{ to } 1,000)$ in V_{sym} for rubidium, with tunneling times $1/\Gamma = 0.05$ to 2[s]. In V_{tilt}, scattering lengths will have to be altered to allow for $\mathcal{O}(1,000)$ atoms in the trap, $a_s \lesssim \mathcal{O}(10)[a_0]$.

3. BEC number density, n, must be sufficiently low.

   For a true quasi-1D GPE, the harmonic oscillator length, $\ell_\perp$ is bounded by the healing length, ξ, see Section. 2.3.6 for details. From this condition, the max density is found as $n_{\max} = (8\pi\ell_\perp^2 a_s)^{-1}$, which gives typical BEC densities, 10^{-12} to $10^{-15}[\text{cm}^{-3}]$, for the parameter ranges considered in this chapter. Above 10^{-15}[cm], 3-body loss mechanics

dominate beyond sub-second tunneling times.

4. Tunneling time, $1/\Gamma$, must be sufficiently small.

   Sufficiently fast tunneling rates, one of the main limitations to observe MQT, are required so that 3-body loss do not dominate the dynamics. Throughout the trap parameter space, we find tunneling times, $1/\Gamma$, from 0.01 to 2 seconds, which are accessible in BEC experiments. These tunneling times, and all figures in this chapter, are for rubidium atoms, which are almost 4 times heavier than sodium and more than 12 times heavier than lithium, two common atoms used in BEC experiments. Rubidium atoms are often preferred because the 3-body loss rate is two orders of magnitude smaller than for sodium and lithium atoms [155].

For different species of atoms, rubidium, lithium, and sodium, all quantities in the paper are rescalable. Given length scale L and a non-dimensionalized quantity, such as $\tilde{\mu}$, then $\mu^{\mathrm{Li}} = \frac{\hbar^2}{m^{\mathrm{Li}}L^2}\tilde{\mu} = \frac{m^{\mathrm{Rb}}}{m^{\mathrm{Li}}}\mu^{\mathrm{Rb}}$. These gain values of $m^{\mathrm{Rb}}/m^{\mathrm{Li}} \approx 12.5$ and $m^{\mathrm{Rb}}/m^{\mathrm{Na}} \approx 3.8$; larger traps, interactions strengths, and tunneling rates. Similarly, maximal densities scale as $n^{\mathrm{Li}}_{\mathrm{max}} = \frac{m^{\mathrm{Li}}}{m^{\mathrm{Rb}}}n^{\mathrm{Rb}}_{\mathrm{max}}$. For typical Rubidium BEC's , $n^{\mathrm{Rb}}_{\mathrm{max}} = 10^{-12}$ to $10^{-15}[\mathrm{cm}^{-3}]$, and thus $n^{\mathrm{Li}}_{\mathrm{max}} = 10^{-11}$ to $10^{-14}[\mathrm{cm}^{-3}]$, giving BEC's that can last upwards of 1 second.

Rescaling Γ can be subtle, depending on the question being asked. The simplest method is, if we rescale all trap and wave function parameters, then we simply get $\Gamma^{\mathrm{Li}} = \frac{m^{\mathrm{Rb}}}{m^{\mathrm{Li}}}\Gamma^{\mathrm{Rb}}$. On the other hand, if given a specific set of trap and wave function parameters, we simply swap out the atoms, then tunneling rates scale as $\Gamma^{\mathrm{Li}} = \Gamma^{\mathrm{Rb}}\sqrt{m^{\mathrm{Rb}}/m^{\mathrm{Li}}}P_{\mathrm{Tunn}}^{\sqrt{m^{\mathrm{Li}}/m^{\mathrm{Rb}}}-1}$. Typical tunneling probabilities of $P_{\mathrm{Tunn}} = 0.05$ to 0.10 give $\Gamma^{\mathrm{Li}} \approx (10 \text{ to } 20)\Gamma^{\mathrm{Rb}}$.

7.7 Additional Considerations: Effective Multiple Wells and Additional Ansätze

There are instances where the effective mean-field barrier energy inside the trap becomes higher than the chemical potential, creating multiple effective wells inside the barrier, Figure 7.8. Tunneling probability through these effective islands is symmetric, left-to-right or right-to-left, and is generally an order of magnitude larger than the outermost trapping bar-

rier(s). We modify the classical oscillation period to be the sum of all oscillation periods, T_i, in the wells,

$$\Gamma = \left(\sum_i T_i\right)^{-1} \exp\left(-\frac{2}{\hbar}\int_{x_1}^{x_2} \mathrm{dx}|p(x)|\right), \tag{7.17}$$

accounting for addition oscillations in the well.

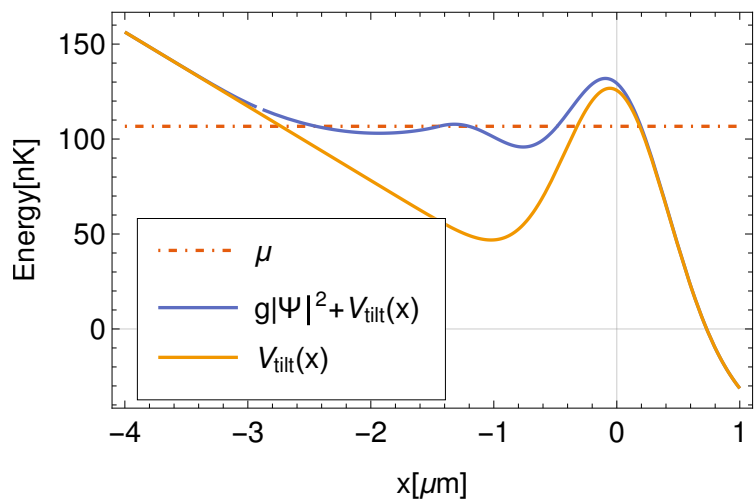

Figure 7.8: *Effective potential produces extra barrier.* The effective potential, $g|\Psi|^2 + V_{\text{tilt}}(x)$ (solid blue line), contains a small *island* region, located around $x \approx -1.5$, which goes slightly above the chemical potential, μ (dash-dotted red line); the bare potential $V_{\text{tilt}}(x)$ (solid yellow line) is shown for comparison. Potential parameters are $V_0 = 125.6$[nK], $\sigma_0 = 0.85[\mu\text{m}]$, and $\alpha_0 = 3.74[\text{m/s}^2]$. The symmetric potential, not shown, produces two islands.

Generally, for larger Ng, and larger traps, widths, and barrier heights, this modified tunneling rate appears cusps or kinks in the scaling plots. Once islands appear for some interaction strength, g', they will persist for all $g > g'$. Similar to water waves swelling near a shore, these mean-field islands are from the wave function self-interaction, $g|\Psi(s)|^2$, overlapping the trapping barrier, $V(x)$, in Eq. (7.6). For V_{sym}, both Gaussian barriers cause islands, while in V_{tilt} they are caused by the left-hand portion of the barrier, a combination of the Linear ramp and Gaussian tail of the barrier. For V_{tilt}, once islands appear for α', islands will persist for smaller, $\alpha_0 < \alpha'$. All scaling laws with mean-field islands have green lines, while those without mean-field islands are yellow, the only exception being Figure 7.4, where the region with mean-islands was sufficiently small that the fit curve covered the whole

range.

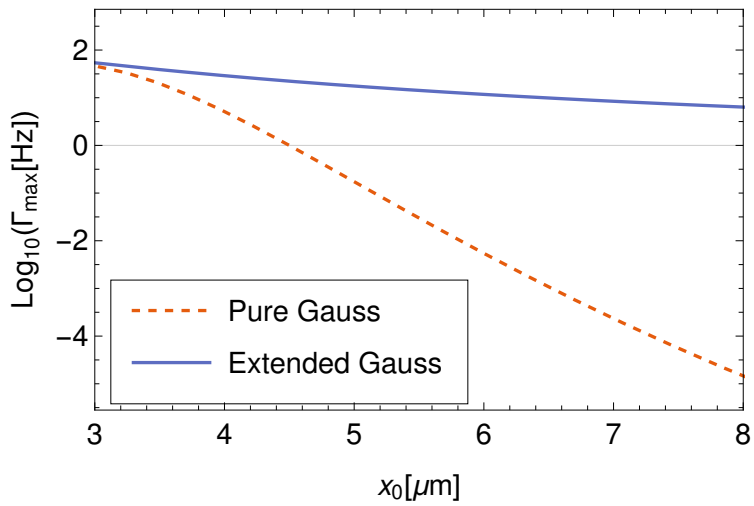

Figure 7.9: *Commonly used pure Gaussian variational ansatz severely underestimates tunneling rate.* Tunneling rate as a function of barrier separation, x_0, is plotted for a pure Gaussian (dashed red) and Gaussian with a flat middle region, extended Gaussian Eq. (7.9) (solid blue), in V_{sym} with parameters $V_0 = 79.8$[nK] and $\sigma_0 = 2.12[\mu\text{m}]$. The tunneling rates are almost equal for smaller separation, where the extended Gaussian approximates the pure Gaussian.

While the typical wave function variational ansatz is a pure Gaussian [156, 157], the results in this chapter used a linear function to connect Gaussian tails, allowing the wave function to extend into the Thomas-Fermi regime with larger and wider traps. The tunneling rates for a typical "pure" Gaussian and our "extended" Gaussian, Figure 7.9, are close for smaller traps. For wider traps, a pure Gaussian predicts a tunneling rate several order of magnitude lower, because it fails to account for the Thomas-Fermi flattening of the wave function.

Beyond using a linear function to allow the Gaussian ansatz to approximate the Thomas-Fermi solution, we also explored ansätze that modified the wave function tails. Using the fact that wave functions in square barriers have exponential tails, while harmonic barriers yield Gaussian tails, we explored an ansatz with the superposition of a Gaussian and exponential tail in the symmetric potential. We used two approaches, one with a "connecting function" to smooth the wave function derivative, and one without, where the derivative was allowed to be

discontinuous. With the connection functions, tunneling rates did not change significantly, while introducing a lot of additional variational parameter calculations. When the Gaussian-Exponential tail had no connecting function, the first derivative was discontinuous, and tunneling rates resulted in one to two orders of magnitude smaller than the simple Gaussian tail ansatz, due to a 20% reduction in the maximal mean-field interaction and around a 5% drop in the chemical potential and tunneling probability.

7.8 Conclusions

In this chapter we quantify the parameter space for two meta-stable traps which are suitable for studying macroscopic quantum tunneling in Bose-Einstein condensates described by the Gross-Pitaevskii equation; we find experimentally accessible tunneling rates and interaction strengths. The two traps are: a linearly ramped Gaussian barrier, and two offset Gaussian barriers. For rapid parameter space exploration, we use a variational-JWKB approach to approximate the ground states and calculate the tunneling rates, modifying the process to account for the nonlinearity in the GPE. The ansatz for the variational search is two Gaussian tails separated by a linear function, allowing the ansatz to accommodate narrow traps with Gaussian solutions, and wide traps with Thomas-Fermi solutions. We explicitly find scaling laws for tunneling rates with respects to relevant trap parameters, such as the barrier heights and trap widths. We can demonstrate when tunneling rate scaling is dominated by the oscillation period in the well or the tunneling probability through the barriers. We find that in certain parameter ranges, additional barriers, *islands*, due to mean-field effects, emerge inside the traps. This results in different scaling with a wide range of functional dependence on trap parameters: linear, polynomial, rational functions, square roots, and exponential. Between the two traps, we quantify a wide range of possible tunneling parameters for rubidium BECs: tunneling rates $O(0.1 \text{ to } 100[\text{Hz}])$, trapping well sizes $O(0.1 \text{ to } 7[\mu\text{m}])$, s-wave scattering lengths of 1 to 100 Bohr radii, and BEC densities of $O(10^{-12} \text{ to } 10^{-15}[\text{cm}^{-3}])$. Furthermore, we demonstrate how these parameters can be rescaled for sodium and lithium, i.e., lithium with reduced scattering length is a good

candidate in the ramped Gaussian potential.

CHAPTER 8

DISCUSSION, CONCLUSIONS, AND OPEN QUESTIONS

In this thesis, we started with the experimental findings of our collaborators, the research group lead by Aephraim M. Steinberg at the University of Toronto, the first realization of non-exponential tunneling decay of a Bose-Einstein condensate due to repulsive mean-field interactions in Chapter 3. Treating the tunneling as quasi-1D, we found we were able to corroborate the participation of mean-field interactions in the dynamics. We used a modified JWKB model with a simplified potential and found that the mean-field interactions were *required* to produce the measured non-exponential decay. This mean-field manifested as a dynamic barrier height which decreased as the number of trapped atoms decreased. An effective 1D model accurately reproduced and reinforced the findings of 3D Bose-Einstein condensate dynamics. The ability of effective mean-field models to simplify and capture gross features of nonlinear systems is well known in nonlinear optics. We asked if the mean-field models could be capturing and compensating for many-body effects. To answer this question, we pursued a simplified version of the experiment. Using the Bose-Hubbard Hamiltonian, we simulated a weakly interacting meta-stable state tunneling into free space through a barrier with many-body effects through depletion and fragmentation. Using the discrete nonlinear Schrodinger equation, we showed how a straight-forward mean-field treatment over-estimated the decay of the meta-stable state but was reproducible with a renormalized scalar mean-field.

Next, we set out to understand the tunneling dynamics of the Bose-Hubbard Hamiltonian in the superfluid quantum phase, with both repulsive and attractive interactions, in Chapter 4. We were able to show the many-body decay process converged to the mean-field with increasing number of atoms. We found that repulsive interactions initially increased tunneling rates, while attractive interactions reduced tunneling rates; intuitively, attractive

atoms in a trap tended to hold onto each other, while repulsive interactions would push other atoms out. Quantifying the time-scales vs interaction gave further insight into the rich many-body dynamics. Even tunneling times, a mean-field or semi-classical observable, deviated from simple exponential scaling for stronger interactions, requiring a polynomial in the exponent. Number fluctuations and entropy, many-body observables, had different functional time scales. We were able to show that many-body effects in number fluctuations and correlations are observable in macroscopic quantum tunneling.

After showing the many-body signatures in macroscopic quantum tunneling for superfluid dominated interactions, we then turned our focus to understanding how the superfluid-Mott quantum phase transition in the Bose-Hubbard Hamiltonian altered escape dynamics in Chapter 5. The superfluid state is gapless with global phase coherence and atoms maximally delocalized across the lattice. The Mott insulator is gapped and breaks global phase symmetry, with atoms localized onto single sites. We found that the ground state quantum phase strongly altered dynamics. Qualitatively, the superfluid regime dynamics were wave-like, with interference patters in the escaped atoms and tunneling rates were fast. Mott regime dynamics were particle-like, and tunneling was slow due to the Mott gap, despite having much larger repulsive interactions. And near the critical point, the system demonstrated a mix of wave and particle-like features. Many-body observables showed distinct imprints of their quantum phase. Fluctuations in the trap monotonically decreased in the superfluid regime. In the Mott regime, fluctuations increased, maximized, and then decreased. Entropy maximized when around half of the atoms had escaped in the superfluid regime, while maximizing when around one-quarter had escaped in the Mott regime. Two-point number correlations showed pulsed regions of positive correlations in escaped atoms. In addition, we contributed to a project studying the Superfluid-Mott and Josephson-Fock phase transitions in a double well in Section 6.1. We were able to demonstrate the coherent wave nature of the superfluid in both the Josephson oscillation and self-trapped Fock states and the Mott insulator induced robust particle-hole excitations. Furthermore, we showed how the mean-field

failed to capture the large fluctuations and strong correlations of the Mott regime.

Finally, in Chapter 7, we explored future realizations of macroscopic quantum tunneling in Bose-Einstein condensates. As experimental techniques increase in sophistication and precision, the quantum fluctuations and correlations we quantified will become observable. To this end, we examined two trapping potentials that are readily accessible in the lab. First, two offset Gaussian barriers in a symmetric configuration. Second, a Gaussian barrier with a linear acceleration. Rather than full many-body simulations, we focused on understanding the gross features of tunneling, understanding the accessible time scales in these two potentials. For rapid parameter space exploration of the two potentials, we used a modified variational-JWKB approach to estimate tunneling times for Bose-Einstein condensates described by the Gross-Pitaevskii equation. In order to maximize the explorable parameter space, we used a modified Gaussian ansatz which could interpolate between pure Gaussian and extended Thomas-Fermi solutions in narrow and wide traps. In this analysis, we found the appearance of mean-field islands, regions inside the trap where the mean-field effective barrier rose above the chemical potential, observable as alterations of the tunneling rates. We found accessible time scales from 10 to 0.1 seconds for rubidium, lithium, and sodium Bose-Einstein condensates. Furthermore, we fully analyzed the experimental limitations on the chemical potential, mean-field energy, and density, providing bounds on accessible ranges, such as, finding that lithium and sodium required lower densities and scattering lengths, and thus were better suited to the ramped Gaussian potential than the double Gaussian. We quantified all possible configurations for macroscopic tunneling in both traps, fitting scaling laws to all trap parameters, clearly indicating accessible density, atom number, and time scales.

And thus, we come full circle in this thesis, from experimental results in Bose-Einstein condensates, to showing how many-body physics could be hidden in mean-field systems, to fully quantifying the macroscopic quantum tunneling dynamics of bosons in a superfluid, showing how the superfluid-Mott quantum phase transition is visible in tunneling dynamics,

and then finishing with possible road maps to future experimental realizations. Thanks to the amazing work with fantastic collaborators from the universities of Toronto, Peking, Heidelberg, and fellow researchers at Colorado School of Mines, we have a more thorough understanding of many-body quantum tunneling. Furthermore, we have opened new avenues of research and future study. There are many fruitful questions open amongst the various projects. Explicitly, what precision in experiments are required to differentiate between effective mean-field and macroscopic many-body dynamics? What happens to superfluid-dominated tunneling for a more slowly, or adiabatically, dropped barrier, rather than a sudden reduction? What if we used different initial trapping barriers such as a harmonic or linear barrier, or different tunneling barriers, such as triangle or Gaussian barriers? By using different trapping wells sizes, how does the density of trapped atoms modify tunneling? How does the superfluid-Mott escape system differ for far-from commensurate filling in the trap? And, using a finer grain interaction parameter range, what happens to tunneling around the critical point in the superfluid-Mott transition?

There are still many systems left unexplored with quantum tunneling: open quantum systems, with the addition of loss and noise; studying quasi-particle tunneling, and the breakdown of quasi-particles at stronger interactions; analyzing multi-component Bose-Einstein condensates; or the addition of disorder to the system. Quantum tunneling propelled quantum mechanics into the forefront of physics in the last century. The first steps taken in this thesis to understand the interplay between quantum phase transitions and tunneling dynamics strongly indicates the accessibility of controlling and guiding entangled matter in future technologies, such as atomtronics. The control of emissions of atoms with tuned interactions and barriers has the potential to produce pulsed and continuous-wave atom lasers with positive correlations.

REFERENCES CITED

[1] R. Kanamoto L. D. Carr and M. Ueda. *Understanding Quantum Phase Transitions*. Taylor & Francis, 2010. URL https://www.crcpress.com/Understanding-Quantum-Phase-Transitions/Carr/p/book/9781439802519.

[2] Subir Sachdev. Quantum phase transitions. *Handbook of Magnetism and Advanced Magnetic Materials*, 2007.

[3] Eugen Merzbacher. The Early History of Quantum Tunneling. *Physics Today*, 55 (8):44–49, August 2002. ISSN 0031-9228. doi: 10.1063/1.1510281. URL http://physicstoday.scitation.org/doi/full/10.1063/1.1510281.

[4] F. Hund. Zur deutung der molekelspektren. i. 40(10):742–764, . ISSN 0044-3328. doi: 10.1007/BF01400234. URL https://doi.org/10.1007/BF01400234.

[5] F. Hund. Zur deutung der molekelspektren. II. 42(2):93–120, . ISSN 0044-3328. doi: 10.1007/BF01397124. URL https://doi.org/10.1007/BF01397124.

[6] F. Hund. Zur deutung der molekelspektren. III. 43(11):805–826, . ISSN 0044-3328. doi: 10.1007/BF01397249. URL https://doi.org/10.1007/BF01397249.

[7] K. Kuwahata, T. Hama, A. Kouchi, and N. Watanabe. Signatures of Quantum-Tunneling Diffusion of Hydrogen Atoms on Water Ice at 10 K. *Physical Review Letters*, 115(13):133201, September 2015. doi: 10.1103/PhysRevLett.115.133201. URL https://link.aps.org/doi/10.1103/PhysRevLett.115.133201.

[8] M. Minissale, E. Congiu, S. Baouche, H. Chaabouni, A. Moudens, F. Dulieu, M. Accolla, S. Cazaux, G. Manic, and V. Pirronello. Quantum Tunneling of Oxygen Atoms on Very Cold Surfaces. *Physical Review Letters*, 111(5):053201, July 2013. doi: 10.1103/PhysRevLett.111.053201. URL https://link.aps.org/doi/10.1103/PhysRevLett.111.053201.

[9] Peter S. Zuev, Robert S. Sheridan, Titus V. Albu, Donald G. Truhlar, David A. Hrovat, and Weston Thatcher Borden. Carbon Tunneling from a Single Quantum State. *Science*, 299(5608):867–870, February 2003. ISSN 0036-8075, 1095-9203. doi: 10.1126/science.1079294. URL http://science.sciencemag.org/content/299/5608/867.

[10] Nagel, Zachary D. and Klinman, Judith P. Tunneling and Dynamics in Enzymatic Hydride Transfer. *Chemical Reviews*, 106(8):3095–3118, August 2006. doi: 10.1021/cr050301x. URL https://pubs.acs.org/doi/abs/10.1021/cr050301x.

[11] Ollie M. Gonzalez-James, Xue Zhang, Ayan Datta, David A. Hrovat, Weston Thatcher Borden, and Daniel A. Singleton. Experimental Evidence for Heavy-Atom Tunneling in the Ring-Opening of Cyclopropylcarbinyl Radical from Intramolecular 12c/13c Kinetic Isotope Effects. *Journal of the American Chemical Society*, 132(36):12548–12549, September 2010. ISSN 0002-7863. doi: 10.1021/ja1055593. URL https://doi.org/10.1021/ja1055593.

[12] David Ley, Dennis Gerbig, and Peter R. Schreiner. Tunnelling control of chemical reactions the organic chemist's perspective. *Organic & Biomolecular Chemistry*, 10 (19):3781, 2012. ISSN 1477-0520, 1477-0539. doi: 10.1039/c2ob07170c. URL http://xlink.rsc.org/?DOI=c2ob07170c.

[13] Xinxin Zhao, Diego A. Alcala, Marie A. McLain, Kenji Maeda, Shreyas Potnis, Ramon Ramos, Aephraim M. Steinberg, and Lincoln D. Carr. Macroscopic quantum tunneling escape of Bose-Einstein condensates. *Physical Review A*, 96(6):063601, December 2017. doi: 10.1103/PhysRevA.96.063601. URL https://link.aps.org/doi/10.1103/PhysRevA.96.063601.

[14] Shin Takagi. *Macroscopic Quantum Tunneling*. Cambridge University Press;, 2002.

[15] Eric Akkermans and Gilles Montambaux. *Mesoscopic Physics of Electrons and Photons*. Cambridge University Press, 2011.

[16] G. Zürn, A. N. Wenz, S. Murmann, A. Bergschneider, T. Lompe, and S. Jochim. Pairing in few-fermion systems with attractive interactions. *Phys. Rev. Lett.*, 111: 175302, Oct 2013. doi: 10.1103/PhysRevLett.111.175302. URL http://link.aps.org/doi/10.1103/PhysRevLett.111.175302.

[17] A. del Campo, F. Delgado, G. García-Calderón, J. G. Muga, and M. G. Raizen. Decay by tunneling of bosonic and fermionic tonks-girardeau gases. *Phys. Rev. A*, 74:013605, Jul 2006. doi: 10.1103/PhysRevA.74.013605. URL http://link.aps.org/doi/10.1103/PhysRevA.74.013605.

[18] John M. Martinis, M. Ansmann, and J. Aumentado. Energy decay in superconducting josephson-junction qubits from nonequilibrium quasiparticle excitations. *Phys. Rev. Lett.*, 103:097002, Aug 2009. doi: 10.1103/PhysRevLett.103.097002. URL http://link.aps.org/doi/10.1103/PhysRevLett.103.097002.

[19] G. Catelani, S. E. Nigg, S. M. Girvin, R. J. Schoelkopf, and L. I. Glazman. Decoherence of superconducting qubits caused by quasiparticle tunneling. *Phys. Rev. B*, 86:184514, Nov 2012. doi: 10.1103/PhysRevB.86.184514. URL `http://link.aps.org/doi/10.1103/PhysRevB.86.184514`.

[20] I. A. Shelykh, D. D. Solnyshkov, G. Pavlovic, and G. Malpuech. Josephson effects in condensates of excitons and exciton polaritons. *Phys. Rev. B*, 78:041302, Jul 2008. doi: 10.1103/PhysRevB.78.041302. URL `http://link.aps.org/doi/10.1103/PhysRevB.78.041302`.

[21] Olaf Nairz, Markus Arndt, and Anton Zeilinger. Quantum interference experiments with large molecules. *American Journal of Physics*, 71(4):319–325, 2003. doi: 10.1119/1.1531580. URL `https://doi.org/10.1119/1.1531580`.

[22] M. Abbarchi, A. Amo, V. G. Sala, D. D. Solnyshkov, H. Flayac, L. Ferrier, I. Sagnes, E. Galopin, A. Lemaitre, G. Malpuech, and J. Bloch. Macroscopic quantum self-trapping and josephson oscillations of exciton polaritons. *Nature Physics*, 9:275–279, May 2013. doi: 10.1038/nphys2609. URL `http://dx.doi.org/10.1038/nphys2609`.

[23] Chaohong Lee, Wenhua Hai, Xueli Luo, Lei Shi, and Kelin Gao. Quasispin model for macroscopic quantum tunneling between two coupled bose-einstein condensates. *Phys. Rev. A*, 68:053614, Nov 2003. doi: 10.1103/PhysRevA.68.053614. URL `http://link.aps.org/doi/10.1103/PhysRevA.68.053614`.

[24] S. Raghavan, A. Smerzi, S. Fantoni, and S. R. Shenoy. Coherent oscillations between two weakly coupled bose-einstein condensates: Josephson effects, π oscillations, and macroscopic quantum self-trapping. *Phys. Rev. A*, 59:620–633, Jan 1999. doi: 10.1103/PhysRevA.59.620. URL `http://link.aps.org/doi/10.1103/PhysRevA.59.620`.

[25] Michael Albiez, Rudolf Gati, Jonas Flling, Stefan Hunsmann, Matteo Cristiani, and Markus K. Oberthaler. Direct Observation of Tunneling and Nonlinear Self-Trapping in a Single Bosonic Josephson Junction. *Physical Review Letters*, 95(1):010402, June 2005. doi: 10.1103/PhysRevLett.95.010402. URL `http://link.aps.org/doi/10.1103/PhysRevLett.95.010402`.

[26] I. Shomroni S. Levy, E. Lahoud and J. Steinhauer. The a.c. and d.c. josephson effects in a Boseeinstein condensate. *Nature*, 449:579–583, 2007.

[27] R. Lundmark, C. Forssén, and J. Rotureau. Tunneling theory for tunable open quantum systems of ultracold atoms in one-dimensional traps. *Phys. Rev. A*, 91:041601, Apr 2015. doi: 10.1103/PhysRevA.91.041601. URL `https://link.aps.org/doi/10.1103/PhysRevA.91.041601`.

[28] Seyed Ebrahim Gharashi and D. Blume. Tunneling dynamics of two interacting one-dimensional particles. *Phys. Rev. A*, 92:033629, Sep 2015. doi: 10.1103/PhysRevA.92.033629. URL https://link.aps.org/doi/10.1103/PhysRevA.92.033629.

[29] G. Zürn, F. Serwane, T. Lompe, A. N. Wenz, M. G. Ries, J. E. Bohn, and S. Jochim. Fermionization of two distinguishable fermions. *Phys. Rev. Lett.*, 108:075303, Feb 2012. doi: 10.1103/PhysRevLett.108.075303. URL https://link.aps.org/doi/10.1103/PhysRevLett.108.075303.

[30] Massimo Rontani. Tunneling theory of two interacting atoms in a trap. *Phys. Rev. Lett.*, 108:115302, Mar 2012. doi: 10.1103/PhysRevLett.108.115302. URL https://link.aps.org/doi/10.1103/PhysRevLett.108.115302.

[31] Masahito Ueda and Anthony J. Leggett. Macroscopic quantum tunneling of a bose-einstein condensate with attractive interaction. *Phys. Rev. Lett.*, 80:1576–1579, Feb 1998. doi: 10.1103/PhysRevLett.80.1576. URL http://link.aps.org/doi/10.1103/PhysRevLett.80.1576.

[32] L. Salasnich, A. Parola, and L. Reatto. Pulsed macroscopic quantum tunneling of falling bose-einstein condensates. *Phys. Rev. A*, 64:023601, Jun 2001. doi: 10.1103/PhysRevA.64.023601. URL http://link.aps.org/doi/10.1103/PhysRevA.64.023601.

[33] L D Carr, M J Holland, and B A Malomed. Macroscopic quantum tunnelling of boseeinstein condensates in a finite potential well. *Journal of Physics B: Atomic, Molecular and Optical Physics*, 38(17):3217, 2005. URL http://stacks.iop.org/0953-4075/38/i=17/a=012.

[34] Alexej I. Streltsov, Ofir E. Alon, and Lorenz S. Cederbaum. Formation and dynamics of many-boson fragmented states in one-dimensional attractive ultracold gases. *Phys. Rev. Lett.*, 100:130401, Apr 2008. doi: 10.1103/PhysRevLett.100.130401. URL http://link.aps.org/doi/10.1103/PhysRevLett.100.130401.

[35] Axel U. J. Lode, Alexej I. Streltsov, Kaspar Sakmann, Ofir E. Alon, and Lorenz S. Cederbaum. How an interacting many-body system tunnels through a potential barrier to open space. *Proceedings of the National Academy of Sciences of the United States of America*, 109(34):13521–13525, 2012. ISSN 00278424. URL http://www.jstor.org/stable/41700964.

[36] Diego A. Alcala, Joseph A. Glick, and Lincoln D. Carr. Entangled Dynamics in Macroscopic Quantum Tunneling of Bose-Einstein Condensates. *Physical Review Letters*, 118(21):210403, May 2017. doi: 10.1103/PhysRevLett.118.210403. URL https://link.aps.org/doi/10.1103/PhysRevLett.118.210403.

[37] M. Girardeau. Relationship between systems of impenetrable bosons and fermions in one dimension. *Journal of Mathematical Physics*, 1(516):516–523, 1960. doi: http://dx.doi.org/10.1063/1.1703687. URL `http://scitation.aip.org/content/aip/journal/jmp/1/6/10.1063/1.1703687`.

[38] C. E. Creffield, F. Sols, D. Ciampini, O. Morsch, and E. Arimondo. Expansion of matter waves in static and driven periodic potentials. *Phys. Rev. A*, 82:035601, Sep 2010. doi: 10.1103/PhysRevA.82.035601. URL `http://link.aps.org/doi/10.1103/PhysRevA.82.035601`.

[39] T. A. Pasquini, M. Saba, G.-B. Jo, Y. Shin, W. Ketterle, D. E. Pritchard, T. A. Savas, and N. Mulders. Low velocity quantum reflection of bose-einstein condensates. *Phys. Rev. Lett.*, 97:093201, Aug 2006. doi: 10.1103/PhysRevLett.97.093201. URL `http://link.aps.org/doi/10.1103/PhysRevLett.97.093201`.

[40] O. Zobay and B. M. Garraway. Two-dimensional atom trapping in field-induced adiabatic potentials. *Phys. Rev. Lett.*, 86:1195–1198, Feb 2001. doi: 10.1103/PhysRevLett.86.1195. URL `http://link.aps.org/doi/10.1103/PhysRevLett.86.1195`.

[41] Martin Shotter, Dimitrios Trypogeorgos, and Christopher Foot. Enhancement of on-site interactions of tunneling ultracold atoms in optical potentials using radio-frequency dressing. *Phys. Rev. A*, 78:051602, Nov 2008. doi: 10.1103/PhysRevA.78.051602. URL `http://link.aps.org/doi/10.1103/PhysRevA.78.051602`.

[42] M Heimsoth, D Hochstuhl, C E Creffield, L D Carr, and F Sols. Effective josephson dynamics in resonantly driven boseeinstein condensates. *New Journal of Physics*, 15 (10):103006, 2013. URL `http://stacks.iop.org/1367-2630/15/i=10/a=103006`.

[43] Marc Andrew Valdez, Gavriil Schedrin, Martin Heimoth, Charles E. Creffield, Fernando Sols, and Lincoln D. Carr. Many-body Quantum Chaos and Entanglement in a Quantum Ratchet. *Phys. Rev. Lett. under review*, 2016.

[44] H. Lignier, C. Sias, D. Ciampini, Y. Singh, A. Zenesini, O. Morsch, and E. Arimondo. Dynamical control of matter-wave tunneling in periodic potentials. *Phys. Rev. Lett.*, 99:220403, Nov 2007. doi: 10.1103/PhysRevLett.99.220403. URL `http://link.aps.org/doi/10.1103/PhysRevLett.99.220403`.

[45] C. E. Creffield. Quantum control and entanglement using periodic driving fields. *Phys. Rev. Lett.*, 99:110501, Sep 2007. doi: 10.1103/PhysRevLett.99.110501. URL `http://link.aps.org/doi/10.1103/PhysRevLett.99.110501`.

[46] C. Sias, H. Lignier, Y. P. Singh, A. Zenesini, D. Ciampini, O. Morsch, and E. Arimondo. Observation of photon-assisted tunneling in optical lattices. *Phys. Rev. Lett.*, 100: 040404, Feb 2008. doi: 10.1103/PhysRevLett.100.040404. URL `http://link.aps.org/doi/10.1103/PhysRevLett.100.040404`.

[47] Gastón García-Calderón and Roberto Romo. Nonexponential tunneling decay of a single ultracold atom. *Phys. Rev. A*, 93:022118, Feb 2016. doi: 10.1103/PhysRevA.93.022118. URL `https://link.aps.org/doi/10.1103/PhysRevA.93.022118`.

[48] Nancy Makri and William H. Miller. A semiclassical tunneling model for use in classical trajectory simulations. *The Journal of Chemical Physics*, 91(7):4026–4036, October 1989. ISSN 0021-9606. doi: 10.1063/1.456833. URL `http://aip.scitation.org/doi/10.1063/1.456833`.

[49] Kevin A. Mitchell and Daniel A. Steck. Fractal templates in the escape dynamics of trapped ultracold atoms. *Phys. Rev. A*, 76:031403, Sep 2007. doi: 10.1103/PhysRevA.76.031403. URL `http://link.aps.org/doi/10.1103/PhysRevA.76.031403`.

[50] Daniel A. Steck, Windell H. Oskay, and Mark G. Raizen. Fluctuations and decoherence in chaos-assisted tunneling. *Phys. Rev. Lett.*, 88:120406, Mar 2002. doi: 10.1103/PhysRevLett.88.120406. URL `http://link.aps.org/doi/10.1103/PhysRevLett.88.120406`.

[51] A. Mouchet, C. Miniatura, R. Kaiser, B. Grémaud, and D. Delande. Chaos-assisted tunneling with cold atoms. *Phys. Rev. E*, 64:016221, Jun 2001. doi: 10.1103/PhysRevE.64.016221. URL `http://link.aps.org/doi/10.1103/PhysRevE.64.016221`.

[52] Steven Tomsovic and Denis Ullmo. Chaos-assisted tunneling. *Phys. Rev. E*, 50:145–162, Jul 1994. doi: 10.1103/PhysRevE.50.145. URL `http://link.aps.org/doi/10.1103/PhysRevE.50.145`.

[53] A. M. Kaufman, B. J. Lester, C. M. Reynolds, M. L. Wall, M. Foss-Feig, K. R. A. Hazzard, A. M. Rey, and C. A. Regal. Two-particle quantum interference in tunnel-coupled optical tweezers. *Science*, 345(6194):306–309, 2014. ISSN 0036-8075. doi: 10.1126/science.1250057. URL `http://science.sciencemag.org/content/345/6194/306`.

[54] Ehud Altman, Kenneth R Brown, Giuseppe Carleo, Lincoln D Carr, Eugene Demler, Cheng Chin, Brian DeMarco, Sophia E Economou, Mark Eriksson, Kai-Mei C Fu, et al. Quantum simulators: Architectures and opportunities. *arXiv preprint arXiv:1912.06938*, 2019.

[55] M. Greiner, C. A. Regal, J. T. Stewart, and D. S. Jin. Probing Pair-Correlated Fermionic Atoms through Correlations in Atom Shot Noise. *Physical Review Letters*, 94(11):110401, March 2005. doi: 10.1103/PhysRevLett.94.110401. URL `http://link.aps.org/doi/10.1103/PhysRevLett.94.110401`.

[56] M. H. Anderson, J. R. Ensher, M. R. Matthews, C. E. Wieman, and E. A. Cornell. Observation of bose-einstein condensation in a dilute atomic vapor. 269(5221):198–201. ISSN 0036-8075, 1095-9203. doi: 10.1126/science.269.5221.198. URL `http://science.sciencemag.org/content/269/5221/198`.

[57] K. B. Davis, M. O. Mewes, M. R. Andrews, N. J. van Druten, D. S. Durfee, D. M. Kurn, and W. Ketterle. Bose-einstein condensation in a gas of sodium atoms. 75(22): 3969–3973. doi: 10.1103/PhysRevLett.75.3969. URL `https://link.aps.org/doi/10.1103/PhysRevLett.75.3969`.

[58] C. C. Bradley, C. A. Sackett, and R. G. Hulet. Bose-einstein condensation of lithium: Observation of limited condensate number. *Phys. Rev. Lett.*, 78:985–989, Feb 1997. doi: 10.1103/PhysRevLett.78.985. URL `https://link.aps.org/doi/10.1103/PhysRevLett.78.985`.

[59] Thomas Schweigler, Valentin Kasper, Sebastian Erne, Igor Mazets, Bernhard Rauer, Federica Cataldini, Tim Langen, Thomas Gasenzer, Jrgen Berges, and Jrg Schmiedmayer. Experimental characterization of a quantum many-body system via higher-order correlations. *Nature*, 545(7654):323–326, May 2017. ISSN 0028-0836. doi: 10.1038/nature22310. URL `https://www.nature.com/nature/journal/v545/n7654/full/nature22310.html`.

[60] W. S. Bakr, J. I. Gillen, A. Peng, S. Fölling, and M. Greiner. A quantum gas microscope for detecting single atoms in a hubbard-regime optical lattice. *Nature*, 462:74, 2009. doi: 10.1038/nature08482. URL `https://www.nature.com/articles/nature08482`.

[61] S.E. Pollack, D. Dries, M. Junker, Y.P. Chen, T.A. Corcovilos, and R.G. Hulet. Extreme tunability of interactions in a ^{7}Li Bose-Einstein condensate. *Phys. Rev. Lett.*, 102:090402, 2009. doi: 10.1103/PhysRevLett.102.090402. URL `https://journals.aps.org/prl/abstract/10.1103/PhysRevLett.102.090402`.

[62] T. Fernholz, R. Gerritsma, P. Krueger, and R.J.C. Spreeuw. Dynamically Controlled Toroidal and Ring-Shaped Magnetic Traps. *Phys. Rev. A.*, page 75:063406, 2007. doi: 10.1103/PhysRevA.75.063406. URL `https://journals.aps.org/pra/abstract/10.1103/PhysRevA.75.063406`.

[63] K.C. Wright, R.B. Blakestad, C.J. Lobb, W.D. Phillips, and G.K. Campbell. Driving Phase Slips in a Superfluid Atom Circuit with a Rotating Weak Link. *Phys. Rev. Lett.*, 110:025302, 2013. doi: 10.1103/PhysRevLett.110.025302. URL `https://journals.aps.org/prl/abstract/10.1103/PhysRevLett.110.025302`.

[64] Juan Carrasquilla, Salvatore R Manmana, and Marcos Rigol. Scaling of the gap, fidelity susceptibility, and bloch oscillations across the superfluid-to-mott-insulator transition in the one-dimensional bose-hubbard model. *Physical Review A*, 87(4):043606, 2013.

[65] Lincoln Carr. *Understanding quantum phase transitions*. CRC press, 2010.

[66] Lincoln D Carr, ML Wall, DG Schirmer, RC Brown, JE Williams, and Charles W Clark. Mesoscopic effects in quantum phases of ultracold quantum gases in optical lattices. *Physical Review A*, 81(1):013613, 2010.

[67] Anatoli Polkovnikov, Krishnendu Sengupta, Alessandro Silva, and Mukund Vengalattore. Colloquium: Nonequilibrium dynamics of closed interacting quantum systems. *Reviews of Modern Physics*, 83(3):863, 2011.

[68] R. V. Mishmash. Quantum many-body dynamics of ultracold bosons in one-dimensional optical lattices: Theoretical aspects, simulation methods, and soliton formation and stability. Master's thesis, Colorado School of Mines, 2012. URL `http://inside.mines.edu/~lcarr/theses/mishmash_thesis_2008.pdf`.

[69] R. Carretero-Gonzlez, D. J. Frantzeskakis, and P. G. Kevrekidis. Nonlinear waves in BoseEinstein condensates: physical relevance and mathematical techniques. *Nonlinearity*, 21(7):R139, 2008. ISSN 0951-7715. doi: 10.1088/0951-7715/21/7/R01. URL `http://stacks.iop.org/0951-7715/21/i=7/a=R01`.

[70] L. D. Landau and E. M. Lifshitz. *Vol. 3. Quantum Mechanics–Non-relativistic Theory, 3rd Ed.* Pergamon Press, 1977.

[71] C.J. Pethick and H. Smith. *Bose-Einstein Condensation in Dilute Gases*. Cambridge University Press, 2001.

[72] D. Jaksch, C. Bruder, J.I. Cirac, C.W. Gardiner, and P. Zoller. Cold bosonic atoms in optical lattices. *Phys. Rev. Lett.*, 81:3108, 1998. doi: 10.1103/PhysRevLett.81.3108. URL `https://journals.aps.org/prl/abstract/10.1103/PhysRevLett.81.3108`.

[73] D. Jaksch and P. Zoller. The cold atom Hubbard toolbox. *Annals of Physics*, 315(1): 52–79, January 2005. ISSN 0003-4916. doi: 10.1016/j.aop.2004.09.010. URL `http://www.sciencedirect.com/science/article/pii/S0003491604001782`.

[74] Andrea Trombettoni and Augusto Smerzi. Discrete Solitons and Breathers with Dilute Bose-Einstein Condensates. *Physical Review Letters*, 86(11):2353–2356, March 2001. doi: 10.1103/PhysRevLett.86.2353. URL `http://link.aps.org/doi/10.1103/PhysRevLett.86.2353`.

[75] TEBD. Time-Evolving Block Decimation open source code. `https://sourceforge.net/projects/opentebd`.

[76] Guifr Vidal. Efficient Classical Simulation of Slightly Entangled Quantum Computations. *Physical Review Letters*, 91(14):147902, October 2003. doi: 10.1103/PhysRevLett.91.147902. URL `http://link.aps.org/doi/10.1103/PhysRevLett.91.147902`.

[77] Guifr Vidal. Efficient Simulation of One-Dimensional Quantum Many-Body Systems. *Physical Review Letters*, 93(4):040502, July 2004. doi: 10.1103/PhysRevLett.93.040502. URL `http://link.aps.org/doi/10.1103/PhysRevLett.93.040502`.

[78] A. J. Daley, C. Kollath, U. Schollwck, and G. Vidal. Time-dependent density-matrix renormalization-group using adaptive effective Hilbert spaces. *Journal of Statistical Mechanics: Theory and Experiment*, 2004(04):P04005, 2004. ISSN 1742-5468. doi: 10.1088/1742-5468/2004/04/P04005. URL `http://stacks.iop.org/1742-5468/2004/i=04/a=P04005`.

[79] Steven R. White and Adrian E. Feiguin. Real-Time Evolution Using the Density Matrix Renormalization Group. *Physical Review Letters*, 93(7):076401, August 2004. doi: 10.1103/PhysRevLett.93.076401. URL `http://link.aps.org/doi/10.1103/PhysRevLett.93.076401`.

[80] J. Eisert, M. Cramer, and M. B. Plenio. Colloquium: Area laws for the entanglement entropy. *Rev. Mod. Phys.*, 82:277–306, Feb 2010. doi: 10.1103/RevModPhys.82.277. URL `https://link.aps.org/doi/10.1103/RevModPhys.82.277`.

[81] Wall M. L. *Quantum Many-Body Physics of Ultracold Molecules in Optical Lattices: Models and Simulation Methods*. PhD thesis, Colorado School of Mines, 2012.

[82] MPS. Matrix product state open source code.`http://sourceforge.net/projects/openmps`.

[83] Masuo Suzuki. Fractal decomposition of exponential operators with applications to many-body theories and Monte Carlo simulations. *Physics Letters A*, 146(6):319–323, June 1990. ISSN 0375-9601. doi: 10.1016/0375-9601(90)90962-N. URL `https://www.sciencedirect.com/science/article/pii/037596019090962N`.

[84] Shreyas Potnis, Ramon Ramos, Kenji Maeda, Lincoln D. Carr, and Aephraim M. Steinberg. Interaction-Assisted Quantum Tunneling of a Bose-Einstein Condensate Out of a Single Trapping Well. *Physical Review Letters*, 118(6):060402, February 2017. doi: 10.1103/PhysRevLett.118.060402. URL `https://link.aps.org/doi/10.1103/PhysRevLett.118.060402`.

[85] Xinxin Zhao. *Quantum Dynamics of Ultracold Bosons*. PhD thesis, Peking University, 2019.

[86] P. Schlagheck and S. Wimberger. Nonexponential decay of bose–einstein condensates: a numerical study based on the complex scaling method. *Applied Physics B*, 86(3): 385–390, 2007. ISSN 1432-0649. doi: 10.1007/s00340-006-2511-8. URL `http://dx.doi.org/10.1007/s00340-006-2511-8`.

[87] Nimrod Moiseyev, L. D. Carr, Boris A. Malomed, and Y. B. Band. Transition from resonances to bound states in nonlinear systems: application to BoseEinstein condensates. *Journal of Physics B: Atomic, Molecular and Optical Physics*, 37 (9):L193, 2004. ISSN 0953-4075. doi: 10.1088/0953-4075/37/9/L02. URL `http://stacks.iop.org/0953-4075/37/i=9/a=L02`.

[88] L. D. Carr, M. J. Holland, and B. A. Malomed. Macroscopic quantum tunnelling of BoseEinstein condensates in a finite potential well. *Journal of Physics B: Atomic, Molecular and Optical Physics*, 38(17):3217, 2005. ISSN 0953-4075. doi: 10.1088/0953-4075/38/17/012. URL `http://stacks.iop.org/0953-4075/38/i=17/a=012`.

[89] Demetrios N. Christodoulides, Eugenia D. Eugenieva, Tamer H. Coskun, Mordechai Segev, and Matthew Mitchell. Equivalence of three approaches describing partially incoherent wave propagation in inertial nonlinear media. *Physical Review E*, 63(3): 035601, February 2001. doi: 10.1103/PhysRevE.63.035601. URL `http://link.aps.org/doi/10.1103/PhysRevE.63.035601`.

[90] Demetrios N. Christodoulides, Tamer H. Coskun, Matthew Mitchell, and Mordechai Segev. Theory of Incoherent Self-Focusing in Biased Photorefractive Media. *Physical Review Letters*, 78(4):646–649, January 1997. doi: 10.1103/PhysRevLett.78.646. URL `http://link.aps.org/doi/10.1103/PhysRevLett.78.646`.

[91] D. N. Christodoulides, T. H. Coskun, and R. I. Joseph. Incoherent spatial solitons in saturable nonlinear media. *Optics Letters*, 22(14):1080, July 1997. ISSN 0146-9592, 1539-4794. doi: 10.1364/OL.22.001080. URL `https://www.osapublishing.org/abstract.cfm?URI=ol-22-14-1080`.

[92] Tamer H. Coskun, Demetrios N. Christodoulides, Matthew Mitchell, Zhigang Chen, and Mordechai Segev. Dynamics of incoherent bright and dark self-trapped beams and their coherence properties in photorefractive crystals. *Optics Letters*, 23(6):418, March 1998. ISSN 0146-9592, 1539-4794. doi: 10.1364/OL.23.000418. URL `https://www.osapublishing.org/abstract.cfm?URI=ol-23-6-418`.

[93] Eugenia D. Eugenieva, Demetrios N. Christodoulides, and Mordechai Segev. Elliptic incoherent solitons in saturable nonlinear media. *Optics Letters*, 25(13):972–974, July 2000. ISSN 1539-4794. doi: 10.1364/OL.25.000972. URL `http://www.osapublishing.org/abstract.cfm?uri=ol-25-13-972`.

[94] V. P. Nayyar. Propagation of partially coherent Gaussian Schell-model sources in nonlinear media. *JOSA B*, 14(9):2248–2253, September 1997. ISSN 1520-8540. doi: 10.1364/JOSAB.14.002248. URL `http://www.osapublishing.org/abstract.cfm?uri=josab-14-9-2248`.

[95] Akira Hasegawa. Dynamics of an ensemble of plane waves in nonlinear dispersive media. *Physics of Fluids (1958-1988)*, 18(1):77–79, January 1975. ISSN 0031-9171. doi: 10.1063/1.860997. URL `http://scitation.aip.org/content/aip/journal/pof1/18/1/10.1063/1.860997`.

[96] Allan W. Snyder and D. John Mitchell. Big Incoherent Solitons. *Physical Review Letters*, 80(7):1422–1424, February 1998. doi: 10.1103/PhysRevLett.80.1422. URL `http://link.aps.org/doi/10.1103/PhysRevLett.80.1422`.

[97] Vladimir V. Shkunov and Dana Z. Anderson. Radiation Transfer Model of Self-Trapping Spatially Incoherent Radiation by Nonlinear Media. *Physical Review Letters*, 81(13):2683–2686, September 1998. doi: 10.1103/PhysRevLett.81.2683. URL `http://link.aps.org/doi/10.1103/PhysRevLett.81.2683`.

[98] Matthew Mitchell, Mordechai Segev, Tamer H. Coskun, and Demetrios N. Christodoulides. Theory of Self-Trapped Spatially Incoherent Light Beams. *Physical Review Letters*, 79(25):4990–4993, December 1997. doi: 10.1103/PhysRevLett.79.4990. URL `http://link.aps.org/doi/10.1103/PhysRevLett.79.4990`.

[99] Demetrios N. Christodoulides, Tamer H. Coskun, Matthew Mitchell, and Mordechai Segev. Multimode Incoherent Spatial Solitons in Logarithmically Saturable Nonlinear Media. *Physical Review Letters*, 80(11):2310–2313, March 1998. doi: 10.1103/PhysRevLett.80.2310. URL `http://link.aps.org/doi/10.1103/PhysRevLett.80.2310`.

[100] Nail Akhmediev, Wiesaw Krlikowski, and A. W. Snyder. Partially Coherent Solitons of Variable Shape. *Physical Review Letters*, 81(21):4632–4635, November 1998. doi: 10.1103/PhysRevLett.81.4632. URL `http://link.aps.org/doi/10.1103/PhysRevLett.81.4632`.

[101] Wiesaw Krlikowski, Nail Akhmediev, and Barry Luther-Davies. Collision-induced shape transformations of partially coherent solitons. *Physical Review E*, 59(4):4654–4658, April 1999. doi: 10.1103/PhysRevE.59.4654. URL `http://link.aps.org/doi/10.1103/PhysRevE.59.4654`.

[102] Andrey A. Sukhorukov and Nail N. Akhmediev. Coherent and Incoherent Contributions to Multisoliton Complexes. *Physical Review Letters*, 83(23):4736–4739, December 1999. doi: 10.1103/PhysRevLett.83.4736. URL `http://link.aps.org/doi/10.1103/PhysRevLett.83.4736`.

[103] H. Buljan, M. Segev, and A. Vardi. Incoherent Matter-Wave Solitons and Pairing Instability in an Attractively Interacting Bose-Einstein Condensate. *Physical Review Letters*, 95(18):180401, October 2005. doi: 10.1103/PhysRevLett.95.180401. URL `http://link.aps.org/doi/10.1103/PhysRevLett.95.180401`.

[104] J. A. Glick. Entangled quantum dynamics via macroscopic quantum tunneling of bright solitons in bose-einstein condensates. Master's thesis, Colorado School of Mines, 2012. URL `http://inside.mines.edu/~lcarr/theses/glick_thesis_2011.pdf`.

[105] J. A. Glick and Lincoln D. Carr. Macroscopic quantum tunneling of solitons in bose-einstein condensates, 2011.

[106] Ulrich Schollwoeck. The density-matrix renormalization group in the age of matrix product states. *Ann. Phys.*, 326:96–192, 2011.

[107] David Stadler, Sebastian Krinner, Jakob Meineke, Jean-Philippe Brantut, and Tilman Esslinger. Observing the drop of resistance in the flow of a superfluid fermi gas. *Nature*, 491(7426):736–739, 2012. URL `http://www.nature.com/nature/journal/v491/n7426/full/nature11613.html`.

[108] T. Schweigler, V. Kasper, S. Erne, B. Rauer, T. Langen, T. Gasenzer, J. Berges, and J. Schmiedmayer. On solving the quantum many-body problem. *ArXiv e-prints*, May 2015.

[109] S. Potnis, R. Ramos, K. Maeda, Lincoln D. Carr, and A. Steinberg. Interaction assisted tunneling of Bose-Einstein condensate out of a quasi-bound state. *Phys. Rev. Lett., to be submitted*, 2016. URL `https://arxiv.org/abs/1604.06388`.

[110] Ehud Altman, Eugene Demler, and Mikhail D. Lukin. Probing many-body states of ultracold atoms via noise correlations. *Physical Review A*, 70(1):013603, July 2004. doi: 10.1103/PhysRevA.70.013603. URL `http://link.aps.org/doi/10.1103/PhysRevA.70.013603`.

[111] G. Gamow. Zur quantentheorie des atomkernes. *Zeitschrift für Physik*, 51(3):204–212, 1928. ISSN 0044-3328. doi: 10.1007/BF01343196. URL `http://dx.doi.org/10.1007/BF01343196`.

[112] R. W. Gurney and E. U. Condon. Quantum Mechanics and Radioactive Disintegration. *Physical Review*, 33:127–140, 1929. doi: 10.1103/PhysRev.33.127. URL `http://link.aps.org/doi/10.1103/PhysRev.33.127`.

[113] Markus Greiner, Immanuel Bloch, Olaf Mandel, Theodor W Hänsch, and Tilman Esslinger. Exploring phase coherence in a 2d lattice of bose-einstein condensates. *Physical Review Letters*, 87(16):160405, 2001.

[114] Maciej Lewenstein, Anna Sanpera, and Veronica Ahufinger. *Ultracold Atoms in Optical Lattices: Simulating quantum many-body systems*. Oxford University Press, 2012.

[115] F Iachello. Analytic description of critical point nuclei in a spherical-axially deformed shape phase transition. *Physical Review Letters*, 87(5):052502, 2001.

[116] Daniel Jaschke, Michael L Wall, and Lincoln D Carr. Open source matrix product states: Opening ways to simulate entangled many-body quantum systems in one dimension. *Computer Physics Communications*, 225:59–91, 2018.

[117] Immanuel Bloch, Jean Dalibard, and Sylvain Nascimbene. Quantum simulations with ultracold quantum gases. *Nature Physics*, 8(4):267–276, 2012.

[118] Ippei Danshita and Anatoli Polkovnikov. Superfluid-to-mott-insulator transition in the one-dimensional bose-hubbard model for arbitrary integer filling factors. *Physical Review A*, 84(6):063637, 2011.

[119] Harry J Lipkin, N Meshkov, and AJ Glick. Validity of many-body approximation methods for a solvable model:(i). exact solutions and perturbation theory. *Nuclear Physics*, 62(2):188–198, 1965.

[120] DR Dounas-Frazer, AM Hermundstad, and LD Carr. Ultracold bosons in a tilted multilevel double-well potential. *Physical review letters*, 99(20):200402, 2007.

[121] Diego A Alcala, Gregor Urban, Matthias Weidemüller, and Lincoln D Carr. Macroscopic quantum escape of bose-einstein condensates: Analysis of experimentally realizable quasi-one-dimensional traps. *Physical Review A*, 98(2):023619, 2018.

[122] G Dekel, V Fleurov, Avraham Soffer, and C Stucchio. Temporal dynamics of tunneling: Hydrodynamic approach. *Physical Review A*, 75(4):043617, 2007.

[123] LD Carr and J Brand. Spontaneous soliton formation and modulational instability in bose-einstein condensates. *Physical review letters*, 92(4):040401, 2004.

[124] Elliott H Lieb and Derek W Robinson. The finite group velocity of quantum spin systems. In *Statistical mechanics*, pages 425–431. Springer, 1972.

[125] H Francis Song, Stephan Rachel, Christian Flindt, Israel Klich, Nicolas Laflorencie, and Karyn Le Hur. Bipartite fluctuations as a probe of many-body entanglement. *Physical Review B*, 85(3):035409, 2012.

[126] Steven R Wilkinson, Cyrus F Bharucha, Martin C Fischer, Kirk W Madison, Patrick R Morrow, Qian Niu, Bala Sundaram, and Mark G Raizen. Experimental evidence for non-exponential decay in quantum tunnelling. *Nature*, 387(6633):575–577, 1997.

[127] Mark Jreissaty, Juan Carrasquilla, F Alexander Wolf, and Marcos Rigol. Expansion of bose-hubbard mott insulators in optical lattices. *Physical Review A*, 84(4):043610, 2011.

[128] Yuya O Nakagawa, Masataka Watanabe, Hiroyuki Fujita, and Sho Sugiura. Universality in volume-law entanglement of scrambled pure quantum states. *Nature communications*, 9(1):1–8, 2018.

[129] Immanuel Bloch, Theodor W Hänsch, and Tilman Esslinger. Atom laser with a cw output coupler. *Physical Review Letters*, 82(15):3008, 1999.

[130] LD Carr and J Brand. Pulsed atomic soliton laser. *Physical Review A*, 70(3):033607, 2004.

[131] María I Rodas-Verde, Humberto Michinel, and Víctor M Pérez-García. Controllable soliton emission from a bose-einstein condensate. *Physical review letters*, 95(15): 153903, 2005.

[132] Anton Öttl, Stephan Ritter, Michael Köhl, and Tilman Esslinger. Correlations and counting statistics of an atom laser. *Physical Review Letters*, 95(9):090404, 2005.

[133] Tim Langen, Sebastian Erne, Remi Geiger, Bernhard Rauer, Thomas Schweigler, Maximilian Kuhnert, Wolfgang Rohringer, Igor E Mazets, Thomas Gasenzer, and Jörg Schmiedmayer. Experimental observation of a generalized gibbs ensemble. *Science*, 348(6231):207–211, 2015.

[134] BT Seaman, M Krämer, DZ Anderson, and MJ Holland. Atomtronics: Ultracold-atom analogs of electronic devices. *Physical Review A*, 75(2):023615, 2007.

[135] Guido Burkard, Daniel Loss, and Eugene V Sukhorukov. Noise of entangled electrons: Bunching and antibunching. *Physical Review B*, 61(24):R16303, 2000.

[136] John W Harris and Berndt Müller. The search for the quark-gluon plasma. *Annual Review of Nuclear and Particle Science*, 46(1):71–107, 1996.

[137] Marie A McLain, Diego A Alcala, and Lincoln D Carr. For high-precision bosonic josephson junctions, many-body effects matter. *Quantum Science and Technology*, 3 (4):044005, aug 2018. doi: 10.1088/2058-9565/aad399. URL `https://doi.org/10.1088%2F2058-9565%2Faad399`.

[138] Marie A McLain and Lincoln D Carr. Quantum phase transition modulation in an atomtronic mott switch. *Quantum Science and Technology*, 3(3):035012, 2018.

[139] M. Albeiz, R. Gati, J. Flling, S. Hunsmann, M. Cristiani, and M.K. Oberthaler. Direct Observation of Tunneling and Nonlinear Self-Trapping in a Single Bosonic Josephson Junction. *Phys. Rev. Lett.*, 95:010402, 2005. doi: 10.1103/PhysRevLett.95.010402. URL `https://journals.aps.org/prl/abstract/10.1103/PhysRevLett.95.010402`.

[140] Boris A. Malomed. *Spontaneous Symmetry Breaking, Self-Trapping, and Josephson Oscillations*. Springer. ISBN 9783642212062., 2014. ISBN ISBN 9783642212062.

[141] R. Khomeriki, J. Leon, S. Ruffo, and S. Wimberger. Nonlinear dynamics in double square-well potentials. 152(2):1122–1131. ISSN 1573-9333. doi: 10.1007/s11232-007-0096-y. URL `https://doi.org/10.1007/s11232-007-0096-y`.

[142] B. Gaury, J. Weston, and X. Waintel. The a.c. Josephson effect without superconductivity. *Nature Comm.*, 6:6524, 2015. doi: 10.1038/ncomms7524. URL `https://www.nature.com/articles/ncomms7524`.

[143] Han Du, Xingwang Zhang, Guiqiang Chen, Jie Deng, Fook Siong Chau, and Guangya Zhou. Precise control of coupling strength in photonic molecules over a wide range using nanoelectromechanical systems. *Sci. Rep.*, 6:24766, 2016. doi: 10.1038/srep24766. URL `https://www.nature.com/articles/srep24766`.

[144] B.A. Malomed. Nonlinear optics: Symmetry breaking in laser cavities. *Nature Photonics*, 9(5):287–289, 2015. doi: 10.1038/nphoton.2015.66. URL `https://www.nature.com/articles/nphoton.2015.66`.

[145] S. Levy, E. Lahoud, I. Shomroni, and J. Steinhauer. The a.c. and d.c. josephson effects in a boseeinstein condensate. *Nature*, 449:579–583, 2007. doi: doi:10.1038/nature06186. URL https://www.nature.com/articles/nature06186?free=2.

[146] M. Galbiati et al. Polariton condensation in photonic molecules. *Phys. Rev. Lett.*, 108: 126403, 2012. doi: 10.1103/PhysRevLett.108.126403. URL https://journals.aps.org/prl/abstract/10.1103/PhysRevLett.108.126403.

[147] Y. Yu, S. Han, X. Chu, S-I Chu, and Z Wang. Coherent temporal oscillations of macroscopic quantum states in a Josephson junction. *Science*, 296:889, 2002. doi: 10.1126/science.1069452. URL http://science.sciencemag.org/content/296/5569/889.

[148] A. Smerzi, S. Fantoni, S. Giovanazzi, and S. R. Shenoy. Quantum coherent atomic tunnelling between two trapped BoseEinstein condensates. *Phys. Rev. Lett.*, 79:4950, 1997. doi: 10.1103/PhysRevLett.79.4950. URL https://journals.aps.org/prl/abstract/10.1103/PhysRevLett.79.4950.

[149] G.G. Batrouni, V. Rousseau, R.T. Scalettar, M. Rigol, A. Muramatsu, P.J.H. Denteneer, and M. Troyer. Mott domains of bosons confined on optical lattices. *Phys. Rev. Lett.*, 89:117203, 2002. doi: https://doi.org/10.1103/PhysRevLett.89.117203. URL https://journals.aps.org/prl/abstract/10.1103/PhysRevLett.89.117203.

[150] Elliott H. Lieb and Derek W. Robinson. The finite group velocity of quantum spin systems. 28(3):251–257. ISSN 1432-0916. doi: 10.1007/BF01645779. URL https://doi.org/10.1007/BF01645779.

[151] Michael Foss-Feig, Zhe-Xuan Gong, Charles W. Clark, and Alexey V. Gorshkov. Nearly linear light cones in long-range interacting quantum systems. *Phys. Rev. Lett.*, 114: 157201, Apr 2015. doi: 10.1103/PhysRevLett.114.157201. URL https://link.aps.org/doi/10.1103/PhysRevLett.114.157201.

[152] Zhe-Xuan Gong, Michael Foss-Feig, Spyridon Michalakis, and Alexey V. Gorshkov. Persistence of locality in systems with power-law interactions. *Phys. Rev. Lett.*, 113: 030602, Jul 2014. doi: 10.1103/PhysRevLett.113.030602. URL https://link.aps.org/doi/10.1103/PhysRevLett.113.030602.

[153] Bruno Nachtergaele and Robert Sims. Much ado about something: why lieb-robinson bounds are useful. *arXiv preprint arXiv:1102.0835*, 2011.

[154] Gregor Urban. Macroscopic quantum tunnelling of bose-einstein condensates in finite potential wells, 2012. Unpublished Bachelor's thesis.

[155] M. Egorov, B. Opanchuk, P. Drummond, B. V. Hall, P. Hannaford, and A. I. Sidorov. Measurement of s-wave scattering lengths in a two-component Bose-Einstein condensate. *Physical Review A*, 87(5):053614, May 2013. doi: 10.1103/PhysRevA.87.053614. URL `http://link.aps.org/doi/10.1103/PhysRevA.87.053614`.

[156] V. P. Ruban. Gaussian variational ansatz in the problem of anomalous sea waves: Comparison with direct numerical simulation. *Journal of Experimental and Theoretical Physics*, 120(5):925–932, May 2015. ISSN 1063-7761, 1090-6509. doi: 10.1134/S1063776115050179. URL `https://link.springer.com/article/10.1134/S1063776115050179`.

[157] F. Wchtler and L. Santos. Ground-state properties and elementary excitations of quantum droplets in dipolar Bose-Einstein condensates. *Physical Review A*, 94(4): 043618, October 2016. doi: 10.1103/PhysRevA.94.043618. URL `https://link.aps.org/doi/10.1103/PhysRevA.94.043618`.